Democratic and Popular Republic of Algeria
Ministry of Higher Education and Scientific Research
University Mohamed Khider of Biskra

Faculty of Exact Sciences and Science of Nature and Life
Department of Material Sciences

Ref:....

Thesis Presented to obtain the degree of

Doctorate in Physics
Option: **Physics**

Entitled:

Study of organic solar cells based on wide band gap semiconductor/perovskite hetero-junction

Presented by: **Barkat Sarra**

Publicly defended on: 31/ 10/ 2024

In front of the Jury committee composed of:

NOUREDINE SENGOUGA	**Prof**	**University of Biskra**	**President**
MEFTAH AFAK	**Prof**	**University of Biskra**	**Supervisor**
MEFTAH AMJAD	**Prof**	**University of Biskra**	**Examiner**
FILALI WALID	**M.R.A**	**C.D.T.A. Algiers**	**Examiner**

Academic Year: 2024

Dedications

Praise be to ALLAH at the beginning and at the end

To my parents: thank you for always being there for me and supporting me while I studied and while I did the research for and wrote this thesis. Without them, it would not have been possible to do this..

To my loving family, whose unwavering support and belief in me have been the pillars of my journey. This work is a testament to your love and encouragement.

To my professors and colleagues, who have enriched my academic journey with their wisdom and camaraderie. Your guidance has been invaluable.,

And to all those who find joy in the pursuit of knowledge, may this work inspire and contribute to our collective understanding..

Acknowledgments

Initially, I express my profound gratitude to Allah, the Most Gracious and the Most Merciful, for granting me the fortitude, wisdom, and chance to conduct this research work, as well as for His abundant blessings and guidance throughout my life and academic pursuits.

I would like to extend my profound gratitude to all those who afforded me the opportunity to successfully accomplish my thesis. I would like to express my sincere appreciation to my doctoral supervisor, Professor Meftah Afak, for their invaluable support and guidance. Their insightful recommendations and encouragement greatly assisted me in successfully completing my project, particularly in the process of writing this thesis.

Besides my advisors, I would like to thank the rest of my thesis committee: ,Professor Nouredine Sengouga, Professor Meftah Amjad, and Doctor Filali Walid, for their insightful comments and encouragement, but also for the hard question which incented me to widen my research from various perspectives.

My sincere thanks also goes to **Dr Madani Labed**, **Dr Maroua Abdaallaoui**, and **Douaa Abdaallaoui **, who have willingly shared their precious time during the process of accomplishing this research.

I also extend my thanks to my colleagues and friends in the **Department of Material Sciences** for their understanding and support in completing this project. Thank you.

ABSTRACT

This thesis focuses on enhancing the efficiency of solar cells by utilizing perovskite materials, specifically two different perovskite Cesium silver bismuth iodide (Cs_2BiAgI_6) and methyl ammonium lead triiodide ($MAPbI_3$). Through meticulous investigation and analysis, the aim is to advance solar cell technology. The performance of solar cells based on different structures of Cs_2BiAgI_6 and $MAPbI_3$ is simulated using Silvaco-ATLAS software to optimize their efficiency. Initially, the study delves into Cs_2BiAgI_6 solar cells, adjusting various parameters such as the hole transport layer (NiO), electron transport layer (ZnO), and front contact (ITO with SiO_2). Significant enhancement in power conversion efficiency (PCE) up to 32.86% is achieved, showcasing the effectiveness of the optimizations. Additionally, a comparative analysis between Cs_2BiAgI_6 and $CH_3NH_3PbI_3$ solar cells reveals Cs_2BiAgI_6's superior performance with a *PCE* of 23.02%. This research aims to contribute valuable insights into the properties, efficiency, and stability of these materials,advancing their potential applications in solar energy.

Keywords: $CH_3NH_3PbI_3$, Cs_2BiAgI_6, HTL, ETL, SILVACO-ATLAS, Perovskite solar cells.

ملخص

تركز هذه الرسالة على اقتراح وفحص الخلايا الشمسية التي تستخدم مواد البيروفسكيت. الهدف الرئيسي هو تحسين كفاءة تحويل الطاقة لهذه الأجهزة. المواد البيروفسكيت التي تمت دراستها هي البيروفسكيت المزدوج Cs_2BiAgI_6 وثلاثي اليوديد الرصاصي لميثيل أمونيوم $MAPbI_3$. يسعى هذا البحث لتقديم مساهمة قيمة في تقدم تكنولوجيا الخلايا الشمسية من خلال التحقيق والتحليل الدقيق. تم تحديد أداء الخلايا الشمسية بناءً على بنيتين مختلفتين من Cs_2BiAgI_6 و $MAPbI_3$ عددياً باستخدام برنامج Silvaco-ATLAS. لتعزيز كفاءتها وفعاليتها الشاملة. بالتالي، تم تنفيذ عملية تحسين منهجية على هذه البنيات لاكتشاف تحسين كفاءة تحويل الطاقة المحسن للخلايا الشمسية. بدأت دراستنا بدراسة خلية البيروفسكيت المزدوجة Cs_2BiAgI_6. لقد ضبطنا متغيرات مختلفة للتحقيق في تأثيرها على خلية البيروفسكيت المزدوجة التي تتألف من NiO كطبقة HTL، و ZnO كطبقة ETL ، و ITO كجهة اتصال أمامية مع SiO_2 كطبقة مضادة للانعكاس و Ag كجهة اتصال خلفية. أظهرت النتائج المتحصل عليها تحسنا كبيرا في كفاءة تحويل الطاقة (PCE) إلى 32.86% ملحوظة. يسلط هذا الارتفاع الضوء على فعالية التدابير المتبعة في تعزيز الأداء الشامل. بالإضافة، هدفنا هو إجراء دراسة شاملة على خلية البيروفسكيت $CH_3NH_3PbI_3$ ومقارنة أدائها بأداء خلية البيروفسكيت Cs_2BiAgI_6. ستوفر هذه التحليلات رؤى قيمة حول التشابهات والاختلافات بين هاتين التقنيتين للخلية الشمسية. من خلال فحص خصائصها وكفاءتها واستقرارها، نهدف إلى المساهمة في الفهم العلمي لهذه المواد وتطبيقاتها المحتملة في مجال الطاقة الشمسية. تشير النتائج إلى كفاءة تحويل الطاقة (PCE) بنسبة 23.02% تم الحصول عليها لـ $CH_3NH_3PbI_3$ لذا تفوقت Cs_2BiAgI_6 على $CH_3NH_3PbI_3$ بفضل خصائصها الكهربائية المواتية.

الكلمات المفتاحية : $CH_3NH_3PbI_3$ ، Cs_2BiAgI_6، HTL، ETL، Silvaco-ATLAS،خلايا شمسية بيروفسكيت.

Résumé

Cette thèse se concentre sur l'amélioration de l'efficacité des cellules solaires en utilisant des matériaux de type pérovskite, notamment deux différents pérovskites (Cs_2BiAgI_6) et le triiodure de plomb de méthylammonium ($MAPbI_3$). À travers une investigation minutieuse et une analyse, l'objectif est de faire progresser la technologie des cellules solaires. Les performances des cellules solaires basées sur différentes structures de Cs_2BiAgI_6 et ($MAPbI_3$) sont simulées à l'aide du logiciel Silvaco-ATLAS afin d'optimiser leur efficacité. Initialement, l'étude se penche sur les cellules solaires (Cs_2BiAgI_6), en ajustant divers paramètres tels que la couche de transport de trous (NiO), la couche de transport d'électrons (ZnO) et le contact avant (ITO avec SiO_2). Une amélioration significative de l'efficacité de conversion de puissance (PCE) allant jusqu'à 32,86% est obtenue,démontrant ainsi l'efficacité des optimisations. De plus, une analyse comparative entre les cellules solaires (Cs_2BiAgI_6) et $CH_3NH_3PbI_3$ révèle la performance supérieure de (Cs_2BiAgI_6) avec une PCE de 23,02%. Cette recherche vise à apporter des éclairages précieux sur les propriétés, l'efficacité et la stabilité de ces matériaux, et à faire accroitre leurs applications potentielles dans l'énergie solaire.

Mots clés : $CH_3NH_3PbI_3$, Cs_2BiAgI_6, HTL, ETL, SILVACO-ATLAS, Cellules solaires en pérovskite.

Contents

List of Figures

List of Tables

List of Abbreviations

Abbreviation	Description
HTL	Hole Transport Layer
ETL	Electron Transport Layer
LUMO	Lowest Unoccupied Molecular Orbital
HOMO	Highest Occupied Molecular Orbital
Spiro-OMeTAD	2,2',7,7'-Tetrakis[N,N-di(4-methoxyphenyl)amino]-9,9'-spirobifluorene
PTAA	Poly(triaryl amine), Poly[bis(4-phenyl)(2,4,6-trimethylphenyl)amine]
P3HT	Poly(3-hexylthiophene-2,5-diyl)
PEDOT:PSS	poly(3,4-ethylenedioxythiophene) polystyrene sulfonate
ITO	Indium Tin Oxide
SiO_2	Silicon Dioxide
PSC	Perovskite Solar Cell
OSC	Organic Solar Cell
DSSC	Dye-Sensitized Solar Cell
NREL	National Renewable Energy Laboratory
BHJ	Bulk Heterojunction
WBG	Wide Band Gap
PV	Photvoltaique
SILVACO	Silicon valley corporation
TCAD	Technology computer aided design
E_g	Gap energy (eV)
χ	Affinity of the semiconductor (eV)
N_c	Effective density of conduction band (cm^{-3})
N_v	Effective density of valence band (cm^{-3}).
μ_n	Electron mobility $(cm^2V^{-1}s^{-1})$
μ_p	Hole mobility $(cm^2V^{-1}s^{-1})$
ε_r	Relative dielectric constant
J_{sc}	Short Circuit Current density (mA/cm^2)
V_{oc}	Open Circuit Volatage (V)
PCE	Power Conversion Efficiency $(\%)$
FF	Fill Factor $(\%)$
EQE	External Quantum Efficiency $(\%)$
IQE	Internal Quantum Efficiency $(\%)$

Chapter I

Introduction

Chapter I

Introduction

The energy issue is driving the advancement of economical and eco-friendly power generation technology. Solar energy, abundant, clean, and universally available, garner global interest. Solar cells, which have the ability to efficiently convert solar energy into electricity, have become a focal point of study in both industry and science, because they provide a viable option for the environmentally friendly application of solar energy. These cells utilize a range of materials as absorbers to capture sunlight, allowing for the generation of electrical energy. Moreover, solar cells are classified into different generations based on the specific absorber materials employed in their design and construction. The first option is expensive pure silicon solar cells. The second option consists of low-cost amorphous silicon solar cells. The third generation is currently being developed and is characterized by being cost-effective, ecologically friendly, and having a highly stable *PCE*. Perovskite Solar Cells, Quantum Dots Solar Cells, and Organic Solar Cells are all classified as third-generation technologies. Perovskite is utilized in several fields including photodetectors. Liang et al. recently created a range of perovskite films, leading to high-performance photo-detector [1–4].

In recent years, the photovoltaic industry has witnessed significant progress in the development of lead *Pb*-halide-based perovskite solar cells (PSCs). These cells have made incredible progress, with their power conversion efficiency (PCE) surging from a a modest 3.8% in 2009 to an impressive 25.7% in current laboratory settings [3, 5–9].The rapid advancements in this field can be attributed to the distinctive photovoltaic characteristics exhibited by Pb halide perovskites. These characteristics include high absorption coefficients, suitable direct band gaps, high tolerance to defects, efficient exciton separation, and exceptional carrier transport capabilities. These unique properties make Pb halide perovskites an excellent choice for various applications in the field of photovoltaics [3, 10–14].In addition to these exceptional characteristics, the convenient method of preparing the solution enables the use of perovskite materials in various optoelectronic applications, including LEDs, photodetectors, and laser devices [3, 15].

The discovery and subsequent development of perovskite materials for solar cell technology began in 1839 with the initial discovery $CaTiO_3$ in the Ural Mountains of Russia. This pivotal event marked the first step towards the remarkable advancements we have witnessed in this field.

Afterwards, Alexander Kammerer, a Russian mineralogist, efficiently transported the initial mineral sample from Saint Petersburg to Berlin. The transportation was conducted with the intention of facilitating a comprehensive analysis of the mineral by Gustav Rose, a distinguished German mineralogist and crystallographer. Upon analysis, Rose was able to figure out the chemical composition and properties of the mineral. Following the occurrence, Kammerer suggested that Rose name this mineral as a tribute to the esteemed Russian mineralogist, Count Lev Aleksevich Perovski, who had a notable political career [16]. . Consequently, this mineral came to be known as perovskite. Over time, the prevailing configuration for perovskite materials became ABX_3, and researchers adapted the constituent atoms to suit the requirements of the technology [17].

Mitzi et al. investigated organic and inorganic perovskites' optoelectronic properties in the 1990s [18]. The researchers discovered that these materials possess advantageous attributes that hold significant potential for application in the area of solar cell technology [17]. In 2009, Kojima et al. employed dye-sensitized solar cells (DSSCs) that utilized perovskite material as a liquid sensitizer for the first time [9]. The researchers employed $CH_3NH_3PbI_3$ ($MAPbI_3$) and $CH_3NHPbBr$ (MAPbBr) as liquid sensitizers, resulting in respective efficiencies of 3.8% and 3.1% respectively. However, the utilisation of liquid electrolytes rendered these devices highly unstable [17].

In the year 2011, researchers successfully employed $MAPbI_3$ quantum dots, resulting in a notable increase in the efficiency of perovskite solar cells (PSC) from 3.81% to 6.54%. It is important to note, although, that the PSC device could only work for 10 minutes before the quantum dots dissolved into the redox electrolyte solution. The devices experienced instability due to the use of liquid electrolytes, which necessitated the development of strategies to address this issue [19]. In the year 2012, the issue associated with liquid electrolytes was successfully addressed through the integration of Spiro-OMeTAD as a hole-transporting layer (HTL) in the specific photovoltaic perovskite solar cell (PSC) device under consideration. With this change, the device's efficiency (PCE) increased significantly to 9.7%. The device showcased in the study conducted by Kim et al. [20] was regarded as a significant advancement in the field of solar cells. This is due to the fact that it not only exhibited improved efficiency but also demonstrated a remarkable increase in its duration by 500 hours [17].

In 2013, a planar architecture was used to fabricate perovskite solar cells (PSCs), with CH_3NH_3 being placed on top of the PbI_2 layer. This planar structure reportedly has a 15% power conversion efficiency, as reported by Burschka et al. [21]. According to investigations conducted by Im et al.,solar cells were made using $MAPbI_3$ as their basic material [22]. The researchers successfully controlled the size of the cuboid-shaped $MAPbI_3$, resulting in several notable improvements. Improved charge transportation; better light harvesting, and a final boost to 17.01% power conversion efficiency were all part of these enhancements [17].

In 2015, researchers conducted a documented study on the utilization of a Li-doped mesoporous titania layer (m-TiO_2) [23]. This study examined the electrical properties of TiO_2 layers

and showed that adding lithium significantly improved the power conversion efficiency (PCE) to 19.3%. In a study conducted by Yang et al, the researchers investigated the use of a $FAPbI_3$ absorber layer as a substitute for $MAPbI_3$ [24]. Their findings indicate that under $AM1.5G$ full solar illumination, a Efficiency ratio (PCE) of 20.1% was achieved by substituting Formamidinium (FA) over Methylammonium (MA). Li et al employed the vacuum flash-assisted solution processing method (VASP) to fabricate perovskite solar cell devices with an absorber layer composed of $FA_{0.81}MA_{0.15}PbI_{2.51}Br_{0.45}$ [25]. The absorber layers exhibit a uniform morphology characterised by crystalline properties. The investigated device reached a *PCE* of 20.5% [17].

In the year 2016, Bi et al implemented an innovative methodology involving the utilisation of poly (methylmethacrylate) (PMMA), a polymer, in the construction of perovskite solar cell devices [26]. This approach aimed to enhance the electronic and charge transport properties, as well as the process of nucleation of the absorber layer films. The incorporation of PMMA resulted in a notable improvement, leading to the attainment of a maximum power conversion efficiency (PCE) of 21.6% for the device [17].

In the year 2017, various positively charged ions containing FA and anions consisting of mixed halides were employed as absorber layers in the advancement of perovskite solar cells (PSCs). It was noted that the presence of iodide solution in the organic cation solution led to a decrease in the concentrations of deep-level defect states. Yang et al. did a study that showed a device with an area of $1cm^2$ had a (PCE) of 19.7% [27]. Furthermore, it is worth noting that a small-scale device was able to achieve a PCE of 22.1%, demonstrating exceptional efficiency [17]. In 2018, a significant advancement was made within the domain of planar perovskite solar cells. A study conducted by Yang et al. demonstrated the successful implementation of Ethylene diamine tetraacetic acid (EDTA) complexed SnO_2/E$-SnO_2$ as an efficient electron transport layer (ETL). This breakthrough has opened new possibilities for enhancing solar panels' efficiency [27], The researchers observed a significant enhancement in the device's performance through the utilization of EDTA. This led to planar perovskite solar cell (PSC) devices achieving an energy conversion ratio (PCE) of 21.6% [17].

In a study conducted by Jiang et al, the utilization of a phenethylammonium iodide (PEAI) layer for the post-treatment of solar cells, which are built upon mixed perovskite ($FA_{1-x}MA_xPbI_3$) materials, was observed. This innovative approach demonstrated promising leads to a significant improvement in the efficiency and durability of the solar cells [28]. This post-treatment occurred at a later stage in the year 2019. The application of the PEAI layer resulted in the successful passivation of surface defects, consequently leading to a significant improvement in the power conversion efficiency (PCE) of photovoltaic devices. The *PCE* reached an impressive 23.32% in the devices treated with PEAI [17].

In 2020, Green et al. reported that single-junction perovskite solar cells (PSCs) achieved a notable output efficiency (PCE) of 25.2% [29]. Subsequently, in 2021, Green et al reported an increase in *PCE* to 25.5% As of the present time [29], under the 2022 NREL Best Research-Cell

Efficiency Chart, single-junction perovskite solar cells have attained a documented efficiency performance (PCE) of 25.7% [30].

In 2023, there were notable endeavors to improve the efficiency ratio$(PCE)$of single-junction perovskite solar cells (PSCs) [31]. The progress can be credited to enhanced regulation of the crystallization of the perovskite thin film and meticulous refinement of the interfacial contact within the device. In late 2021, scientists from Ulsan National Institute of Science and Technology (UNIST) established a benchmark for small-area cells (with an aperture area of $0.05\tilde{}1cm^2$) by achieving an efficiency factor (PCE) of 25.7% [32, 33]. In November 2022, the same research group achieved a further enhancement of the record to 25.8% [31, 34]. The particular technical information regarding the production of the 25.7% power conversion efficiency (PCE) cell was revealed in early 2023 [33]. To improve the crystallinity and shape of the resultant perovskite layer, volatile alkylammonium chlorides were incorporated into the precursor solution of formamidinium lead iodide ($FAPbI_3$). This improvement significantly decreased defects and enhanced the efficiency of the cell when paired with high-quality charge transport layers [34].

Three new milestones in small-area cell technology were reached in 2023. The Chinese Academy of Sciences' Institute of Semiconductors (ISCAS) broke the 26.0% mark in March [35, 36]. After that, two different groups of researchers came up with an even greater efficiency of 26.1%: one from USTC (University of Science and Technology of China) [37, 38] and another from NWU and UT (University of Toronto) [37, 39]. The fact that these three records are so close in proximity is significant since they all show very similar values for important performance metrics like V_{oc}, J_{sc} , and FF, which guarantees very good performance overall [34].

For perovskite single-junction one-sun cells larger than $1cm^2$, there have been two significant advancements in efficiency. The initial prototype, which received certification in April, demonstrated an impressive efficiency of 24.35% within a prescribed lighting area of $1.007cm^2$. This achievement was made possible by the collaborative efforts of the National University of Singapore (NUS) and the Solar Energy Research Institute of Singapore (SERIS) [40]. In September, Northwestern University achieved an efficiency of 25.2% on an area of $1.0347cm^2$, marking the second improvement. The new power conversion efficiencies $(PCEs)$ have improved values of J_{sc} and FF, while yet keeping a reasonable V_{oc} value. The current record for the power conversion efficiency (PCE) of a minimodule, which is a package consists of multiple interconnected cells, each with an area smaller than$200cm^2$, has remained at 22.4% since 2022. This record was obtained by an 8-cell, $26cm^2$ minimodule [34, 41].

Pb-based perovskite has made significant advancements, yet it encounters two primary challenges in its application. Firstly, there is a need to improve its storage in low humidity conditions and its stability under ambient illumination. Secondly, the potential leakage of Pb elemental poses a high risk. Pb halide perovskite is known to be prone to degradation caused by light, heat, oxygen, and moisture after film formation. This degradation gradually weakens the lattice structure during storage [42]. The current operating stability of Pb-based PSCs is relatively short, typically lasting only a few hundred hours. This is significantly lower than the 25-year

effective lifespan of commercial modules. Similarly, even with LEDs, is often limited to only a few hundred hours [43]. The severe toxicity and cancer-causing properties of water-soluble lead are significant barriers to the widespread use of lead-based perovskite solar cells [3,44,45]. Despite the advancements made in the development of materials with effective Pb sequestration and adsorption properties, as well as various approaches for device encapsulation, the challenge of eliminating the risk of Pb leakage persists. Consequently, many researchers are currently focused on investigating new lead-free perovskite materials to develop solar cells that are both very stable and efficient [3].

Identifying lead-free alternatives is a critical and difficult task in perovskite solar cell technology. Double halide perovskites $A_2BB'X_6$ are a diverse set of compounds with different chemical arrangements. The crystal structures consist of B or B' atoms positioned at the center, while X atoms are located at the corners of corner-splitting octahedra. The computational research conducted by Slavney et al. and Cai et al. reveals that substituting two adjacent Pb^{2+} ions with monovalent and trivalent cations will produce in the formation of 222 supra-cellular perovskites with the overall chemical formula $A_2B^+B^{3+}X_6$ [46–48].

Replacing lead in the crystal structure with monovalent and trivalent metal cations is a progressive and encouraging method of producing structured double perovskites with the chemical formula $A_2B^+B'^{3+}X_6$. This method is extremely efficient as it provides a more extensive range of materials while preserving the integrity of the 3D perovskite structure. Mixing various element A, B^+, B^{3+}, and X results in materials with structural tolerance factors and octahedral factors. Elements A, B^+, and X are defined as follows: (A = K, Rb, Cs; $B^+ = Li^+$, Na^+, K^+, Rb^+, Cs^+, Ag^+; $B^{3+} = Al^{3+}$, Ga^{3+}, In^{3+}, Sb^{3+}, Bi^{3+}, Sc^{3+}, Y^{3+}; and X = F, Cl, Br, I) [49]. Double perovskites, with their diverse structure, robust stability, and absence of lead, offer compelling alternatives for various optoelectronic applications. They exhibit a wide range of functions, making them highly appealing in the field [46].

Cs_2AgBiI_6 has garnered significant attention in the realm of optoelectronics, thanks to its admirable properties in comparison to lead-based perovskites. Its three-dimensional structure, prolonged carrier lifetime, and relatively low effective carrier mass contribute to its appeal. Cs_2AgBiI_6 solar cells have boosted power conversion efficiency(PCE) by over 3% since they were first introduced. Despite its beneficial properties and intriguing applications, Cs_2AgBiI_6 still requires further detailed research to address existing difficulties. These issues are not present in perovskites made of double iodides, which show improved properties and straight band transitions [50]. Cs_2AgBiI_6 is thermodynamically unstable. The energy conversion ratio (PCE) of solar devices connected to Cs_2AgBiI_6 is greatly limited by its huge indirect band gap. The basic structural, optical, electrical, and thermal properties of this chemical are not entirely

comprehended [46].

I.1 Research aims/objectives

The aim of the dissertation is to conduct a study, utilizing numerical simulation, of two different perovskite solar cell architectures. This investigation leverages the advanced simulation capabilities provided by SILVACO-ATLAS software [51]. The initial structure is derived from the double perovskite compound Cs_2BiAgI_6, while the subsequent structure is based on the methylammonium lead iodide compound $CH_3NH_3PbI_3$. The selection of these particular perovskite materials was made to facilitate a thorough examination of their individual characteristics and effectiveness in solar cell applications. The overarching objective is to gain valuable insights and contribute to the advancement of perovskite solar cell technology through a comparative analysis of these two architectures.

I.2 Structure of thesis

This thesis is structured as follows:

- **Chapter I**: In this initial chapter, a comprehensive introduction is provided, delving into the historical context and the most recent advancements in the efficiency of perovskite solar cells.
- **Chapter II**: In the following chapter, a comprehensive analysis is conducted on the distinctive properties and underlying principles of perovskite materials. Additionally, a thorough exploration is undertaken on a diverse array of photovoltaic cell architectures based on perovskite, along with the corresponding characteristic parameters used to assess their performance.
- **Chapter III**: This chapter provides a comprehensive overview and delves into the intricate details of the numerical software SILVACO TCAD that has been utilized in the present study.
- **Chapter IV**: In this chapter, we present a comprehensive analysis and optimization of different perovskite solar cell structures by incorporating two distinct perovskite materials, namely Cs_2BiAgI_6 and $CH_3NH_3PbI_3$. Through numerical simulation, we aim to enhance our understanding of the performance and efficiency of these structures.

Chapter II

Perovskite materials in solar cell technology

Chapter II

Perovskite materials in solar cell technology

II.1 Introduction

Organic solar cells (OSCs) have been acknowledged as a feasible and ecologically sustainable substitute for conventional inorganic solar cell technology in the generation of electrical power. The devices are produced through the utilisation of low-temperature solution processing, a method recognised for its effectiveness in capturing solar energy, cost-effectiveness, quick energy payback period, and basic mechanical flexibility [52].Furthermore, organic solar cells (OSCs) have garnered significant consideration due to their advantageous features, such as economics, adaptability, partial transparency, lack of toxicity, and applicability for high-volume roll-to-roll manufacturing in comparison to alternative photovoltaic technologies. Significantly, based on the comprehensive research-cell efficiency table given by the National Renewable Energy Laboratory (NREL), The power conversion efficiency (PCE) of organic solar cells (OSCs) has noticeably and quickly heightened in recent years. Recent progress in organic solar cells (OSCs) have achieved an officially recognised power conversion efficiency (PCE) of 18.2%, indicating their promising prospects for future practical uses [53]. In this chapter, our focus will be on the materials upon which the studied solar cell relies. These materials constitute the active region responsible for light absorption, namely Perovskite, and wide-band semiconductors utilized as layers for transporting free carriers.

II.2 Overview of organic solar cells

In the beginning, organic solar cells (OSCs) were only made of one organic semiconductor material and were built as single-layer devices. Over time, the architecture of these solar cells experienced a transformation, developing into a dual-layer structure that included donor and acceptor components. The evolution of OSCs into the bulk heterojunction (BHJ) structure took

place with time, with the donors and acceptors becoming mixed together. In 1995, Heeger et al. developed BHJ solar cells by combining fullerene acceptors and conjugated polymer donors in the absorber layer. This approach was subsequently refined by incorporating supplementary charge transporting and/or interfacial layers [54–56].

The BHJ structure is now regarded as the prevailing architecture for Organic Solar Cells (OSCs) since it efficiently tackles the issues related to the restricted migration distance and strong binding energy of excitons in organic materials. Recently, a revolutionary method called the layer-by-layer (LBL) growth methodology has been proposed, wherein the sequential deposition of acceptor and donor layers is employed [57]. The process involves the successive deposition of donor and acceptor layers to create a structure similar to a p-n junction [58]. The described method creates a pseudo-planar-heterojunction with a vertical profile, which improves charge transport and achieves a power conversion efficiency (PCE) similar to that of a bulk heterojunction (BHJ) device [59]. Furthermore, the utilisation of a roll-to-roll process enables precise control over the morphology of individual layers, making it particularly suitable for large-scale manufacturing [54, 60].

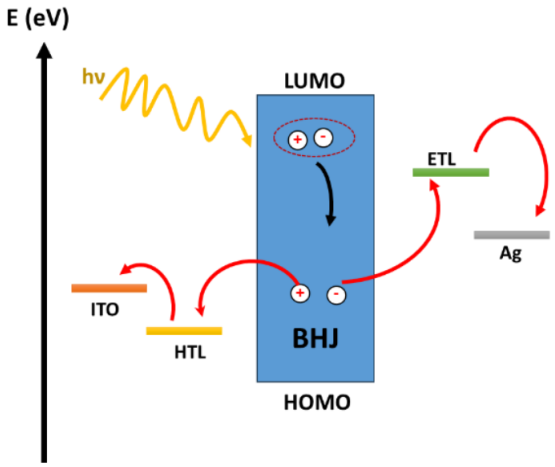

Figure II.1: The device architecture and operational principles of BHJOSCs [61].

Figure II.1 illustrates the basic structure and operational concept of organic solar cells (OSCs). When organic semiconductors absorb photons, electrons are excited to the lowest unoccupied molecular orbital (LUMO), while at the same time, holes are created in the highest occupied molecule orbital (HOMO) [62]. The presence of electron-hole pairs (excitons) in organic semiconductors can be attributed to the high Coulomb binding energy resulting from their low dielectric constant. The excitons move towards the donor-acceptor material interface through diffusion, where they undergo separation into free charges. An internal driving force, derived from the energy difference between the donor's and the acceptor's lowest unoccupied molecular orbitals (LUMO and HOMO, respectively), facilitates this process. In the end, the electric field between the cathode and anode will separate the carriers while delivering them to the electrodes. Hence, the optimal magnitude of the domain size, the interconnectivity be-

tween the donor and acceptor materials, and the distribution of components along the vertical axis collectively exert a synergistic influence on the dissociation of excitons and the transport of charges, ultimately dictating the performance of the device [54].

II.3 Wide band gap semiconductors

Wide-band-gap (WBG) semiconductors have received significant attention due to their wide range of applications, including thin-film transistors, transparent contacts, high-power devices, and photovoltaic devices [63]. Extensive research has been conducted on a range of wide bandgap (WBG) semiconductors, specifically post-transition-metal oxides including In_2O_3 , Ga_2O_3 , ZnO , SnO_2 , and their alloys. These materials have garnered significant attention due to their exceptional electrical properties and notable transparency to visible light [64–68]. Wide bandgap semiconductors play a critical role in enhancing the performance and durability of perovskite solar cells when used as either a hole transport layer (HTL) or an electron transport layer (ETL).Semiconductors exhibit distinctive characteristics, including significant bandgap energies, that enable effective transportation of charge carriers, thereby minimising recombination losses and enhancing the overall performance of the devices [69].

In the context of hole transport layers (HTLs), the utilisation of wide bandgap semiconductors facilitates the efficient extraction of holes from the perovskite layer. This, in turn, enhances the movement of positive charges towards the electrode. On the contrary, the function of an electron transport layer (ETL), facilitates the effective extraction and transportation of electrons towards the layer responsible for electron collection. The incorporation of wide bandgap semiconductors as hole transport layer (HTL) or electron transport layer (ETL) constituents in perovskite solar cells represents a promising approach towards attaining enhanced conversion efficiencies and improved stability. This advancement holds the potential to propel the development of renewable energy technology to new heights [69].

Titanium dioxide TiO_2 is a widely utilised wide bandgap semiconductor in perovskite solar cells, often serving as an electron transport layer (ETL). Titanium dioxide TiO_2 exhibits a bandgap energy that is suitably aligned with the perovskite layer, facilitating the effective transfer of charges at the interface. The perovskite layer's ability to exhibit transparency within the visible spectrum results in minimal absorption of light, thereby optimising light capture. Spiro-OMeTAD (2,2',7,7'-tetrakis(N,N-di-p-methoxyphenylamine)9,9'-spirobifluorene) is a commonly utilised wide bandgap semiconductor, predominantly employed as a hole transport layer (HTL). SpiroOMeTAD demonstrates a notable capacity for hole mobility, thereby facilitating efficient hole transportation and accumulation. This characteristic performs a vital function in boosting photocurrent and heightening the overall efficiency of solar cells [69].

Gallium oxide Ga_2O_3 is a semiconductor material that exhibits significant potential, owing to its wide band gap, rendering it an appealing choice for diverse solar cell applications [69]. The categorization of Ga_2O_3 as a semiconductor possessing a substantial bandgap $(E_g 4.23\tilde{}5.24eV)$

and its optical transparency render it a captivating substance for utilisation in electronic applications [70]. While Ga_2O_3 is generally non-conductive in its stoichiometric state, it has the otential to exhibit n-type conductivity when doped with silicon or tin [71]. Similar to aluminium, gallium is also considered a p-type dopant in silicon. Consequently, Ga_2O_3 exhibits the potential to serve as a source of p-type dopant through thermal diffusion or laser processing techniques. Moreover, the analysis of the energy band structure of Ga2O3 indicates its potential application as a carrier-selective contact for crystalline silicon [72].

The previously mentioned features have led to investigations regarding the utilisation of Ga_2O_3 in the field of photovoltaics. In their study, Chandiran et al [69] utilised Ga_2O_3 as an electron tunnelling interlayer in a dye-sensitized solar cell. This interlayer was positioned between the porous TiO_2 layer, responsible for electron collection, and the dye responsible for absorption. The utilisation of Ga_2O_3 served to minimise the electron back reaction within the electrolyte, thereby leading to an augmentation in the open circuit voltage (V_{oc}) of the device. Ga_2O_3 has been demonstrated to successfully passivate the surfaces of crystalline silicon and minimize the density of defects present in crystalline silicon solar cells [73]. According to current research conducted by Minami et al and Lee et al, Ga_2O_3 was employed as a buffer layer in cupric-based heterojunction thin film solar cells. This buffer layer was positioned between the p-type Cu_2O layer and the electron collecting ZnO:Al layer. The utilisation of a Ga_2O_3 buffer layer at the interface between cupric-AZO resulted in a decrease in charge carrier recombination, facilitating the transfer of electrons to the negative terminal of the device. As a consequence, the open-circuit voltage (V_{oc}) was enhanced [73, 74].

II.4 Perovskite materials for solar cells

II.4.1 Overview of perovskite materials in solar cell technology

In recent years, the utilisation of perovskite materials has significantly transformed the solar cell technology domain, presenting sympathetically resolutions to the prevailing global energy crisis. Perovskites, which derive their name from their crystal structure resembling that of the naturally occurring mineral, demonstrate remarkable light-absorption and charge-conduction characteristics, rendering them highly suitable contenders for photovoltaic purposes.

The ease of manufacturing, affordability, and potential for achieving high levels of efficiency have garnered significant interest among scholars and professionals in the renewable energy sector. Perovskite solar cells have demonstrated substantial advancements, attaining notable power conversion efficiencies that are comparable to those of conventional silicon-based solar cells. In addition, the integration of these components into devices that are both flexible and lightweight presents intriguing prospects for the field of wearable electronics and other non traditional applications. Despite the existence of challenges related to stability and toxicity, the current endeavours in research and development about perovskite materials hold the potential to

contribute to a more promising and environmentally friendly future in the field of solar energy utilisation.

As researchers strive to break down the limits of perovskite solar cell technology, several key advancements have been made to address its limitations. Efforts are being made to strengthen the long-term stability of perovskite materials, making them more resistant to moisture, heat, and other environmental factors that can degrade their performance over time. Novel encapsulation techniques and the development of more stable perovskite compositions have shown promising results in extending the lifespan of these solar cells.

Furthermore, the issue of toxicity associated with some perovskite formulations has been a subject of intense investigation. Scientists are actively exploring environmentally friendly and less toxic alternatives, ensuring that the manufacturing and disposal processes of perovskite solar cells are sustainable and safe for the environment. Collaboration between academia, industry, and government institutions has accelerated the commercialization of perovskite solar cell technology. Large-scale manufacturing processes are being developed to bring perovskite solar cells to the market, making them more accessible to a broader audience. The versatility of perovskite materials has also led to exciting developments in tandem solar cells. Scientists are trying to increase the efficiency of perovskite cells by catching more of the sun's spectrum by mixing them with other semiconductor materials, such as silicon or organic photovoltaics.

The overview of perovskite materials in solar cell technology portrays a compelling narrative of progress and potential. As research continues and technological hurdles are overcome, perovskite solar cells may soon become a mainstream renewable energy source, contributing significantly to the global shift towards a cleaner and more sustainable future. With their impressive efficiency, ease of manufacturing, and versatility. Perovskite solar cells will be very important for green energy and will help us get closer to a world with no carbon emissions.

II.4.2 Perovskite Materials

Perovskites, which are extensively studied materials in scientific research, are distinguished by their ABX_3 structure. Typically, perovskite compounds are designated as ABX_3, wherein A and B represent cations of diverse dimensions, while X signifies a shared bound anion. Metal-halide perovskites have attracted significant attention in the field of research, primarily focusing on leadbased perovskites denoted by the structural formula $APbX_3$. These perovskites exhibit distinctive physical and chemical properties, contributing to their widespread investigation. The A component can encompass both organic and inorganic cations, for example methylammonium, formamidinium, or Cs^+, B represents divalent metal cations (Pb or Sn) while the X component represents halide ions, including iodide, bromide, or chloride. Figure II.2 provides a visual representation of the atomic configuration within a perovskite compound. Perovskites made of metal halides have recently come to the forefront of the semiconductor industry, particularly in photovoltaics [17, 75–77].

The structure of perovskite, as depicted in Figure II.2, consists of corner-sharing octahedra $BX_6{}^{4-}$. These octahedra are formed by a hexacoordinated B-site cation surrounded by six X-site halide anions. The bonding between these ions within the octahedra is established through a combination of ionic and covalent interactions. The octahedral framework consists of wide voids located between every eight $BX_6{}^{4-}$ entities, which serve as the location for the A-site cation. The main role of the entity under consideration is to counterbalance the electric charge present inside the crystalline structure, so exerting a significant impact on its overall arrangement, The primary nature of the interactions between the A-site cation and the inorganic octahedra is predominantly electrostatic in nature [78].

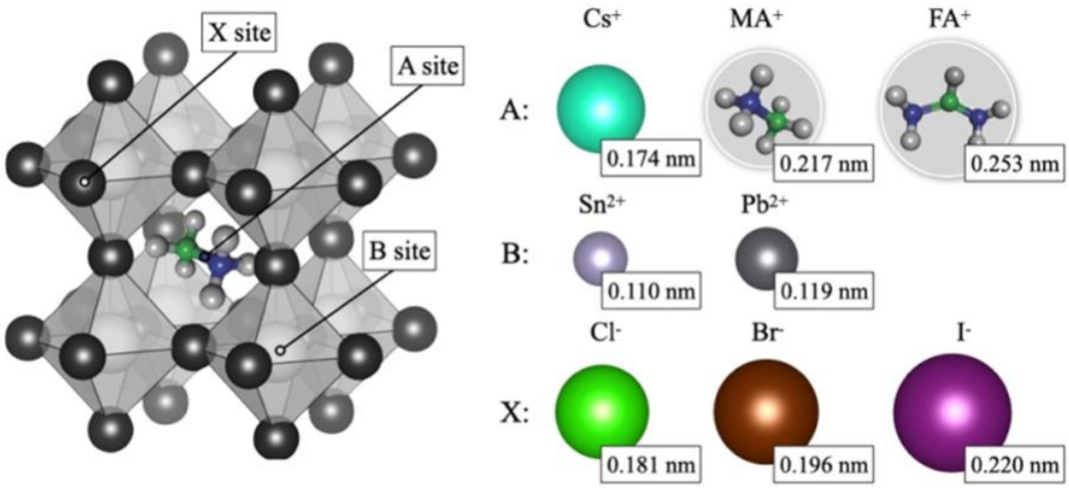

Figure II.2: The perovskite structure consists of eight inorganic $BX_6{}^{4-}$ octahedra that are connected at their corners, with an A-site cation positioned within the space created by these octahedra. Displayed on the right are instances of ions capable of occupying every site inside the ABX_3 structure, along by their respective ionic radii [78].

II.4.2.1 Types of perovskite materials

Perovskites can be categorized into two groups based on their cation: inorganic perovskites and hybrid perovskites. Nevertheless, perovskites can be categorized as either halide or non-halide depending on the X anion. The X anion of halide perovskites contains a halogen substance, which allows them to convert energy very efficiently; non-halide perovskites, on the other hand, are less poisonous and more stable. If we consider hybrid perovskites from an ecological perspective, we can divide them into two categories: toxic and non-toxic. It should be noted that B and X might be either simple or mixed materials, (as $B = Sn_{1-x}Pb_x$ or $X = I_{3-x}Br_x$) [79].

- **$MAPbI_3$**:The methyl ammonium lead halide is the toxic element in the hybrid perovskites group because it has lead in the cation B position. But it has a better light absorption rate,

which makes it the best choice for use in perovskite solar cells. At a thickness of $550nm$, its effective absorption coefficient for visible light is about $1 \cdot 10^{-5}((mol.L^{-1}))^{-1} \cdot cm^{-1}$. This means that it can take in all the light in the film. The diffusion lengths of $MAPbI_3$ are $L_n = 130nm$ for electrons and $L_p = 100nm$ for holes. The material exhibits excellent electrical conductivity and possesses a desirable bandgap of approximately $1.55eV$, which closely aligns with the optimal value for a single junction solar cell [79].

* **Double Perovskite**:Several theoretical investigations have shown that the outstanding photovoltaic characteristics of Pb halide perovskite can be primarily attributed to the distinctive electronic configuration of Pb 6s26p0 and the high symmetry of the ABX_3 structure [3]. However, perovskites made of lead halide are poisonous and can harm humans and the environment. Researchers have developed many lead-free perovskite materials to meet the growing need for nontoxic lead-free PSCs. Lead based perovskites have been substituted by harmless elements such as bivalent Sn^{2+} and Ge^{2+}. Because of lattice instability caused by the oxidation of Sn^{2+} and Ge^{2+}, lead-free PSCs are not very stable [80]. Furthermore, Sn exhibits a higher level of toxicity to humans compared to Pb when it becomes concentrated in the environment [3]. Bi^{3+} and other heterovalent M^{3+} halides are stable semiconducting halides that are non-toxic and can replace Pb^{2+}. The reduced intrinsic trap concentrations and defect states in bismuth-based PSCs cause the charge carrier diffusion lengths to be longer. When a highly charged Bi^{3+} ion is introduced to the three-dimensional $A^{1+}M^{2+}X_3$ structure, its opto-electronic characteristics are inferior to those of the lead-based perovskite [81].

  In order to deal with these unfavourable characteristics, the Elpasolite structure, which is also referred to as the double perovskite structure, has been employed by including the Bi^{3+} anion. The Elpasolite structure is characterized by the generic formula $A_2B^{I}B^{III}X_6$ as shown in Figure II.3, where A represents a monovalent cation, X represents a halide anion (Br^-, Cl^-, I^-), BI represents an inorganic cation (Cu^+, Ag^+, Au^+, Na^+, K^+, Rb^+, and In^+), and BIII represents an organic or inorganic cation (Bi^{3+} or Sb^{3+}) [80]. Due to the vast number of possible combinations, there are theoretically more than 100 double perovskite materials that possess appropriate tolerance factors and thermodynamic stability. Several double perovskite compounds have been produced effectively in recent times. These include Cs_2NaBiI_6,$Cs_2AgInCl_6$, Cs_2AgBiX_6 [3].

  Recent studies have demonstrated that Bi^{3+}-based double perovskites containing the monovalent cation Ag^{1+} exhibit highly promising characteristics for use in photovoltaic applications. These include a desirable band gap, comparable effective masses of charge carriers, excellent photoluminescence lifetime, extended lifetimes for carrier recombination, and high stability. When compared to $CH_3NH_3PbX_3$, McClure and his colleague found that $Cs_2AgBiBr_6$ and $Cs_2AgBiCl_6$ have a better band gap and are more stable. However, $Cs_2AgBiBr_6$ and $Cs_2AgBiCl_6$ are not very efficient because they have large charge car-

rier effective masses, poor charge carrier transport abilities, and a high band gap ($> 2eV$). Unfortunately, this means these materials cannot be inserted into solar cells. In contrast, the Cs_2AgBiI_6 absorber demonstrated a desirable band gap of$1.12eV$, superior light absorption capabilities, and improved overall performance compared to $Cs_2AgBiBr_6$ and $Cs_2AgBiCl_6$. These characteristics make it well-suited for use in the PSC [80].

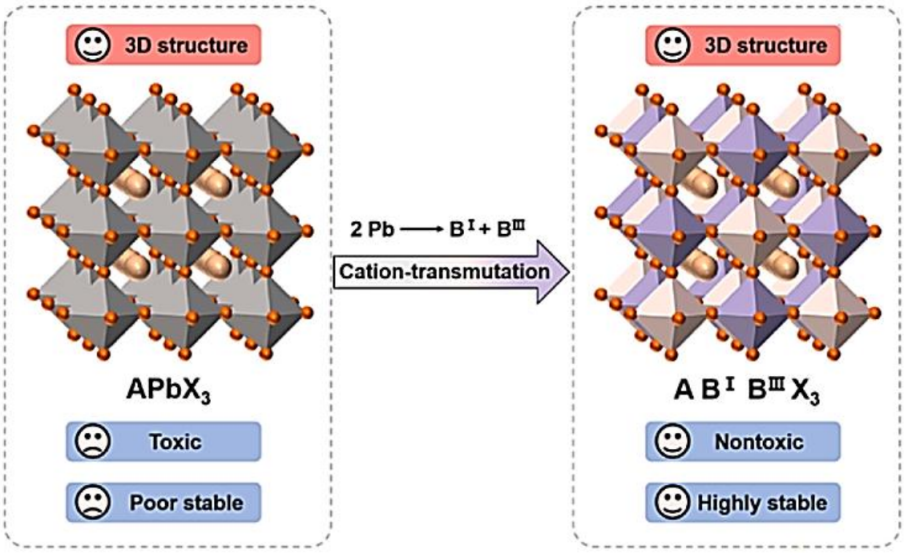

Figure II.3: Comparative analysis of the composition and properties of lead-based perovskite and double perovskite structures [3].

II.4.3 Properties of perovskite materials

Based on the features of perovskite technology, perovskite materials are often used as light absorbers in solar cells. The remarkable thermal stability and very high degree of structural orderedness exhibited by the inorganic components of the organic-inorganic hybrid perovskite materials have mainly attracted a great deal of interest. Additionally, the characteristics of the organic component, such as functional versatility, mechanical flexibility, and cost-effectiveness in processing, have contributed to the interest in these materials. Therefore, the exploration of the potential combination seen in traditional inorganic crystals with molecular organic solids has sparked new scientific investigations into the multifaceted qualities exhibited by organic-inorganic hybrid perovskite materials [82]. n greater depth, organic-inorganic hybrid perovskite materials exhibit promising possibilities for use in solar systems. The following items are included:

- The light-harvesting capabilities of the material have been reported to be excellent, and it also exhibits good hole transportation properties.

- The potential for an affordable processing cost.

- The utilisation of printing techniques for low-temperature solar cell fabrication is highly desirable since it enables the deposition of solar cells on flexible substrates.

- The phenomenon of increased light absorption leads to a subsequent rise in the creation of free charge carriers through the process of photogeneration. This promotes a reduction of energy dissipation by the generated charges and improves the concentration of these charges at the electrodes.

- The short duration required to recover the energy invested is attributed to the combination of cheap processing costs and high efficiency. The energy payback time refers to the period required for solar cells to generate an amount of energy that is equal to the energy consumed during their manufacturing. A material that exhibits both low production cost and good performance can result in a reduced payback time [82].

To date, an enormous number of hybrid organic-inorganic halide perovskite materials have been synthesised and utilised as absorber layers. The $CH_3NH_3PbI_3(MAPbI_3)$ perovskite material has garnered significant attention in academic research owing to its exceptional photoelectric characteristics. These features can be summarised as follows:

1. **Wide absorption range**:

   The perovskite material $MAPbI_3$ has a bandgap of around $1.5eV$, which aligns with the Schotty barrier theory. This bandgap enables the material to effectively absorb the full visible spectrum ranging from $300nm$ to$800nm$. Consequently, it demonstrates a remarkable capacity for efficiently utilising sunlight, leading to the generation of a substantial current by photoexcitation [83].

2. **Significant absorption coefficient**:

   The high absorption coefficient is crucial for attaining optimal performance in perovskite solar cells (PSCs). This characteristic allows for the efficient decrease in the desired thickness of the absorber layer, hence improving the efficiency of capturing photo-generated carriers. The perovskite material $MAPbI_3$ is well recognised as a direct semiconductor, exhibiting a significantly greater absorption coefficient compared to silicon materials [83]. In addition, it is worth noting that hybrid perovskites have a low effective mass for both electrons and holes. Consequently, charges exhibit a significant degree of mobility when subjected to room temperature conditions. The significance of these features lies in their ability to enable the charges to disperse across distances of several hundred nanometers before recombining, hence enhancing their collection. Moreover, this material has a remarkable resistance to crystal flaws, a characteristic that sets it apart from the majority of semiconductors [84].

3. **Long exciton diffusion length**:

   Transient photoluminescence measurement has established that the exciton diffusion length of polycrystalline $MAPbI_3$ materials is roughly 100 nm, which is significantly greater than the exciton diffusion length of organic semiconductors, estimated to be around $10nm$. The mixed halogen $MAPbI_{3-x}Cl_x$ has demonstrated an exciton diffusion length that surpasses $1m$. In a recent study conducted by Dong et al., it was demonstrated that the exciton diffusion length within a single $MAPbI_3$ perovskite crystal can extend up to $175m$. This notable achievement can be attributed to the crystal's singular nature, which possesses a reduced number of defects, enhanced carrier mobility, and an extended lifetime. This means that perovskite solar cells (PSCs) can improve their power conversion efficiency by successfully reducing the possibility of exciton recombination during transmission [84].

4. **Fast carrier mobility**:

   Perovskite materials can conduct both electrons and holes due to their bipolar carrier transport properties. The incorporation of this bi-functional performance significantly enhances the structural composition of the electronic devices. [83]. The study revealed that the hole and electron mobility of $MAPbI_3$ were measured to 12.5-66 and 7.5 $\frac{cm^2}{Vs}$, respectively. This indicates that there is a significant ability for efficient separation of photo-generated electrons and holes, resulting in the suppression of negative carrier recombination [83].

5. **Low exciton binding energy**:

   According to reports, the perovskite material $MAPbI_3$ exhibits an exciton binding energy of roughly $19meV$. At room temperature, the photoexcited exciton can undergo spontaneous dissociation upon exposure to light, resulting in the generation of a significant quantity of unbound electrons and holes. This process contributes to the observed photoabsorption phenomenon [83]. .

6. **Tunable bandgap**:

   One further benefit of perovskite materials is their capability to modify the bandgap by ion doping and replacement, hence achieving desired photoelectronic characteristics. In the context of$MAPbI_3$ perovskite materials, it is possible to substitute I- ions with Br^- or Cl^- ions, so that the formation of $MAPbBr_3$ and $MAPbCl_3$ perovskite materials. These substitutions lead to the generation of perovskite materials with distinct bandgaps. This method can considerably contribute in the development of perovskite electronics with enhanced colour features. The substitution of MA^+ ($CH_3NH_3^+$) with FA^+ $(CH(NH)_2)^{2+}$ is shown to result in enhanced photovoltaic performance due to the slightly greater ionic radius of FA^+. The bandgap of $FAPbI_3$ is approximately within the range of 1.45-1.52 $4eV$, in contrast to the bandgap of $MAPbI_3$ which is 1.95 eV. Furthermore, the substitu-

tion of Pb^{2+} with Sn^{2+} in $MASnI_3$ results in a bandgap of approximately 1.3 eV, hence expanding the absorption spectrum to include infrared light up to 1100nm [83].

II.5 Perovskite Solar Cells

In the past few years, there has been a significant increase in the academic study and advancement of third-generation (3G) solar cell technologies. These include solar cells based on copper/zinc/tin sulphide, dye-sensitized cells, polymer cells, quantum dot cells, organic cells, and perovskite based solar cells (PSCs). From this selections, perovskite solar cells (PSCs) have attracted considerable attention and have emerged as the technology that is advancing fast in this particular industry. Perovskite solar cells (PSCs) have demonstrated the capacity to effectively produce power, along with the benefit of cost-effectiveness, positioning them as a highly viable contender for the substitution of traditional solar cells [31].

Solar cell technology, which possesses abundant resources, sustainability, renewability, and employability, is being proposed as an environmentally friendly option to address the upcoming energy problems. The first and second generations of solar cell technologies, which rely on silicon and thin films, present notable obstacles. These challenges encompass extended energy payback periods, increased costs primarily due to the heightened purity standards for the active material, limited availability of resources, suboptimal efficiencies in low illumination settings, and deficiencies in terms of flexibility, design, and opacity.

Since 2012, solid-state perovskite solar cells (PSCs) have emerged as a promising and revolutionary cost-effective third-generation photovoltaic (PV) technology. Perovskite solar cells (PSCs) demonstrate remarkable photovoltaic (PV) efficiency and possess the advantageous characteristic of being easily processed at low temperatures. These qualities render PSCs particularly versatile for integration into printed and flexible electronics, as well as the smart textile industries. The multifunctionality and wide range of uses of perovskite solar cells (PSCs) possess the ability to significantly transform the photovoltaic industry, offering an optimal resolution to the constraints associated with earlier solar cell technologies [85].

II.5.1 Types of perovskite solar cells and their structures

A typical PSC (perovskite solar cell) comprises five essential layers, each serving a specific purpose in its operation. These layers include the conducting substrate (ITO/FTO), the hole transporting layer (HTL), the perovskite light-absorber layer, the electron transporting layer (ETL), and the metal electrode Au/Ag [86]. The active or absorption layer of perovskite is located between the electron transport layer and the hole transport layer. The overall performance of Perovskite devices is greatly affected by the extraction of charge carriers at the electron transport layer (ETL) and the hole transport layer (HTL). The primary role of the ETL (electron transport layer) or HTL (hole transport layer) is to make it easier for electrons (or holes) to be

extracted and transferred from the absorber layer to the anode (or cathode) while simultaneously preventing the movement of holes (or electrons).

Typically employed HTL materials exhibit a HOMO value that surpasses the absorber layer by a tiny margin. Some examples of organic materials include Spiro-OMeTAD,PTAA, P3HT, PEDOT: PSS, Poly-TPD, and EH44. Inorganic materials include CuSCN, NiO, CuO, CuCrO, CuI, and CrO. In order to facilitate the transmission of a greater number of photons to the absorber layer, it is necessary for the ETL materials to possess enhanced transmittance in the ultraviolet (UV) region. Additionally, the HOMO and LUMO values of the ETL materials should surpass those of the active layer [87]. Furthermore, it is imperative for the ETL (electron transport layer) to exhibit stability in both air and moisture, while also being adaptable to low-temperature processing. These characteristics are crucial in enhancing the longevity of perovskite solar cells and facilitating their fabrication procedures [88].

Some examples of materials include TiO_2, SnO_2,ZnO, PCBM, C60, and Al_2O_3 [87]. The electron transport layer is frequently comprised of TiO2, an n-type metal oxide, because to its notable characteristics such as a high band gap and high transmittance. In the same way, organic electron transport layers of the n-type have been utilised, which are composed of $[_{6}$,$_{6}]-$phenylC_{61}butyricacidmethylester PCBM, C60, and their respective derivatives. The utilisation of inorganic metal oxide charge transport materials has been found to be an efficient strategy for enhancing the stability of perovskite solar cells in the presence of moisture. In recent studies, certain research groups have been substituting organic n-type materials with inorganic compounds. The better stability of metal oxide semiconductors in the presence of oxygen and moisture, as well as their increased charge mobility, is widely acknowledged in comparison to the aforementioned organic charge transport materials [37].

Commonly employed transparent conducting oxide (TCO) materials include indium tin oxide (ITO), fluorine-doped tin oxide (FTO), indium zinc oxide (IZO), and aluminum-doped zinc oxide (AZO), as well as various anodes such as gold (Au), silver (Ag), copper (Cu), chromium (Cr), molybdenum oxide (MoO), or zinc oxide/aluminum (ZnO/Al) [87]. There exist two fundamental configurations for this device: one incorporates a mesoporous TiO_2 layer, therefore referred to as the mesoporous structure (as depicted in Figure II.4), while the other is missing the mesoporous layer and is denoted as the planar structure (as illustrated in Figure II.4 [88]. The mesoporous structure, as depicted in Figure II.4, has a substrate composed of Fluorinedoped Tin Oxide (FTO) and Indium Tin Oxide (ITO), a hole-blocking layer, and a scaffold that can be either conductive Titanium Dioxide (TiO_2) or insulating Aluminium Oxide (Al_2O_3).

Additionally, the structure includes a perovskite absorber, a hole transport layer (HTL), and the top metal contact electrode [86] . The perovskite material has to be inserted into the mesoporous titanium dioxide (TiO_2) scaffold within the mesoporous device. According to a study carried out by Snaith et al., the researchers replaced the mesoporous TiO_2 material with insulating Al_2O_3 in the experimental device, and observed that the device continued to function effectively. This observation suggests that perovskite has the potential to serve as both a light-

harvesting material and an electron-transporting layer, so enabling the construction of a photovoltaic device without the need for a mesoporous layer. The mesoporous device construction has demonstrated a high efficiency of around 23%. Nevertheless, the elevated sintering temperature necessary for the formation of the mesoporous layer not only results in longer processing duration but also contributes to the overall expenses incurred during cell manufacture [88].

One advantage of planar perovskite solar cells is the relative ease of their production due to the absence of high-temperature procedures [36]. The study conducted by Zhou et al demonstrates a 20% efficiency achieved by the implementation of a planar structure [89]. This finding supports the rationale behind the elimination of the mesoporous layer, as depicted in Figure II.4 . This phenomenon occurs due to the high collect ability of electrons by the electron transport layer, even in the absence of a mesoporous layer, as evidenced by the charge diffusion length of perovskite materials [88].

Planar and mesoporous perovskite solar cells (PSCs) can be categorised into two distinct forms, which are determined by the arrangement of charge-transporting layers within the devices. These sorts of devices are referred to as conventional n-i-p structures and inverted p-i-n structures [86] ; When the incident light passes through the TCO/ETL side, it is referred to as an n-i-p or conventional structure. Conversely, if the light penetrates through the HTL side, it is denoted as a p-i-n or inverted structure [87] Hence, there exist four primary potential alternatives for the device designs depicted in Figure II.4.

- TCO/ETL/Mesoporous ETL/Perovskite/HTL/Electrode (n-i-p).
- TCO/HTL/Mesoporous HTL/Perovskite/ETL/Electrode (p-i-n).
- TCO/ETL/Perovskite/HTL/Electrode (n-i-p).
- TCO/HTL/Perovskite/ETL/Electrode (p-i-n).

The perovskite layer exhibits ambipolar behaviour, allowing for the independent separation and transportation of electrons and holes. Consequently, the aforementioned configurations are then diminished in the manner described below.

- TCO/Perovskite/HTL/Electrode (ETL-free device).
- TCO/ETL/Perovskite/Electrode (HTL-free device).

The PSCs without a charge transport layer have demonstrated their suitability for reducing manufacturing expenses and enhancing efficiency. The ETL-free configuration can be realised by employing a consecutive layer deposition technique to deposit the perovskite absorbing layer directly onto the surface of the transparent conducting oxide. Despite the superior efficiency and stability of the HTL-free PSCs arrangement, it is costly and significantly raises the manufacturing expenses [90].

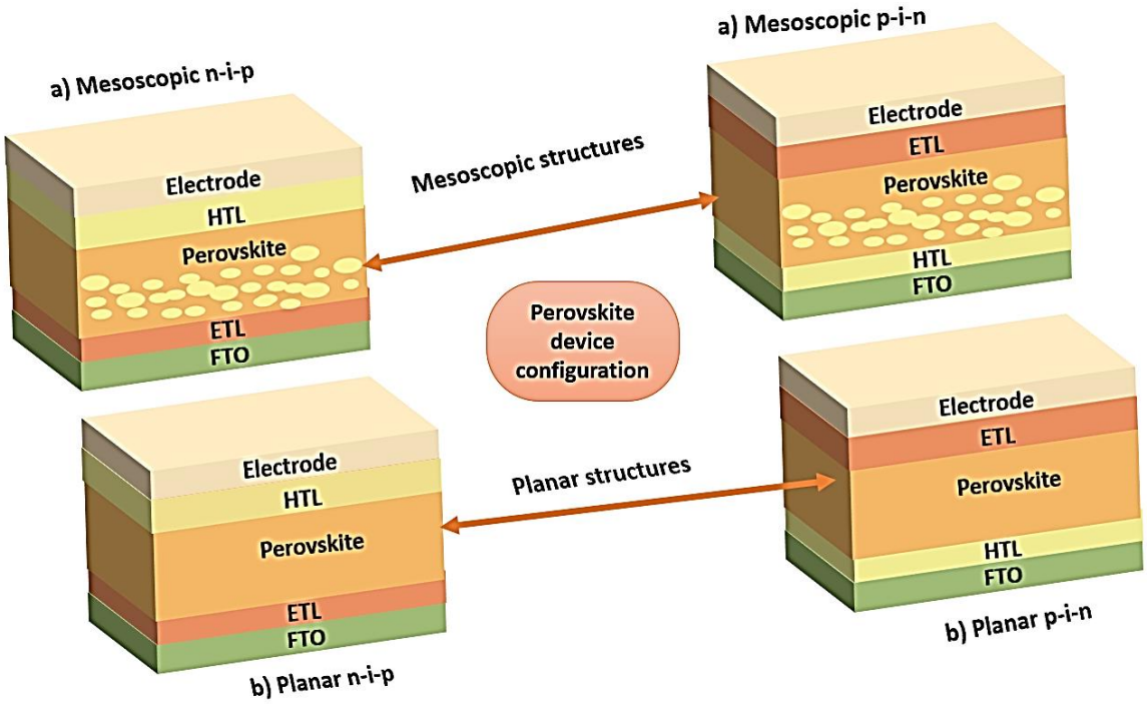

Figure II.4: perovskite solar cell architectures [87].

II.5.2 Working mechanism of perovskite solar cells

The process by which the PSC operates can be comprehended by examining the operational principles of the DSSC and organic photovoltaic technologies. In perovskite solar cells (PSCs), perovskite is used as a light sensitizer, analogous to the function of dye in dye-sensitized solar cells (DSSC). The photovoltaic solar cell (PSC) carries out four essential functions: the generation of an exciton, which is an electron-hole pair, through the absorption of photons, the exciton diffusion, the transportation of charges, and the extraction of charges [91]. Figure II.5 illustrates the energy level matching diagram of the materials within the perovskite device, showcasing the alignment between different components. To optimise the power conversion efficiency (PCE) of the device, it is imperative to ensure an adequate alignment of energy levels throughout each layer. The primary operational mechanism of perovskite solar cells can be in brief described as a sequence of four sequential processes [83].

1. **Absorption of Photons:** As depicted in Figure II.5, when the solar cell is subjected to solar radiation, the perovskite material absorbs the incident light, resulting in the generation of excitons, which consist of electrons and holes. The formation of free carriers occurs as a result of excitons, which arise from the disparity in binding energy between perovskite materials. This phenomenon subsequently leads to the generation of electric current.

2. **Exciton diffusion:** The formation of free carriers occurs as a result of excitons because of the hybrid perovskites' low exciton binding energy [92].This phenomenon subsequently leads to the generation of electric current [88]. While the holes stay at the HOMO level

(or valence band),the electrons created by light are transported to the energetically excited lowest unoccupied molecular orbital (LUMO) level (or the conduction band) [83].

3. **Charge carrier separation:** The produced free electrons and holes are subsequently distinguished at the interfaces of the electron transporting layer (ETL) and hole transporting layer (HTL) through the utilisation of their respective electron and hole transporting layers.

4. **Charge carrier transportation and collection:** Subsequently, the electrons originating from the perovskite material are transmitted to the electron transport layer (ETL), whereas the holes are transmitted to the hole transporting layer (HTL). Ultimately, the TCO collects the electrons from the ETL, while the metal back electrode collects the holes. The transparent conducting oxide (TCO) and metal back electrode are electrically linked to generate a photocurrent within the external circuit. The better photovoltaic output of perovskite solar cells (PSCs) is due to the high carrier mobility and extended diffusion length exhibited by perovskite materials [88].

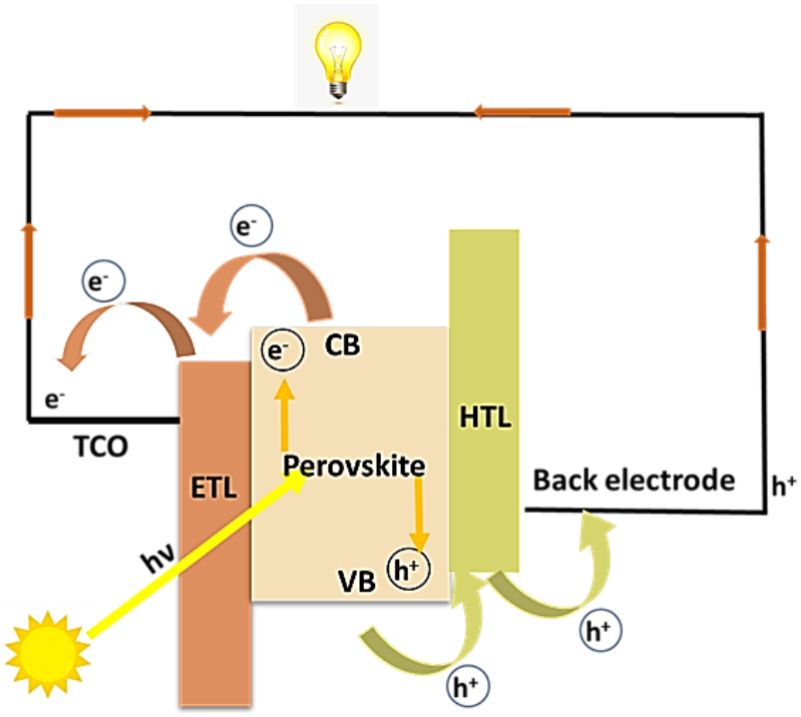

Figure II.5: Working mechanisms of perovskite solar cells [88].

In order for the PSC (Photovoltaic Solar Cell) to operate well, it is imperative to meticulously design the energy levels associated with each layer. The reason for the recombination of excited electrons and holes is to minimise the overall energy. However, the charge carriers also exhibit energy conservation properties, resulting in their tendency to follow the path of least resistance. By implementing an appropriate layer structure, it is possible to impede a portion

of the recombination process within the cell by redirecting the charge carriers via an alternative pathway. This is achieved by ensuring that the energy level of the electron transport layer (ETL) lowest unoccupied molecular orbital (LUMO) is slightly lower than that of the active layer's LUMO. This arrangement facilitates a more favourable pathway for electron movement. The HOMO of the HTLs should ideally be somewhat higher than that of the active layer, facilitating a more favourable pathway for hole transport. The aforementioned observation holds true for each individual layer inside the cell. Specifically, each layer exhibits either a greater highest occupied molecular orbital (HOMO) or a lower lowest unoccupied molecular orbital (LUMO) in order to facilitate the effective transit of charge carriers, as depicted in FigureII.5 [93].

According to Marchioro et al., it was hypothesised that the separation of electron-hole pairs occurred at the two heterojunction interfaces of ETL/perovskite and HTL/perovskite. This was followed by the injection of electrons into ETL (process (i) in Figure II.6 and the injection of holes into the hole transport material (HTM) (process (ii)), facilitating the transport of charges. Simultaneously, the cell's performance may be compromised by a range of undesirable behaviours, including exciton annihilation (process (iii)), photoluminescence, nonradiative recombination, reverse transmission of electrons and holes (process (iv) and (v)), and recombination at the ETL/HTL interface (process (vi)). Figure II.6 illustrates the transport mechanisms of electrons and holes within an HTM/perovskite/ETL cell [94].

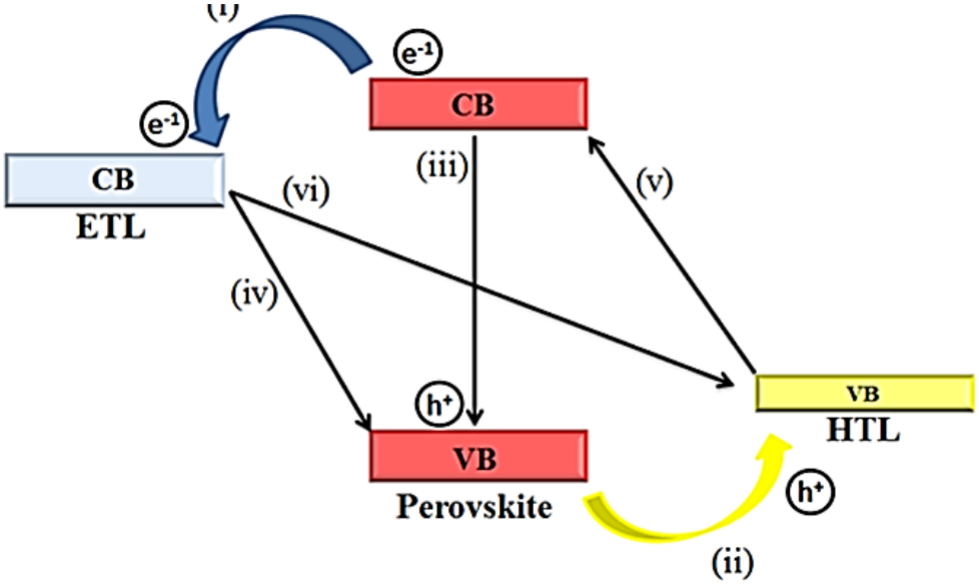

Figure II.6: Illustration depicting the mechanism of charge transfer and recombination in perovskite solar cells [94].

II.5.2.1 Excitons

Excitons represent a fundamental quantum unit of electronic excitation, where an electron with a negative charge and a hole with a positive charge are interconnected through electrostatic

attraction. when a solid absorbs photons, resulting in the creation of these particles [82].

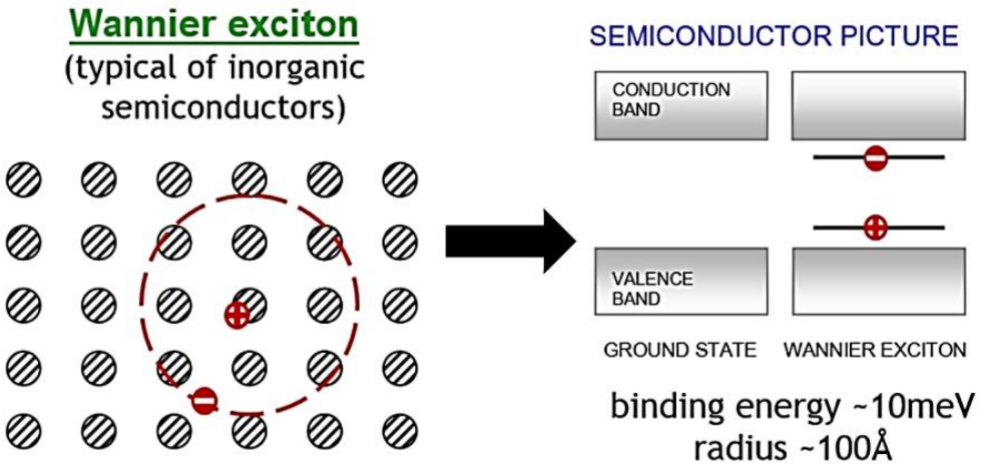

Figure II.7: A illustration of a Wannier-type exciton (b) Schematic representation of the energy bands in a semiconductor material [82].

Excitons can be classified into two categories, namely Wannier excitons (as shown in FigureII.7 (a) and Frenkel excitons (as depicted in FigureII.7 (a)), depending on their dimensions in relation to the interatomic or intermolecular distance within the material [82].

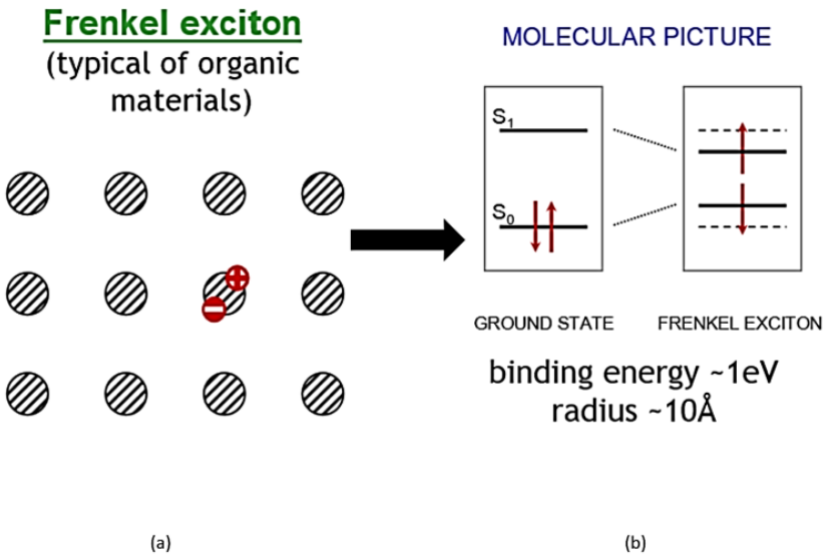

Figure II.8: Illustration of (a) Frankel-type exciton (b) depicting the molecular band diagram of an organic material [82].

Wannier excitons, which are commonly encountered in covalent semiconductors and insulators, exhibit a significant separation between the electron and hole, surpassing the atomic spacing. Consequently, the influence of the crystal lattice on the exciton is considered mini-

mal. Frenkel excitons predominantly appear in organic materials, such as molecular or rare-gas crystals. In these systems, the electron and hole have a separation distance that is comparable to the atomic spacing. Consequently, the exciton becomes localised to a singular site at any given moment. The movement of Wannier excitons can be described as resembling that of free particles, whereas the mobility of Frenkel excitons is observed as a process of hopping between different sites [82].

II.5.3 Basic parameters and electrical characterization methods

II.5.3.1 J-V Characteristics of a PV device

The electrical performance of solar cells is frequently evaluated by measuring their current-voltage characteristic. This is accomplished by setting a bias voltage V throughout the two terminals of the device and simultaneously determining the current I that passes through these terminals. Typically, the current density J is used over the current because it enables a direct comparison of solar devices of varying areas [95].

Under dark conditions, a solar cell exhibits diode-like behaviour and its properties can be described using the Shockley diode equation [95]:

$$J = J_0 \left[\exp\left(\frac{qV}{\eta kT} \right) - 1 \right] \tag{II.1}$$

J_0 represents the saturation current, η denotes the ideality factor (with $\eta = 1$ indicating an ideal diode), K indicates the Boltzmann constant, q indicates the elementary charge, and T indicates the temperature [95].

When the solar cell is exposed to light, the diode characteristic is altered in a negative direction due to the photo-current density produced by the solar device [95].

Figure II.9 illustrates the current-voltage characteristics. The J-V curve under illumination provides valuable information on several key parameters, including the short-circuit current density (J_{sc}), the open-circuit voltage (V_{oc}), and the fill factor (FF) [95].

Short circuit current density

J_{sc} represents to the current density that is measured when the device is in a short-circuit state, meaning that the terminals are connected without any electrical load [95]. Additionally; The short circuit current density (J_{sc}) refers to the highest amount of electric current density that passes through a solar cell while it is in a zero-load state. When the current at the maximum short-circuit condition (J_{sc}) is reached, the voltage across the solar cell will be reduced to zero. The short-circuit current density is caused by the creation and accumulation of light-induced charge carriers. The effectiveness of a solar cell is primarily determined by factors such as the quantity and spectrum of incident photons, the optical characteristics of the cell, the probability

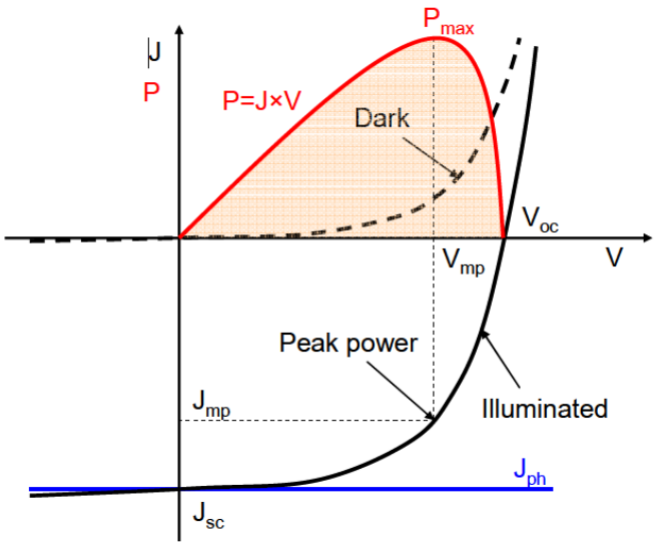

Figure II.9: Schematic depiction of the current-voltage characteristics (J-V) [82].

of photon collecting, and the cell's surface area. Figure II.9 displays the visual depiction of the short circuit current [96]. And it is given as the following equation:

$$J_{sc} = J - J_0(\exp\left(\frac{qV}{\eta kT}\right) - 1) \tag{II.2}$$

Open circuit voltage

The open circuit voltage (V_{oc}) refers to the voltage between the terminals of the solar cells when the device does not have a connection to an external circuit, also known as the open-circuit circumstance [95]. Also, we can define the open circuit voltage (V_{oc}) as the highest potential difference that can be obtained from a solar cell. When a solar cell is open-circuited, meaning there is no load attached to it, the current flowing through the solar cell will be at its minimum value of zero, while the voltage across the solar cell will be at its greatest value. The value of V_{oc} can be determined by equating the net current to zero in the solar cell equation II.1 [96].

$$V_{oc} = \frac{nKT}{q} \ln\left(\frac{J_L}{J_0} + 1\right) \tag{II.3}$$

The open circuit voltage (V_{oc}) is determined by the light generated (J_L) and the saturation current density (J_0), as shown in the equation above. The current density, denoted as J_0, is contingent upon the process of recombination within the solar cell. V_{oc} quantifies the level of recombination occurring within a solar cell. Figure II.9 displays the graphical depiction of open circuit voltage [96].

Efficiency

Efficiency is the quantitative measure of the ratio between the power produced by a solar cell and the power it receives as input. Solar cell efficiency is specifically specified within the range of operation from 0 to V_{oc}, when the solar cell is capable of delivering power. The equation II.4 provides the value for the output power density of a solar cell [96].

$$P_{max} = J_{max}V_{max} \tag{II.4}$$

The power (P_{max}) reached its maximum at the maximum power point of the cell, as depicted in II.9. The efficiency of a solar cell is determined by equation II.5.

$$\eta = \frac{J_{max}V_{max}}{P_s} \tag{II.5}$$

P_s is the power that comes from sunlight.

Equation II.5 can be reformulated with respect to the fill factor (FF), which serves as an indicator to evaluate the performance of a solar cell. The fill factor is determined by dividing the greatest power output of a solar cell by its theoretical power output. FF can also be understood as the ratio of the rectangular regions illustrated in Figure II.9, representing the maximum power point (MPP) and the theoretical maximum power P_{max} [96].

The fill factor is determined using the following equation:

$$FF = \frac{J_{max}V_{max}}{V_{oc}J_{sc}} \tag{II.6}$$

By rearranging equation II.6, we obtain the equation $(J_{max}V_{max} = FFJ_{sc}V_{oc})$. Substituting the value of $(J_{max}V_{max})$ into equation II.5 yields equation II.7 as follows [96].

$$\eta = \frac{J_{sc}V_{oc}FF}{P_s} \tag{II.7}$$

External Quantum Efficiency (EQE)

The quantum efficiency of a solar cell, comprising the internal quantum efficiency (IQE) and external quantum efficiency (EQE), is the ratio of collected charge to incident photons. The EQE is occasionally called $IPCE$, an acronym for incident photon-to-electron conversion efficiency. The term refers to the proportion of electrons produced in an external circuit (N_e) in relation to the quantity of incident monochromatic photons (N_p) per unit of time. The EQE value serves as an indicator of both the light capturing efficiency and the effectiveness of light into power. Hence, EQE plays a crucial role in evaluating the photovoltaic efficiency of PSCs [83]. The precise equation for EQE is as follows:

$$EQE = \frac{N_e}{N_p} = \frac{1240J_{sc}}{\lambda P_{in}} \tag{II.8}$$

In this equation, J_{sc} represents the short-circuit current density of photovoltaic solar cells (PSCs). λ denotes the wavelength of the incident monochromatic light, while P_{in} represents the power of the incident monochromatic light.

II.5.4 The advantages and disadvantages of perovskite solar cells

II.5.4.1 The advantages of perovskite solar cells

Perovskite materials provide inherent advantages in terms of their favourable optical and electrical properties, which make them better suited for solar applications when compared to traditional silicon-based materials. The principal features of perovskite include, but are not limited to,

- ❋ The material exhibits favourable optical characteristics and possesses a significant absorption coefficient;
- ❋ The capacity to effectively absorb solar energy;
- ❋ A high dielectric constant facilitates the facile passage of charge carriers;
- ❋ A high dielectric constant facilitates the facile passage of charge carriers;
- ❋ The simultaneous transmission of electron-hole pairs is facilitated by their beneficial diffusion length, which has been observed to exceed 1mm;
- ❋ The phenomenon of recombination losses being minimised
- ❋ The material costs are rather inexpensive;
- ❋ The possibility for anion/cation substitution as a method of adjusting the bandgap [79]

II.5.4.2 The disadvantages of Perovskite solar cell

Although perovskite solar cells have promising capabilities, they also encounter certain drawbacks. Below are several examples:

- ❋ The attainment of enhanced control over the structure of the film and the characteristics of the material is necessary;
- ❋ The utilisation of toxic materials such as lead cell instability;
- ❋ There is a significant sensitivity to humidity;
- ❋ material degradation and hysteresis;
- ❋ An issue in manufacturing is scalability, as the spin-coating technology utilized in lab tests is not suitable for large-scale production. For high throughput, roll-to-roll manufacturing must be adopted [79] ;

II.5.4.3 Comparison of perovskite solar cells with other types of solar cells

Perovskite materials belong to a category of chemicals that exhibit an identical crystal structure to that of calcium titanium oxide ($CaTiO_3$). Recently, there has been much focus on them because of their possible usefulness in solar cells. This interest stems from their advantageous characteristics,including their cost-effectiveness, superior efficiency, and ability to modify their band gap. This section aims to conduct a comparative analysis between perovskite solar cells and other types of solar cells, including silicon, cadmium telluride (CdTe), copper indium gallium selenide (CIGS), dey sensitized and organic solar cells [94].

Silicon is the predominant material employed in solar cell technology, constituting over 90% of the worldwide market share. Silicon-based photovoltaic cells have notable attributes including exceptional stability, durability, and performance. However, it is important to acknowledge several limitations associated with these cells, namely elevated expenses in terms of materials and processing, inefficient light absorption capabilities, and an increased vulnerability to impurities and defects. Perovskite materials provide the potential to surmount certain constraints due to their ability to be fabricated from inexpensive precursors, exhibit strong light absorption and charge carrier mobility, and undergo processing at reduced temperatures. Nevertheless, it is worth noting that perovskite materials present several obstacles, including inadequate stability when exposed to environmental conditions, the presence of harmful components, and issues in achieving large-scale production [97].

Two types of thin-film solar cells, namely CdTe and CIGS, are employed to convert sunlight into electrical energy by utilising thin layers of semiconducting elements. Thin-film solar cells have reduced material and processing expenses in comparison to silicon solar cells, while also possessing the advantageous characteristics of flexibility and lightweightness. Both cadmium telluride (CdTe) and copper indium gallium selenide (CIGS) have superior efficiencies compared to silicon solar cells, actually lower than those achieved by perovskite solar cells. Both CdTe and CIGS photovoltaic technologies raise environmental and safety problems. CdTe is problematic due to its inclusion of poisonous cadmium, while CIGS poses challenges due to its reliance on rare indium and gallium resources. Perovskite materials possess the potential to serve as a more sustainable and plentiful substitute for CdTe and CIGS, owing to their composition derived from readily available elements and the absence of toxic metals [98–100].

One notable benefit of perovskite solar cells, in comparison to alternative thin-film solar cell technologies, is the ample availability of precursor materials, rendering them well-suited for largescale manufacturing. Various forms of third-generation solar cells, such as organic photovoltaics (OPVs), dye-sensitized solar cells (DSSCs), and quantum dot solar cells (QDSCs), have encountered challenges in their manufacturing methods or have exhibited relatively poor power conversion efficiencies $(PCEs)$, hence impeding their widespread commercial utilisation. Therefore, it can be inferred that perovskite solar cells (PSCs) have the potential to emerge as a promising contender for the advancement of 4th generation solar cell technologies, primarily

due to its favourable characteristics in terms of cost-effectiveness throughout the manufacturing process and high device efficiency [101].

Another significant factor driving the ongoing efforts of numerous researchers is the economic viability associated with efficient and stable perovskite solar cells. Chang et al. conducted a comprehensive evaluation, wherein they estimated the production costs and levelized cost of energy (LCOE) to fall within the range of $87 to 140$ per square meter and 3.5 to 4.9 cents per kilowatt per hour, respectively [20]. Although it is possible to produce FPSCs using a roll-to-roll manufacturing process, there is clearly potential to reduce the levelized cost of electricity (LCOE) [101].

Perovskite photovoltaic (PV) technology has demonstrated the potential to achieve cost competitiveness with crystalline silicon $(c-Si)$ PVs $\$0.02/\text{kWh}$ and thin-film cadmium telluride (CdTe) modules $\$0.04/\text{kWh}$. However, the economic viability of perovskite PVs is currently underestimated. This is due to factors such as the selection of module production methods, which often involve the use of expensive materials like silver (Ag) or gold (Au), as well as slow throughput deposition techniques like thermal evaporation. Song et al (2017) presented a study that showcased a very favourable photovoltaic solar cell (PSC) architecture and an efficient production procedure, resulting in a significant reduction in manufacturing expenses, with costs as low as 6.3 cents per kilowatt-hour [101, 102].

In summary, perovskite solar exhibit numerous advantages in comparison to alternative solar cells, including their cost-effectiveness, superior efficiency, and capacity for customization.Nevertheless, there are certain obstructions that must be encountered prior to achieving widespread commercialization of these technologies. These challenges encompass issues related to stability,toxicity, and scalability.

II.6 Fabrication of Perovskite Solar Cells

In the device architectures utilised thus far for perovskite solar cells, the absorber layer, which is based on perovskite material, is positioned between the hole and electron transport layers. It is worth noting that the development and treatment of these transport layers can also have an influence on the performance of the perovskite absorber. In order to attain favourable physical properties, it is imperative to employ suitable fabrication procedures for the production of perovskite thin film absorber layers. The optoelectronic characteristics of perovskite thin films are influenced by various factors such as morphology, crystallinity, stoichiometry, and so on. These factors can be modified through different approaches, strategies, doping, pre- and post-treatments, environmental conditions, solvents, and molar compositions.

Perovskite devices commonly utilise physical and chemical processes, such as the vapour deposition method and one- and two-step solution-based procedures, which will be discussed in detail in this context. The methods can be categorised as vapour, solution, hybrid, and diffusion. In the vapour process, the absorber layer is formed through the evaporation method, either co-

evaporation or sequential evaporation. In the solution process, the absorber layer is entirely fabricated using spin coating (one step) or dip coating (two step). The hybrid process involves deposition using both solution and vapour methods. In the diffusion process, the absorber layer is partially formed through either the vapour or solution process, and then the samples are placed in a graphite block at an elevated temperature containing the compound to be diffused [17].

II.6.1 Vapor deposition method

The utilisation of the vacuum deposition technique was also employed in the production of perovskite thin films. The process of depositing perovskite films using vacuum deposition involves either the simultaneous evaporation of lead halide and organic halide salt or the sequential evaporation of lead halide followed by organic halide salt, as depicted in Figure II.10 (c). One notable benefit of employing this approach in contrast to solution processing is its ability to consistently produce perovskite films with a uniform, dense, and compact morphology. This is particularly advantageous as solution processing techniques often exhibit lower levels of reproducibility. One significant drawback of vacuum deposition in comparison to solution processing is the increased expense of manufacturing, mostly attributed to the necessity of maintaining a vacuum environment [92].

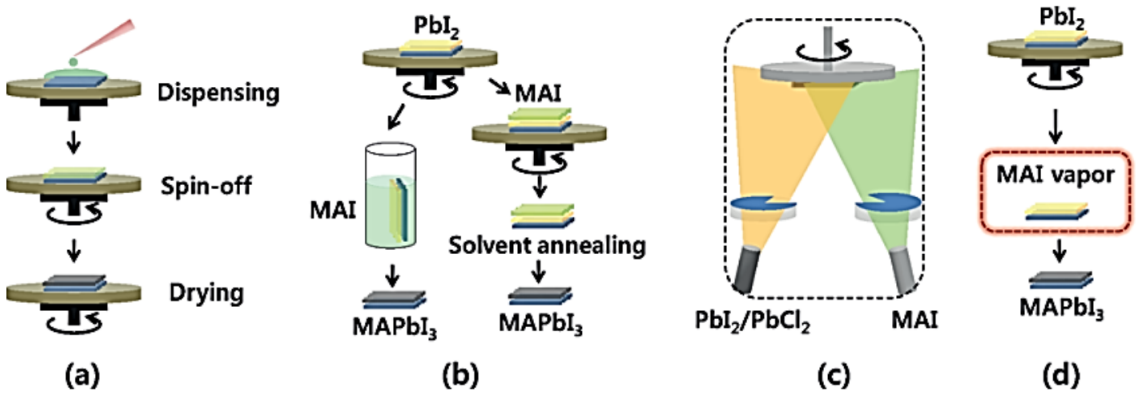

Figure II.10: Illustration depicting different techniques for depositing photoactive hybrid perovskite films; (a) one-step spincoating method; (b) two step or sequential deposition method; (c) dual-source vapor deposition; and (d) vapor-assisted solution process [103].

II.6.2 One-step and two-step solution-based methods

II.6.2.1 One-step solution-based method

The one-step solution procedure is widely employed as the predominant technique for the production of perovskite layers. In a brief manner, the precursor salts are initially dissolved in

a solvent that serves as a common among them. Subsequently, the resulting solution of precursors is deposited onto a substrate, and a spin-coating technique is employed to eliminate a portion of the solvent while the substrate undergoes spinning motion (Figure II.10 (a)). After the remaining solvent is eliminated during the subsequent post-annealing process, a thin film of perovskite is established [92]. The one-step approach has demonstrated a power conversion efficiency above 20% [103].

II.6.2.2 Two-step solution-based method

In the context of the "two-step" deposition procedure or "sequential" deposition process, two precursor solutions are produced [103]. This includes the first deposition of a lead halide layer,such as lead iodide (PbI_2), onto a glass substrate using spin-coating. This is then followed by the subsequent deposition of an organic halide salt, such as methylammonium iodide (MAI) or formamidinium iodide FAI, which reacts with the PbI_2 layer to produce a perovskite layer. The process of depositing organic halide salt can be accomplished by three methods: immersing the substrate coated with PbI_2 into a solution of MAI, applying the MAI solution (often dissolved in isopropanol) onto the PbI_2 layer using spin-coating, or through MAI vapour deposition. This is illustrated in (Figure II.10) (b) [92].

II.6.3 Hybrid process

A novel hybrid methodology including the combined utilisation of solution processing and vapour deposition techniques was also devised for the production of perovskite thin films. In this experimental procedure, the PbI_2 precursor is first deposited using spin-coating. Subsequently, the methyl ammonium iodide (MAI) compound is evaporated onto the PbI_2 film that has been previously formed. It is noteworthy that a power conversion efficiency (PCE) of approximately 12% was attained by employing this particular approach [103].

II.7 Potential Applications of PSCs

Perovskite solar cell products can be categorised into two different types: rigid perovskite solar cells and flexible perovskite solar cells. These cells are widely used in several sectors including homeowners, businesses, factories, automotive, defence, and other areas because to their adaptability and lightweight. The final users of perovskite solar cells vary across various sectors including aerospace, industrial automation, consumer electronics, energy, and other industries. The perovskite solar cells market comprises various products such as solar energy systems, smart glass windows, perovskite in tandem solar cells, utilities, mobile phones, building-integrated photovoltaics (BIPV), and other associated products [104].

II.8 Previous research on perovskite solar cells

Based on the literature study, the quantity of research articles on silicon-based solar cells has reached a point of saturation. There is a lack of study attention towards silicon because of its low bandgap $(1.12eV)$ and low absorption coefficient. The steady increase in the quantity of articles published on PSCs suggests that significant attention has been given to PSCs in the past ten years, as depicted in Figure II.11 (a). The increasing fascination with PSCs in comparison to silicon solar cells can be ascribed to their adjustable bandgap, better power conversion efficiency (PCE), and significantly reduced production costs. Perovskite solar cells (PSCs) have shown significant progress in terms of efficiency improvement in recent years, as illustrated in Figure II.11 (b). This indicates that PSCs have a promising future for further development [90].

The efficiency of carbon nanotube (CNT)-based bifacial perovskite solar cells (C-PSCs) reached 27.1% in 2022. The carbon-based material is highly advantageous in the PSCs market because of its superior stability, resistance to ion migration, and waterproofing. The study showed that the CPSCs, when combined with a $CuInSe_2$ (CIS) bottom cell in a 4-terminal (4-T) tandem solar cell (TSC), efficiently utilised the reflected irradiation to improve the power conversion efficiency (PCE). TSCs often have numerous light absorbers with varying bandgaps, enabling them to capture light across a wider spectrum of wavelengths and hence achieve higher power conversion efficiency (PCE). TSCs offer a viable method for surpassing the Shockley-Queisser limit by reducing transparency to low-energy photons and converting excess high-energy photons into heat.The Shockley-Queisser limit is a criterion employed to evaluate novel photovoltaic systems. It defines the utmost attainable efficiency of solar energy conversion for a specific material [90].

In the past 5 years, significant advancements have been made in the development of metal halide perovskite-based tandem solar cells (TSCs). Several studies have been published on MHP/CIGS TSCs, MHP/Si TSCs, and other types of perovskites TSCs All-perovskite (AP-TSCs). The maximum efficiencies for the aforementioned types of TSCs are 24.2%, 32.5%, and 29.0%, respectively. The AP-TSC, or All-Perovskite Tandem Solar Cell, stands out as a highly favourable option compared to other types of TSCs due to its ability to produce both subcells using low temperature and cost-effective solution processing methods. This makes it compatible with massproduction techniques like roll-to-roll printing. This enables the production of TSCs on pliable and lightweight substrates. Therefore, numerous studies have been conducted on the production of APTSCs, as well as the durability of WB-MHPs and NB-MHPs, with the aim of advancing the commercialisation of these very promising AP-TSCs. Nevertheless, the effectiveness and reliability of the AP-TSC fall short of meeting the demands of the business sector [105].

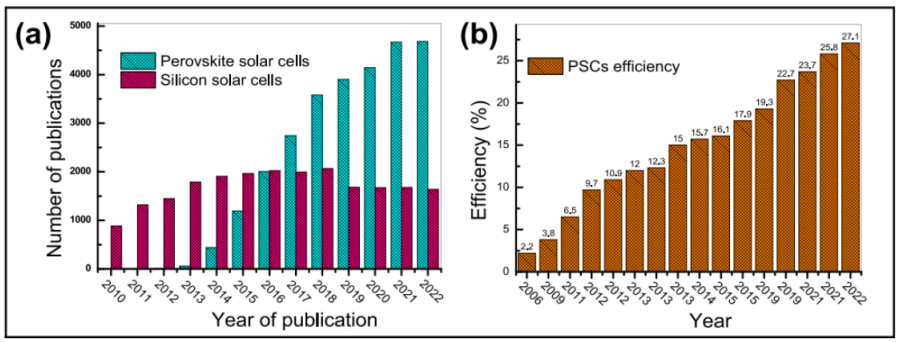

Figure II.11: Bar charts: a) showning to illustrate the number of articles on perovskite solar cells (PSCs) and silicon solar cells, b) the charts depict the progress in enhancing the efficiency of PSCs [90].

II.9 Challenges and opportunities in the implementation of perovskite solar cells

Despite the fact that the efficiency ratings of perovskite solar cells (PSCs) can rival those of commercially accessible photovoltaic panels, there are still several obstacles that need to be addressed in order to advance their commercialization, as outlined in Figure II.12. These challenges involve issues related to their long-term stability, potential lead toxicity, and the presence of J-V hysteresis [106]. The perovskite materials exhibit sensitivity to light, moisture, and high temperature due to their inherent softness and ionic nature. While certain measures, such as solid encapsulation, have been employed to mitigate moisture permeation, devices utilising perovskite materials continue to experience significant performance degradation during operation. This degradation can be attributed to inherent issues induced by light or heat, including lattice strains, phase transition, phase segregation, ion migration, and other related factors.

In addition, it is worth noting that high-efficiency perovskite solar cells (PSCs) are often produced on a small scale in laboratory settings, with an active area that is less than $1cm^2$. As the active area increases, the efficiencies of these PSCs decline due to the inadequate uniformity of the large-scale perovskite thin films and functional layers. Hence, a significant obstacle impeding the commercialization of perovskite solar cells (PSCs) lies in the deposition of high-quality large-area thin films that exhibit exceptional homogeneity. This problem is further compounded by the utilisation of large-area manufacturing processes. Furthermore, there has been a growing interest in conducting life cycle assessments on perovskite solar cells (PSCs) to evaluate their environmental impact. These assessments focus on factors such as the toxicity of organic solvents and the presence of heavy metals like lead (Pb) throughout the various stages of PSC fabrication, operation, and end-of-life disposal. The outcomes of these assessments are crucial in determining the viability of PSCs in the future market and stimulating the development of innovative techniques for manufacturing PSCs in a sustainable and environmentally conscious manner [107].

Figure II.12: Bar charts: a) showning to illustrate the number of articles on perovskite solar cells (PSCs) and silicon solar cells, b) the charts depict the progress in enhancing the efficiency of PSCs [90].

II.9.1 Long-term stability

The durability of perovskite solar cells is a significant impediment to their overall performance. The deterioration of absorber perovskite material and its subsequent decline in performance may be attributed primarily to three factors: moisture, temperature, and UV irradiation. To enhance the performance of *PCE* (power conversion efficiency), researchers utilised several strategies including ion doping, modification of HTL/ETL (hole transport layer/electron transport layer),adjustment of interfaces, and implementation of improved synthesis processes. In addition to photovoltaic conversion efficiency (PCE), the deterioration of materials is a notable limitation for the widespread manufacturing and commercial utilisation of perovskite-based solar cells. This section will systematically discuss each factor that contributed to the degradation of the material [106].

II.9.1.1 Progress in humidity stability

One major obstacle in the usage of PSCs in humid environments is the degradation of the perovskite material, namely the organic component of $MAPbI_3$. This material readily absorbs water molecules, leading to the decomposition of the perovskite into CH_3NH_2, PbI_2, and HI molecules, as seen in Figure II.13. Nevertheless, the perovskite film does not consistently suffer decomposition by water molecules. Wu et al. discovered that by introducing H_2O molecules during the preparation of the perovskite film, they were able to get a higher power conversion efficiency (PCE) of over 20%. This enhancement was attributed to the extended carrier lifespan and enhanced crystallization of the film. However, in the presence of high ambient humidity,

the perovskite film will experience significant degradation. The subsequent reaction process explained the mechanism of perovskite decomposition [83]:

$$CH_3NH_3PbI_3 + H_2O \longleftrightarrow CH_3NH_3PbI_3 \bullet H_2O \tag{II.9}$$

$$4\,(CH_3NH_3PbI_3 \bullet H_2O) \longleftrightarrow (CH_3NH_3PbI_3)_4(PbI_6) \bullet H_2O + 3\,PbI_2 + 2\,H_2O \tag{II.10}$$

$$(CH_3NH_3PbI_3)_4PbI_6 \bullet {}_2\,H_2O \longleftrightarrow {}_4\,CH_3NH_3PbI_3 + PbI_2 + 2\,H_2O \tag{II.11}$$

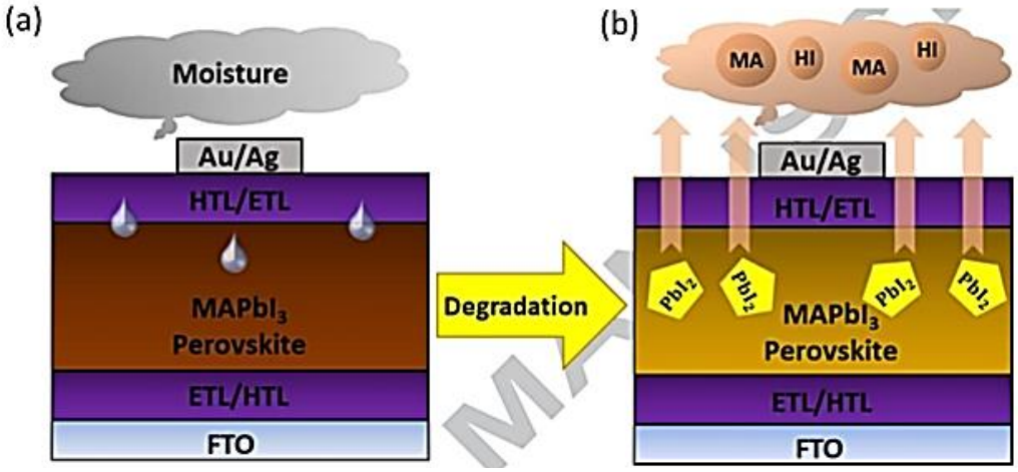

Figure II.13: Deterioration of PSCs structure prior to (a) and subsequent to (b) exposure to a humid environment [83].

During the early stage of the process, when perovskite materials come into contact with moisture, the $CH_3NH_3PbI_3 \bullet H_2O$ phase of monohydrate is produced by hydrogen bonding (as shown by formula II.9). During this phase, the connection between $CH_3NH_3{}^-$ and I^- ions weakens, while the combination bond between $CH_3NH_3{}^-$ and H_2O molecules strengthens. Nevertheless, it is a process that may be reversed. The water molecules adsorbed on the surface of the perovskite layer can be eliminated using processes such as heating, vacuuming, or nitrogen drying [83].

As the quantity of H_2O molecules adsorbed onto the perovskite layer's surface rises, the perovskite material encounters additional reaction with water to produce a dihydrate material ($(CH_3NH_3)_4\,PbI_6 \bullet {}_2\,H_2O$) and starting decomposition into bI_2, as represented by formula II.10. This reaction process is also a procedure that may occur in both directions. The deteriorate process of perovskite materials can be inhibited by managing the external environment and

limiting the concentration of water molecules associated with the perovskite material. Nevertheless, when the perovskite materials endure further interaction with water molecules, the water molecules persist in dismantling the crystal structure of the perovskite, resulting in the slow decomposition of the perovskite materials into CH_3NH_3I, PbI_2, and H_2O, as seen in formula II.11. During the aforementioned process, water molecules in the air gradually degrade the perovskite film, resulting in the weakening of both the film and the device under humid conditions. This limits the use of perovskite devices in humid external environments [83].

II.9.1.2 Oxygen

Aristidou et al. conducted a study that integrated experimental investigation and theoretical modeling to examine the influence of oxygen on perovskite thin film. It was discovered that when the perovskite layer is exposed to oxygen, O_2 molecules would spread across the perovskite material lattice and selectively bind to the iodine vacancy defects inside the perovskite materials, as seen in Figure II.14. During exposure to sunlight, the perovskite film's photo-generated electrons can be captured by O_2 molecules. These electrons are then transferred to $O_2{}^-$ ions, which then combine with photo-oxidized $CH_3NH_3PbI_3$. This reaction leads to the formation of PbI_2, I_2, H_2O, and CH_3NH_2, culminating in the deterioration of the perovskite materials. The reaction can be described as follows [83]:

$$4\,CH_3NH_3PbI_3 + O_2{}^- \rightarrow {}_4PbI_2 + 2\,I_2 + 2\,H_2O + 4\,CH_3NH_2\,(g) \tag{II.12}$$

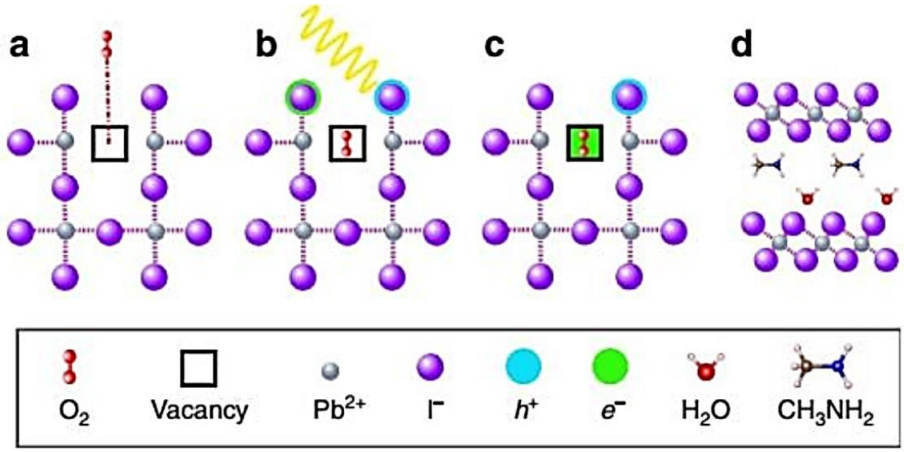

Figure II.14: Oxygen-induced photo-degradation. Schematic representation of the reaction steps of O_2 with $CH_3NH_3PbI_3$. (a) Oxygen diffusion and incorporation into the lattice, (b) photoexcitation of $CH_3NH_3PbI_3$ to create electrons and holes (c) superpxide formation from O_2, and (d) reaction and degradation to layered PbI_2, H_2O, I_2 and CH_3NH_2 [83].

II.9.1.3 Thermal Stability

To address the stability issues of perovskite devices caused by external variables, such as H_2O and O_2, it is feasible to mitigate this problem by employing appropriate device packaging techniques that effectively isolate these elements. The temperature has a notable influence on the structure of the crystals and transition from one phase to another of organic-inorganic mixed perovskite materials. At elevated temperatures, perovskite materials experience thermal deterioration. At a temperature range of 54-56 °C, the $MAPbI_3$ perovskite materials undergo a phase transition from a tetragonal phase (non-perovskite phase) to a cubic phase (perovskite phase). As per the international solar cell test standard, solar cell modules need to undergo a thermal stability test by being subjected to a high-temperature environment of 85 °C. According to McGehee et al., the perovskite materials exhibited a tendency to breakdown into PbI_2 when subjected to heating at a temperature of 85 °Cfor a duration of 24 hours in an environment containing nitrogen. To mitigate the negative effects of high temperatures, opting for heat-resistant materials would be a suitable decision. The FA^+ cation has been employed as a partial or complete substitute for the MA^+ cation in PSCs, resulting in significantly enhanced thermal stability of the PSCs. Currently, several researchers have discovered that two-dimensional perovskite materials may also be utilized to improve the thermal stability of perovskite devices [83].

II.9.1.4 UV-irradiance effect

Because of their nature as organic solar cells and dye-sensitized solar cells, PSCs are susceptible to deterioration by ultraviolet light, which in turn reduces their photovoltaic efficacy. There is around 5% ultraviolet radiation when exposed to normal sunshine (AM 1.5 G). TiO_2 materials are commonly employed as an electron transport layer in PSCs. The titanium dioxide materials possess pho-tocatalytic characteristics, allowing the TiO_2 layer to absorb UV light and subsequently produce electron-hole pairs, as seen in Figure II.15. The presence of photogenerated holes leads to strong oxidation, causing the perovskite materials to decompose into I_2, CH_3NH_2, and HI. Furthermore, it will induce changes in the local electric field and prompt the movement of iodine ions within the perovskite. The chemical process that occurs under the influence of light can be described as follows [83].

$$2I^- \longleftrightarrow I_2 \tag{II.13}$$

$$3\,CH_3NH_3{}^+ \longleftrightarrow {}_3CH_3NH\,(g) + 2\,H^+ \tag{II.14}$$

$$I^- + I_2 + 3H^+ + 2e^- \longleftrightarrow {}_3HI(g) \tag{II.15}$$

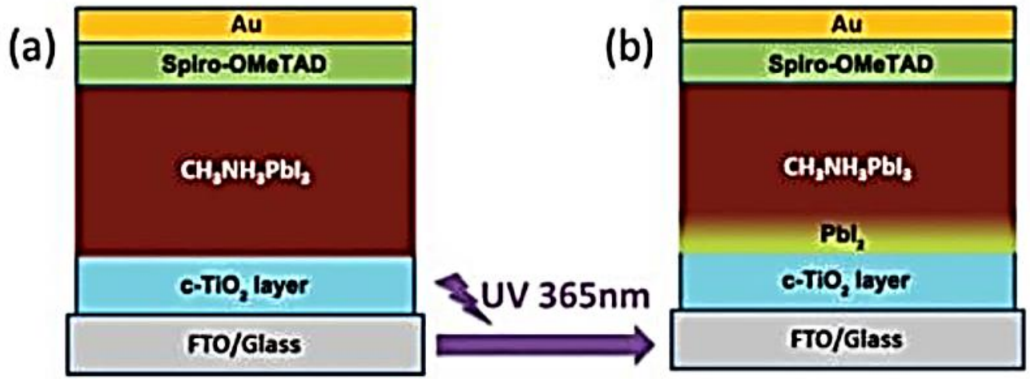

Figure II.15: Control perovskite solar cell (a) before and (b) after UV radiation, shown as a schematic [83].

II.9.1.5 J-V hysteresis

An example of a challenging phenomenon for researchers is the hysteresis in the current densityvoltage (J-V) curve, which was initially identified by Henry Snaith in 201. The J–V curve is the primary method used to determine the energy conversion efficiency of PS. The device J–V curve is typically measured under standard AM1.5 $(100mW/cm^2)$ illumination. Currently, the opencircuit voltage (V_{OC}), short-circuit current (J_{SC}), fill factor (FF), and conversion efficiency η of solar systems are determined by analyzing the J-V curve. During the J–V measurement of the PSC, a hysteresis always exists between the forward scan (voltage biased from $0V$ toV_{OC}) and revers scan (voltage biased from V_{OC} to $0V$) scan , meaning that the forward and reverse scan cannot coincide as shown in Figure II.16.

The majority of observations on the J–V hysteresis in PSC indicate a typical hysteresis, demonstrating superior performance during reverse scanning (RS) compared to forward scanning (FS). Nevertheless, there have been instances where the reverse hysteresis occurs, leading to a decrease in performance of the RS compared to the FS. The presence of this hysteresis is contingent upon the direction and/or speed of the scanning process, resulting in either an overestimation or underestimating of the actual conversion efficiency of the PSC. Hysteresis is considered a contributing reason to the inconsistent power output in PSC [108].

It is indisputable that the photovoltaic parameters should not be influenced by factors such as prelighting, starting voltage, scanning rate, direction, and residence time of each test bias prior to JV testing. The presence of hysteresis problems raises concerns about the reliability of the findings acquired from the photovoltaic performance, making it difficult to accurately evaluate the actual performance of PSC. Consequently, the J–V hysteresis effect is a significant

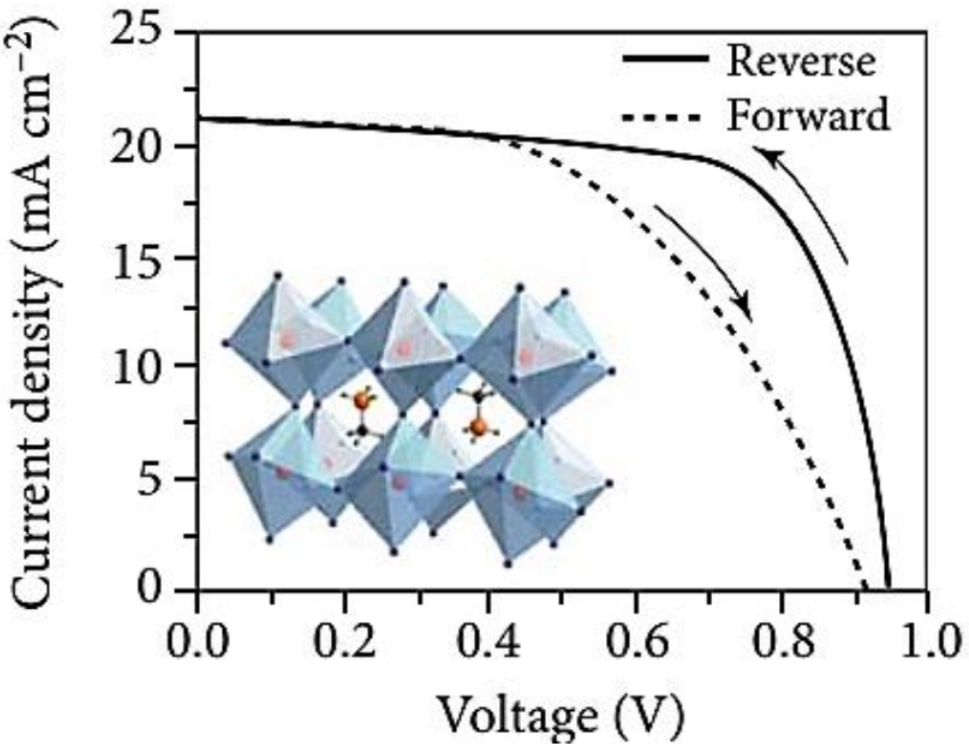

Figure II.16: Normal J-V curve in both FS and RS when the sun is shining. The voltage scanning lines are shown by the arrows. The 3D perovskite crystal structure is shown in the picture below [109].

obstacle that limits the progress of PSC. Despite numerous attempts to comprehend the source of hysteresis and mitigate its effects, the hysteresis phenomenon in PSC remains a subject of vigorous discussion, and a universally successful approach has not yet been devised [109]. To comprehensively comprehend the underlying reasons of the hysteresis effect in PSCs, numerous potential explanations have been put out and thoroughly examined. These include the capacitance effect,ferroelectricity, ion migration, and charge trapping, among others [83].

Capacitance Effect

The photocurrent observed in perovskite solar cells may be separated into two components: a constant photocurrent known as steady-state photocurrent (J_0), and a time-dependent photocurrent referred to as non-steady-state photocurrent $(J_n(t))$. Hysteresis in the current-voltage characteristics is caused by a gradual decay process that affects the non-steady-state photocurrent during voltage sweep measurements. The degradation is a consequence of the photo-induced phenomenon of enormous dielectric permittivity, which leads to an increase in capacitance within the cells [110].

Impedance spectroscopy tests validate the existence of a low-frequency arc, which signifies electrode polarization resulting from the accumulation of charges at the interface of the perovskite film. Under illumination, the dielectric permit-tivity experiences a substantial increase,

resulting in a big rise in low-frequency capacitance and a gradual decrease in the capacitive current. Further work is needed to understand the influence of the loss tangent on the relationships between capacitance and frequency, as well as dielectric permittivity and frequency [110].

Ferroelectricity

The ferroelectric effect potentially influences the hysteresis observed in perovskite solar cells. Presence of ferroelectric domains in the $MAPbI_3$ thin films allows for manipulation of the interface band structure, resulting in distinct polarization properties. This manipulation leads to differing photovoltaic (PV) performance during forward and reverse scanning. Negative polarization impedes the process of charge separation, whereas positive polarization enhances it [110].

During the forward scan, the initial polarization electric field counteracts the built-in electric field, inhibiting charge extraction. In contrast, during the reverse scan, the initial polarization electric field amplifies the inherent electric field. The presence of ferroelectric polarization domains in films made of organometal perovskite has been examined using theoretical modeling, revealing the impact of polar molecules on the performance of photovoltaic cells [110].

Ion Migration

Ion migration is a potential factor contributing to the J-V hysteresis phenomenon. When an external electric field is applied to the perovskite device, the positive and negative ions that have gathered near the electrodes will either speed up or hinder the movement of ions towards the respective sides of the device, resulting in the formation of areas with limited ion movement at the electrode interfaces. Furthermore, the distortion of the energy band resulting from ion migration has an impact on the movement and accumulation of electrons and holes, hence influencing the photovoltaic efficiency of the PSCs [83].

Ion migration has been observed in polarization-switchable perovskite devices, where the direction of photocurrent can be altered by modifying the voltage scanning direction. The application of an external electric field causes the slow movement of ions, resulting in the occurrence of the J-V hysteresis phenomenon. Hence, reducing the density of mobile ions or carrier charge defects within the perovskite light absorber layer and at the interfaces can mitigate the hysteresis effect [83].

Defect State Theory

Furthermore, with the aforementioned potential hysteresis factors, the defect state hypothesis is currently seen as another significant contributor to device hysteresis. Currently, perovskite materials are primarily synthesized using the solution process approach. However, this procedure results in the formation of numerous defects in the thin film. These imperfections have the ability to trap charge carriers, which ultimately leads to the observed hysteresis phenomenon.

Huang's group discovered that by introducing fullerene to a perovskite film, the surface and interface defect states of the film were successfully neutralized, resulting in the successful suppression of the perovskite hysteresis phenomena [83].

Chapter III

Numerical Simulation by Silvaco-Atlas

Chapter III

Numerical Simulation by Silvaco-Atlas

III.1 Introduction

Numerical modelling, also referred to as numerical analysis, includes computer software that controls mathematical models to simulate and depict the behavior of various physical systems. It serves as a technique for examining systems governed by complex mathematical models, facilitating the acquisition of analytical solutions. This tool is indispensable for delving deeper into the operational workings of any given device.

In the field of solar device production and semiconductor-based construction, numerical analysis holds principal importance. Design engineers and researchers strive to harness numerical modelling methodologies to impeccably integrate real-world complexities into a virtual environment. Through this, they aim to pinpoint the most efficient strategies for addressing intricate challenges. Educational institutions highlight computer-centric learning methods as they enable the thorough exploration of practical design hurdles, sans the necessity for physical implementation, thus conserving invaluable time.

Modelling approaches are instrumental in calculating essential physical parameters, such as electron and hole concentrations, along with electrical potential. Moreover, they provide valuable insights into how material properties affects the functional attributes of devices. To execute simulation programs effectively for solar cell numerical modelling, inputting the material's physical properties is imperative.

It is essential to utilize experimental data in order to depict the true or authentic device's $J-V$ characteristics and operational parameters, including power conversion efficiency, fill factor, open circuit voltage, and short circuit current. To better understand the device's behavior, numerical simulation provides a more efficient and user-friendly alternative. The ability to solve the Poisson equation, which establishes the relationship between charge and electrostatic potential, and the continuity equations for holes and electrons are fundamental semiconductor equations that must be effectively handled by the simulation software used for device modeling in order to conduct a thorough evaluation of the device's performance [111].

Several software tools, such as SCAPS, Silvaco, COMSOL, AMPS, and wxAMPS, can be used to evaluate the performance of single or multijunction solar cells. In this study, the optical and electrical characteristics of the suggested solar cell are modelled and simulated using the Silvaco- TCAD simulator. The solution of the semiconductor carriers' equations is discretized using a predetermined grid in the numerical simulation [112].

This chapter offers a detailed exploration and explanation of SILVACO-ATLAS simulation software. Throughout this chapter, we delve into the significance and diverse applications of SILVACO-ATLAS simulation. We examine its crucial role in accurately modeling and analyzing a range of electronic devices, including MOSFETs, bipolar transistors, diodes, and solar cells. Furthermore, we explore how SILVACO-ATLAS facilitates understanding device physics, optimizing performance, and navigating design trade-offs.

III.2 SILVACO-ATLAS Simulation Tool

III.2.1 Overview and Features

SILVACO TCAD software is an acronym for Silicon Valley Corporation Technology ComputerAided Design. The simulation package process for semiconductor devices includes a collection of physically based simulators (such as ATHENA, ATLAS, MERCURY, SSUPREM3, etc.) that are organized into a single environment known as DECK BUILD. Each of them is responsible for modeling distinct processes. From of SILVACO's various modules, ATLAS is the most appropriate module for this research [113]. Which is a powerful simulation software that is utilised for the study of electronic, optical, and electro-optical devices. It can perform AC, DC, and transient analysis in both 2D and 3D. The software employs diverse physical models coupled with robust numerical algorithms to simulate the functioning of device systems [114].

There are three separate types of output files that ATLAS produces. The run-time output is the first type of output file; it updates the user on the simulation's progress and displays any warnings or errors that occurred. The log file documents all currents and voltages measured at the device's terminals and is the second type of output file. An additional type of output file is the solution file. This file includes both two-dimensional and three-dimensional information about the values of the device's solution variables at a certain bias point [113].

SILVACO offers a range of additional software tools that can be used alongside these programs to facilitate simulations. The included software packages are TonyPlot, TonyPlot3D, DeckBuild, MaskViews, and DevEdit. We will only provide an explanation for the packages utilized in this investigation [115].

- **DeckBuild:** Interactive Deck Development and Runtime Environment DeckBuild is a dynamic platform where SILVACO TCAD products can be executed, allowing for the creation and modification of input files. DeckBuild offers a wide range of pre-designed

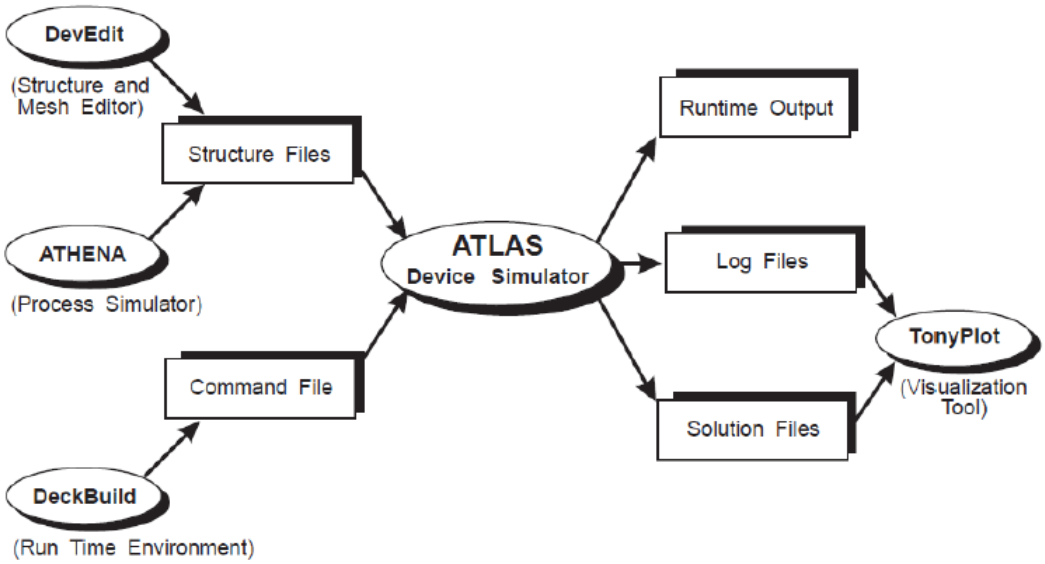

Figure III.1: Atlas inputs and outputs [113].

decks that showcase various technologies and materials. These decks enable users to quickly gain knowledge in simulation [115].

- **TONYPLOT:** TONYPLOT is an effective tool specifically created to display TCAD 2D and 3D structures generated by SILVACO TCAD simulators. TONYPLOT offers advanced visualization capabilities, including features like as panning, zooming, different viewpoints, labeling, and support for numerous plots. TONYPLOT offers a variety of visualization functions that are special to TCAD. These include 1D cut lines from 2D structures, animated markers to display vector flow, integration of log or 1D data files, and the ability to fully customize TCAD-specific colors and styles [115].

III.2.2 Device Simulation Capabilities

Atlas is an accurate simulation software that provides an extensive array of features and capabilities for modeling and analyzing devices. The software encompasses a variety of physical models for conducting simulations in the domains of direct current (DC), alternating current (AC), and time-dependent phenomena. Additionally, it incorporates models for transport, energy balance, hydrodynamic transport, and optoelectronic interactions. Additionally, it is compatible with a wide range of material types, heterojunctions, circuit settings, and trap dynamics. Atlas interfaces smoothly with other tools from Silvaco and enables for complex numerical implementation, including adaptive mesh refinement, parallel computation, advanced convergence control, and multi-physics coupling. Additionally, it offers comprehensive visualization and data analysis capabilities, rendering it a flexible instrument for precise and efficient device simulations [51].

III.2.3 Device Physics and Models

The mathematical model employed in the Atlas simulator establishes a connection between the electrostatic potential and the densities of carriers within a semiconductor device. This model incorporates essential equations, such as Poisson's equation, which establishes a connection between potential and charge density, as well as carrier continuity equations, which elucidate the changes in electron and hole concentrations over time. The discretization process is used to apply the equations derived from Maxwell's laws to the finite element grid that stands in for the device in the simulation. This approach allows for accurate predictions of how well devices will function [51].

III.2.3.1 Poisson's Equation

The electrostatic potential and the space charge density are related according to Poisson's Equation:

$$\operatorname{div}(\varepsilon \nabla \Psi) = -\rho \tag{III.1}$$

Electrostatic potential, local permittivity, and local space charge density are denoted by Ψ, ε, and ρ, respectively. Various methods can be used to define the reference potential. The intrinsic Fermi potential Ψ_i is consistently referred to by Atlas. Electrons, holes, and ionized impurities all contribute to the total local space charge density, which includes both mobile and stationary charges.

The electric field is calculated from the potential gradient:

$$\vec{E} = -\nabla \Psi \tag{III.2}$$

III.2.3.2 Carrier Continuity Equations

What follows are the equations that characterize the continuity equations of electrons and holes:

$$\frac{\partial n}{\partial t} = \frac{1}{q} \operatorname{div} \vec{J}_n + G_n - R_n \tag{III.3}$$

$$\frac{\partial p}{\partial t} = -\frac{1}{q} \operatorname{div} \vec{J}_p + G_p - R_p \tag{III.4}$$

With respect to the concentration of electrons and holes, respectively, we have G_n and G_p, which stand for the rates of generation of these two variables. Here, R_n and R_p stand for the electron and hole recombination rates, respectively. An electron's charge is represented by the variables q [51].

III.2.3.3 The Transport Equations

Equations specify charge transport, generation, and recombination physical models in device simulation. Simplifying the Boltzmann Transport Equation yields these equations. Choice of charge transport model affects generation and recombination models. Smaller devices need more complicated models than the Drift-Diffusion Model, which is the most prevalent. Atlas has driftdiffusion and sophisticated transport models [51].

A drift-diffusion model can be used to estimate the current densities in the continuity equations, according to derivations based on the Boltzmann transport theory. The quasi-Fermi levels, written as Ψ_n and Ψ_p, stand for the current densities in this situation [51]:

$$\vec{J_n} = qn\mu_n\vec{E_n} + qD_n\nabla n \tag{III.5}$$

$$\vec{J_p} = qp\mu_p\vec{E_p} - qD_p\nabla p \tag{III.6}$$

$$\vec{E} = -\vec{grad}\Psi \tag{III.7}$$

$\mu_n$and μ_p denote the mobilities of electrons and holes, respectively. The electron and hole diffusion coefficients, denoted as D_n and D_p, respectively, can be determined using Einstein's relationship:

$$D_n = \frac{K_B T}{q}\mu_n \tag{III.8}$$

$$D_p = \frac{K_B T}{q}\mu_p \tag{III.9}$$

III.3 ATLAS Simulation Workflow

The Atlas syntax is employed for generating command files for the Atlas simulation software. The command files are stored as ASCII text files and can be created using either DeckBuild or a text editor. Every command has a keyword and a collection of parameters. The syntax is mostly caseinsensitive, with the exception of certain commands issued by DeckBuild. Parameters can possess several types, including Real, Integer, Character, and Logical. A sample command line consists of the term "DOPING" along with parameters like "CONCENTRATION", "REGION", and "OUTFILE". The order of the parameters is irrelevant, and abbreviated versions of the parameter names can be utilized as long as they are distinct. Logical parameters can be assigned a value of either true or false [51].

III.3.1 Device and Process Simulation Setup

The sequence of statements in an Atlas input file is of utmost importance and must be adhered to accurately in order to prevent errors and guarantee the right functioning of the program. There are five distinct categories of statements that need to be organized in the correct sequence, as depicted in Figure III.2. Incorrect arrangement of these groups may result in the display of an error notice, which can lead to inaccurate calculations or the termination of the application. Statement order in structural definition, mesh definition, and solution groups is also crucial. Any divergence from the accurate sequence within these categories can lead to erroneous functioning or program termination [51].

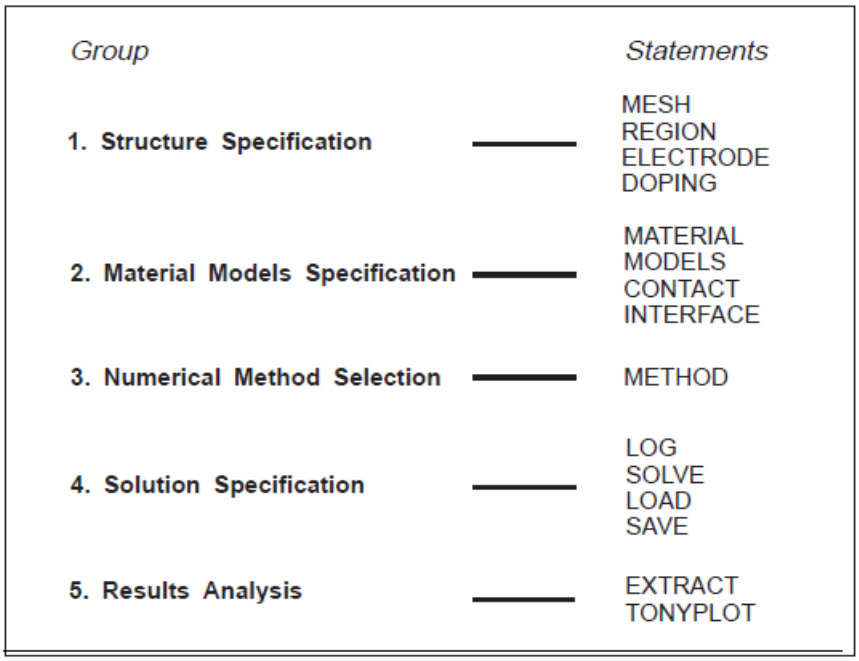

Figure III.2: Atlas Command Groups, each with its own main statement [113].

III.3.1.1 Structure Specification

The structure definition is accomplished through the identification of the mesh, the region, and the electrodes.

➢ **Defining the Mesh**

The first approach employed to accurately determine structural parameters is known as "MESH". To represent the device's mesh in this way, a grid made of a succession of horizontal and vertical lines is created. The automatic form and the standard form are the two main ways it can be classified. You can express the first form, which is standard meshing, as follows [79]:

```
Mesh space.mult=<value>
```

```
X.mesh location=<value> spacing=<value>
Y.mesh location=<value> spacing=<value>
```

The significance of SPACE.The MULT parameter is employed as a multiplier for the mesh, allowing for scaling. The significance of SPACE.The MULT parameter is used to scale the mesh generated by the X.MESH and Y.MESH statements. The default value for the beginning value is set to 1. Values greater than 1 will lead to a grid with reduced level of detail that is suitable for fast simulation. Values less than 1 will yield a finer mesh overall, resulting in improved accuracy. The X.MESH and Y.MESH statements are used to specify the positions in microns of vertical and horizontal lines, respectively, as well as the spacing between each line. Each direction must have a minimum of two mesh lines defined. Atlas employs an automatic mechanism to introduce extra lines as necessary in order to achieve seamless transitions in the spacing values between consecutive lines. The X.MESH and Y.MESH statements need to be organized in ascending order based on the values of x and y, respectively. Both positive and negative values of x and y are acceptable [113].

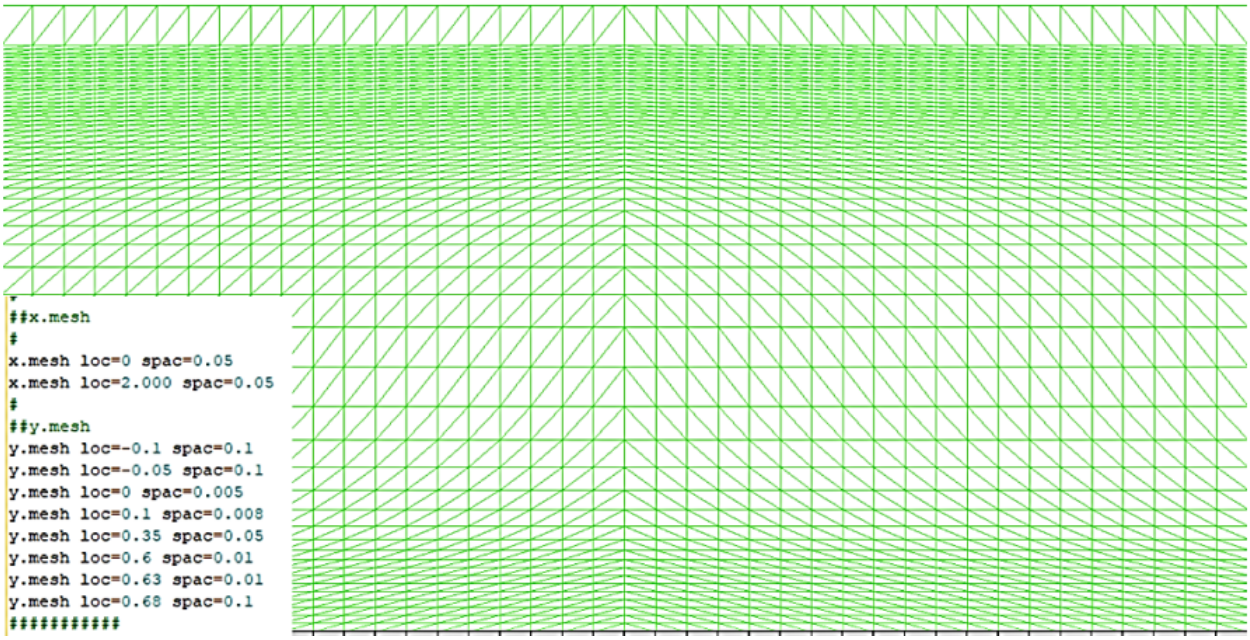

Figure III.3: Example of the mesh [113].

```
Mesh auto
X.mesh location=-1.0 spacing=0.1
X.mesh location=1.0 spacing=0.1
```

The SPACING parameter value determines the horizontal distance between vertical grid lines at the specified LOCATION point. The generation of meshing in the Y direction will be postponed at that point defined as the REGION statement. Auto meshing is commonly

employed in devices with a uniform X direction, such as solar cell devices. We employed the auto meshing approach in our study. Figure III.3 illustrates an example of the mesh utilized for the perovskite solar cell structure, as described in the accompanying deck in Figure III.3 [79]. An example of a mesh definition of the perovskite solar cell in this dissertation is given below.

```
##x.mesh
x.mesh loc=0 spac=0.05
x.mesh loc=2.000 spac=0.05
##y.mesh
y.mesh loc=-0.1 spac=0.1
y.mesh loc=-0.05 spac=0.1
y.mesh loc=0 spac=0.005
y.mesh loc=0.1 spac=0.008
y.mesh loc=0.35 spac=0.05
y.mesh loc=0.6 spac=0.01
y.mesh loc=0.63 spac=0.01
y.mesh loc=0.68 spac=0.1
```

The example illustrates a configuration of a two-dimensional mesh grid along the x and y axes, with given positions and spacings. Two homogeneous mesh sections are defined for the x-axis, with a separation of 0.05 units. The y-axis mesh is characterized by its intricate structure, consisting of several segments with spacings that range between 0.005 and 0.1 units. These different spacing are strategically designed to accommodate diverse mesh densities, allowing for the accurate representation of specific phenomena in different regions. This configuration implies a deliberate method for conducting simulation or analysis, with an emphasis on using a highresolution mesh in specific regions of interest to guarantee precise and comprehensive outcomes.

➢ **Specifying regions**

Assigning a material type to each part of the mesh is the next step after specifying it. REGION statements are used to accomplish this task. As an illustration:

```
REGION number=<integer> <material_type> <position parameters>
```

The region numbers must commence at 1 and are incremented for each succeeding region statement. Atlas allows for a maximum of 15000 distinct regions. Access to a wide variety of materials is possible. The REGION statement also allows for the specification of composition-dependent material types, which include the x and y composition fractions [51].

Utilizing the X.MIN, X.MAX, Y.MIN, AND Y.MAX parameters, the position parameters are defined in microns. When two or more REGION statements have position parameters that

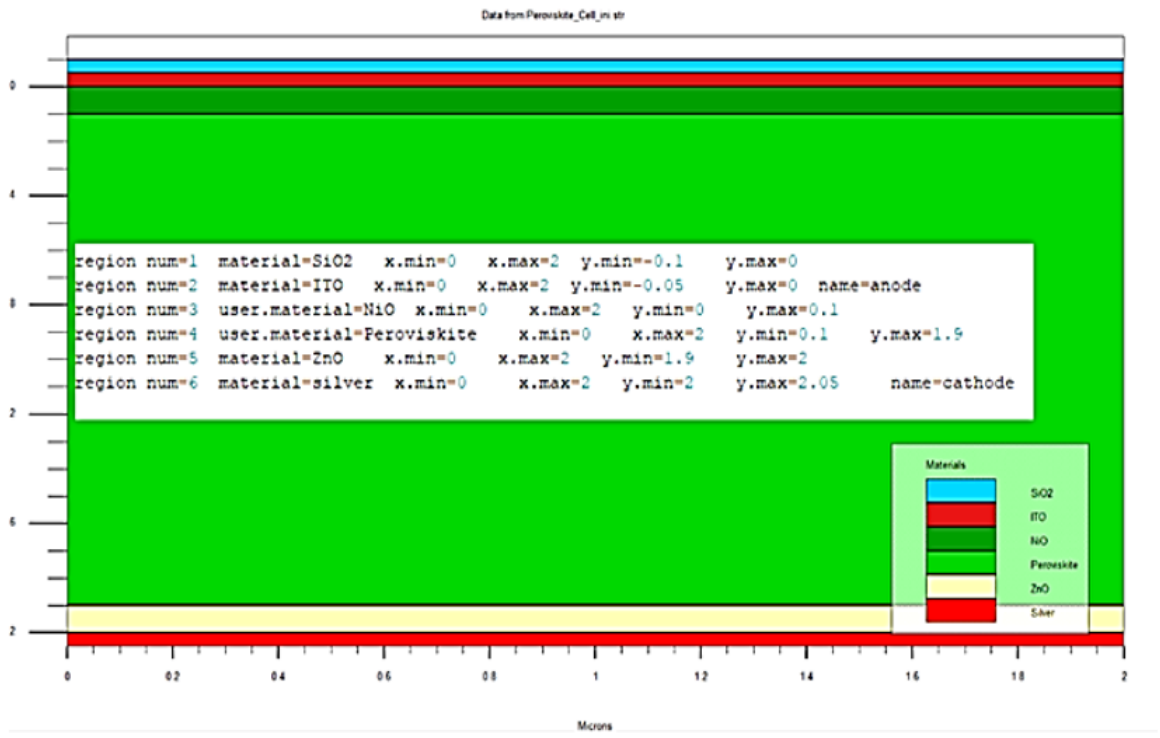

Figure III.4: A Tonyplot screenshot that shows an example of the regions.

overlap, the area where the two or more overlaps is used to determine the material type of the new region. To finish the construction, users must assign materials to every point on the mesh. Without executing this will cause Atlas to fail to launch and display error messages [51]. Below is an example of REGION created in atlas for the perovskite solar cell in the current study:

```
region num=1 material=SiO2 x.min=0 x.max=2 y.min=-0.1 y.max=0
region num=2 material=ITO x.min=0 x.max=2 y.min=-0.05 y.max=0 name=anode
region num=3 user.material=NiO x.min=0 x.max=2 y.min=0 y.max=0.1
region num=4 user.material=Cs2BiAgI6 x.min=0 x.max=2 y.min=0.1 y.max=0.6
region num=5 material=ZnO x.min=0 x.max=2 y.min=0.6 y.max=0.63
region num=6 material=silver x.min=0 x.max=2 y.min=0.63 y.max=0.68 name=cathode
```

The example illustrates an ordered structure within a model, comprising of six sections, each characterized by their material composition and spatial limits along the x and y axes. The zones are placed in a sequential manner, ranging from ‘y.min=-0.1‘ to ‘y.max=0.68‘. These regions consist of materials such as SiO_2, ITO, NiO, Cs_2BiAgI_6, ZnO, and silver. These materials serve different roles including insulation, conduction, light absorption, and charge transport. The ITO and silver layers are explicitly designated as the "anode" and "cathode," respectively, denoting their functions within the electrical framework of the device, most likely a thin-film solar cell or a comparable optoelectronic system.

➢ **Specifying electrodes**

After specifying the regions and materials, it is necessary to establish the definition of a minimum of one electrode that makes contact with a material for semiconductors. The ELECTRODE statement is utilized for this purpose. As an illustration [51]:

```
ELECTRODE NAME=<electrode name> <position_parameters>
```

There is a limit of 200 allowed electrode options. Specification of the positional parameters is given in micrometres using the x.min, x.max, y.min, and y.max parameters. The same electrode name could appear in many statements. Electrodes that are physically close to each other and have the same name are said to be electrically related. When describing the location of an electrode, specific acronyms can be used. Presumption of electrode placement at structure top is made in the absence of Y coordinate values. Furthermore, you may fine-tune the location by using the RIGHT, LEFT, TOP, and BOTTOM properties. For instance [51]:

```
ELECTRODE NAME=SOURCE LEFT LENGTH=0.5
```

The structure's source electrode starts at its upper left corner and stretches over a length to the right [51]. This is an illustration of electrodes definition that used in our code:

```
electrode name=anode material=ITO x.min=0 x.max=2 y.min=-0.05 y.max=0
electrode name=cathode material=silver x.min=0 x.max=2 y.min=0.63 y.max=0.68
```

The electrode statement presents crucial details regarding two specific electrodes: the anode and cathode. The anode consists of Indium Tin Oxide (ITO) and extends from x=0 to x=2, with a ycoordinate ranging from -0.05 to 0. Conversely, the cathode consists of silver and is positioned between x=0 and x=2, with its y-coordinate ranging from 0.63 to 0.68.

➢ **Specifying Doping**

The structure definition is incomplete without the doping assertion. To determine the doping level inside the allotted zones, the doping statement is utilised. To learn more about the semiconductor's doping, the region's n- or p-type status, and the uniformity or gaussianity of the doping, you can add more attributes to the doping statement. Here is the correct format for writing this statement [51]:

```
DOPING <distribution_type> <dopant_type> <position_parameters>
```

Instead of an area number, it may employ the position parameters X.MIN, X.MAX, Y.MIN, and Y.MAX. Here are two examples of doping statement:

```
Doping uniform concentration=1e16 n.type region=1
Doping gaussian concentration=1e18 characteristic=0.05 p.type X.left=0.0 x.right=1.0 p
```

Here is a specific example of a doping statement employed in our simulation:

```
Doping uniform region=3 p.type conc=1e17
Doping uniform region=4 p.type conc=1e15
Doping uniform region=5 n.type conc=5e18
```

The doping statement elucidates the procedure of introducing impurities into a material structure in order to modify its electrical properties. Region 3 (NiO) undergoes a process of p-type doping at a high concentration in order to enhance the conductivity of holes. On the other hand, Region 4 (Cs_2BiAgI_6) is weakly doped with p-type. On the other hand, Region 5 (ZnO) is extensively doped with n-type impurities in order to greatly improve electron conductivity.

III.3.1.2 Materials Model Specification

After setting up the mesh, geometry, and doping profiles, you can change the basic material parameters, change the electrodes' properties, and select which physical models Atlas will use for the device simulation. The CONTACT, MATERIAL, and MODELS statements are used to do these issues [51].

➢ **Specifying Material Properties**

The materials are categorized into three distinct classes: semiconductors, insulators, and conductors. Every class necessitates the specification of a distinct set of parameters. Regarding semiconductors, the parameters in question encompass electron affinity, band gap, density of states, and saturation velocities. Device simulation for various materials often includes default values for material properties [51]. You can specify your own settings for these basic characteristics in the MATERIAL declaration. A material or region may be relevant to your principles. Take the following sentence as an example [51]:

```
MATERIAL MATERIAL=ZnO permi=9 AFFINITY=4.1 eg300=3.3 nc300=4e18 nv300=1e19
mun0=30 mup0=10 index.file=ZnO.nk \TAUN0=1e-7 TAUP0=1e-7
```

The bandgap at 300K is denoted as EG300, whereas electron and hole mobilities are represented by MUN and MUP, respectively. The identification numbers for all the parameters can be located in the user handbook of Silvaco [51].

We can determine the index of refraction and the extinction coefficient for any material by employing either of the two approaches. One approach is to utilize refractive index information from the SOPRA database. In order to accomplish this, it is necessary to indicate the suitable index file (as stated in the user handbook) on the SOPRA parameter of the MATERIAL statement. Illustrated by the following example [113]:

```
MATERIAL MATERIAL=Platinum SOPRA =Pt.nk
```

An alternative approach involves inputting a text file that comprises sequential sets of wavelength, refractive index, and extinction coefficient triplets. This example illustrates the situation [113]:

```
MATERIAL MATERIAL=ZnO INDEX.FILE=ZnO.nk
```

➢ **Specifying Physical Models**

In order to specify physical models, the MODELS and IMPACT statements are used. Statements like "MOBILITY," "IMPACT," and "MATERIAL" list the parameters for these models. There are five main types of physical models: mobility, recombination, impact ionisation, tunnelling, and carrier statistics [51].

The MODELS statement specifies all models except for impact ionization. The IMPACT statement specifies the occurrence of impact ionization. As an illustration, consider the following statement [51]:

```
model MATERIAL=Cs2BiAgI6 srh conmob
```

In the example above we use Shockley-Read-hall (SRH) and concentration -dependent mobility model for Cs_2BiAgI_6 material.

- **The Shockley-Read-Hall (SRH)** model elucidates the process of recombination of charge carriers, namely electrons and holes, within a semiconductor material. This takes into consideration the presence of defects or impurities that have the potential to capture carriers and impact their lifespan.
- **The concentration-dependent mobility (conmob)** model recognizes that the mobility of charge carriers (electrons and holes) can change depending on their concentration, which in turn affects the electrical conductivity and overall performance of the material in semiconductor applications.

To summarize, the provided model statement pertains to the compound Cs_2BiAgI_6, takes into account the process of Shockley-Read-Hall (SRH) recombination, and employs the continuous mobility model to explain the behavior of carriers. These metrics are essential for comprehending the electrical characteristics of the material and its efficacy in devices.

➢ **Specifying contact characteristics**

It is assumed that an electrode is ohmic when it comes into contact with semiconductor material. The electrode is considered a Schottky contact once the work function is set up. You can specify the metal workfunction of an electrode or electrodes using the CONTACT statement. The NAME parameter is used to identify which electrode will have its attributes changed [51].

An electrode's workfunction value is defined by the WORKFUNCTION parameter. One example is the following assertion:

```
CONTACT NAME=gate WORKFUNCTION=4.8
```

Assigns a value of 4.8 electron volts to the work function of the electrode called "gate". The workfunctions of many frequently utilized contact materials can be determined by specifying the material's name [51].

```
contact name=anode workfun=5.2
contact name=cathode workfun=4.2
```

The contact statement specifies two contacts: the anode, which has a work function of $5.2eV$, and the cathode, which has a work function of $4.2eV$. The determination of work function values is crucial for comprehending the interaction between these contacts and adjacent materials.

➢ **Specifying Interface Properties**

At the interfaces between semiconductors and insulators, the surface recombination velocity and interface charge density can be defined using the INTERFACE statement. Take the following statement as an example:

```
INTERFACE QF=3e10
```

Declares that a charge of $3.10^{10} cm^{-2}$ is present in all semiconductor-insulator connections. In many cases, the interface that matters is just a small portion of the whole. This can be accomplished by utilising the INTERFACE statement's X.MIN, X.MAX, Y.MIN, and Y.MAX properties. A rectangle with the properties defined by the parameters is used to apply the interface features. To illustrate the point, take this sentence into consideration [51]:

```
INTERFACE QF=3e10 X.MIN=1.0 X.MAX=2 Y.MIN=0.0 Y.MAX=0.5
```

Limits the accumulation of electric charge at the boundary between the semiconductor and insulator to the defined rectangular area. The INTERFACE statement allows for the definition and activation of surface recombination velocity and thermionic emission, in addition to the fixed charge [51].

```
interface x.min=0 x.max=2 y.min=0 y.max=0 s.n=1e3 s.p=1e3
interface x.min=0 x.max=2 y.min=2 y.max=2 s.n=1e5 s.p=1e5
```

The given interface statements specify the existence of two interfaces within a system. The initial object is positioned at the lowermost part, extending from x=0 to x=2 and y=0, exhibiting a very modest surface charge density of 1e3. The second interface is located just above the first interface, covering the same range on the x-axis but positioned at a y-coordinate of 2. It possesses a significantly greater surface charge density of 1e5.

III.3.1.3 Choosing Numerical Methods

Altas offers three numerical methods, namely completely coupled (Newton), decoupled (Gummel), and block iteration, for solving the electrical characteristics of semiconductor devices.

The Newton iteration method is capable of solving many unknowns simultaneously and is suitable for processing huge datasets. The convergence rate is rapid, often taking between three to eight iterations, as long as the original guess is in close proximity to the final result. The Gummel iteration method solves for each unknown variable while holding all other unknowns at a constant value. A Gummel iteration is considered complete when all variables have been solved in this manner, resulting in a delayed convergence. Nevertheless, the Gummel iteration is capable of accommodating a somewhat inadequate initial estimation. Block iterations employ distinct sequences to resolve subsets of the device simulation equation, utilising Gummel for certain equation groups and Newton for others, hence reducing simulation time [115].

In general, the GUMMEL method works well when the set of equations is poorly coupled and only converges linearly. If you have a system of equations that are highly coupled and have quadratic convergence, you can use the NEWTON method. It may take longer for the NEWTON method to solve for quantities that are mostly constant or loosely coupled, though. To get convergence, NEWTON also needs a better first guess at the situation. This means that a BLOCK method can run models faster than a NEWTON method in these situations. Most of the time, GUMMEL can give better first guesses to problems. A few GUMMEL cycles can help you get a better idea of how to solve a problem. Then, go to NEWTON to finish the answer [51]. The solution method is described in the following way:

```
METHOD GUMMEL BLOCK NEWTON
```

Here is an example for the numerical method that we have used in our simulation:

```
method block newton maxtrap=40
```

The term "maxtrap=40" in the statement refers to a parameter that is linked to the Newton method. "maxtrap" is most likely an abbreviation for either "maximum iterations" or "maximum steps to take." In this scenario, the value is configured as 40, indicating that the Newton method

will be permitted to execute a maximum of 40 iterations or steps in order to reach a solution. If the algorithm fails to converge within the specified 40 iterations, it may terminate and the desired result may not be attained .

➢ **Obtaining solutions**

Atlas possesses the capacity to calculate solutions for direct current (DC), alternating current (AC) small signal, and transient situations. Obtaining solutions can be likened to setting up parametric test equipment to do device tests. The voltages on each electrode in the device are typically determined. Atlas then calculates the electric current that passes through each individual electrode. Atlas has the ability to calculate internal parameters, such as the density of charge carriers and the distribution of electric fields within the device. This relates to complex or difficult-to-measure data [51].

In every simulation, the device begins with a zero bias on all electrodes. Solutions are acquired by incrementally adjusting the biases on electrodes from their original equilibrium state. As a result of employing the initial guess technique, there are limitations on the magnitude of voltage steps. In order to preserve the outcomes, it is advisable to employ the LOG or SAVE commands [51]. In ATLAS, this part of the input deck is where the program does the math to solve for the given device. LOG, SOLVE, OUTPUT, and SAVE are the four parts that make it up [113].

• **LOG**

Log files include the terminal attributes computed by ATLAS. The following data represents the current and voltage values for each electrode in DC simulations. During transient simulations, the temporal information is stored. The tiny signal frequency, conductances, and capacitances are recorded during AC simulations [113]. As an illustration, the given statement :

```
log outf=IVlight_.log
```

For example, the current-voltage data is saved in $IVlight\_log$.

• **SOLVE**

The SOLVE statement determines the solution for one or more bias points, whether they are for D.C. or A.C. In order to obtain an initial approximation of the ultimate solution, it is imperative to carry out a simplified preliminary solution, specifically addressing Poisson's equation [113]. The syntax can be described as follows:

```
solve b1=1 name=anode
solve b1=1 vanode=0 vstep=0.01 vfinal=1.5 name=anode
```

- **LOAD and SAVE**

The LOAD and SAVE statements are employed in conjunction to facilitate the generation of more accurate initial estimates for bias points. The SAVE command is used to store simulation results in files for display or future usage as an initial estimate. Conversely, the LOAD statement is used to get a solution file whenever necessary to aid in the solution process [113].

For the simulation of a solar cell to occur, the presence of light is necessary. The illumination is activated by specifying the beam intensity in a SOLVE statement in the following manner [51]:

```
beam num=1 x.origin=1 y.origin=-30 angle=90.0 power.file=cdrom.spec reflects=1
front.refl back.reflquantum.eff=1.0
```

III.3.1.4 Interpreting results

In Atlas, the last part of the input deck is used for extracting data and plotting. The EXTRACT statement in the DeckBuild environment is used to print out required data from the file to the output deck. It can be used for extracting device parameters, such as Jsc, Voc, and efficiency. The extracted data can be saved in a file and plotted using Tonyplot [51].

The results of device simulations in Atlas are plotted by initially saving the results in a file and subsequently importing the file into Tonyplot [51].

For a structure file, the data is displayed as a 2D mesh plot, representing the device's structure. Regarding the log file scenario, Tonyplot will exhibit the data in an x-y plot, specifically showcasing the current density-voltage characteristics. (As shown in Figure III.5) [51].

The following is an example of an EXTRACT and TONYPLOT generated in atlas for our perovskite solar cell.

```
extract name="IV" curve(v."anode",i."cathode") outfile="IVcurvlight.dat"
tonyplot IVcurvlight.dat
extract name="ISC_[mA/cm^2]" y.val from curve(v."anode",i."cathode"*1e3)
where x.val=0.0
extract name="VOC_[V]" x.val from curve(v."anode",i."cathode"*1e3)
where y.val=0.0
extract name="Vmax_[V]" x.val from curve(v."anode",v."anode"*i."cathode")
where y.val=max(v."anode"*i."cathode")
extract name="Imax_[mA/cm^2]" x.val from curve(i."cathode"*1e3,v."anode"*i."cathode")
where y.val=max(v."anode"*i."cathode")
extract name="power" curve(v."anode",(v."anode"*i."cathode"))
outfile="powerlight.dat"
extract name="Pmax" max(curve(v."anode", (v."anode" * i."cathode" )))
tonyplot powerlight.dat
```

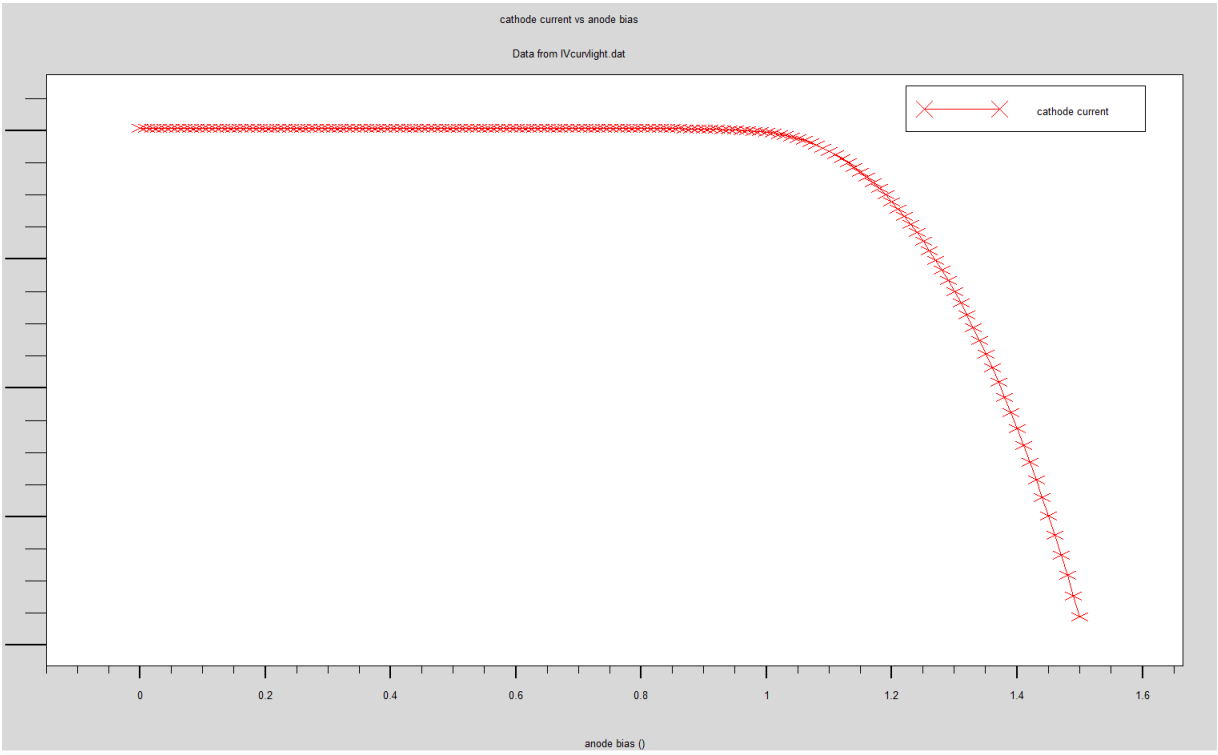

Figure III.5: Curve I-V of the solar cell from Tonyplot.

III.4 Conclusion

The SILVACO-ATLAS simulation is a highly adaptable and reliable tool used in the semiconductor industry for accurate modeling and analysis of electronic devices, including MOSFETs, transistors, diodes, and solar cells. The versatility of this technology enables the replication of intricate device setups and materials, hence aiding in the creation and enhancement of semiconductor devices. The tool is utilized in several areas such as device design, process development, reliability analysis, and failure investigation.

In the future, SILVACO-ATLAS aims to tackle problems and enhance its skills. This entails the integration of more precise models that take into account quantum phenomena and enhanced mobility. There is a requirement for more efficient simulation techniques to handle the decreasing sizes of devices. Crucial to the success of a project are comprehensive and proven models, which are supported by collaboration among stakeholders. The importance of integrating with other tools and incorporating variability and statistical analysis is growing. Furthermore, by tackling obstacles in multi-physics simulations, the tool's capacity to assess devices with intricate interactions would be improved.

In conclusion, the development of SILVACO-ATLAS simulation is primarily aimed at enhancing precision, productivity, and adaptability in order to remain at the cutting edge of semiconductor device modeling. This empowers researchers and engineers to address emerging technologies and maximize the performance of devices.

Chapter VI

Results and discussion

Chapter IV

Results and discussion

IV.1 Introduction

The chemical composition of traditional inorganic-organic halide-based perovskite solar cells (PSCs), denoted as (ABX_3), typically consists of organic cations (A) such as Methylammine (MA^+) and Formamidine (FA^+), a metal cation (B) predominantly Lead (Pb^+), and anions (X) in the form of single or mixed halides (Cl^-, Br^-, I^-). The adoption of these material compositions in the perovskite solar cell (PSC) has resulted in a remarkable photovoltaic performance. However, two significant issues contribute to its substantial limitation in industrial applications. The primary factor contributing to the intrinsic instability of the PSC is the presence of organic volatile components. The chemical instability of organic-inorganic based perovskite solar cells (PSCs) is attributed to their unsteady and their Capability to absorb moisture from the air properties of the organic cations. When subjected to oxygen, humidity, and elevated temperature, these PSCs experience a loss of stability.

The second parameter pertains to the emergence of toxicity resulting from the utilisation of the lead element, which poses a significant risk to both human health and environmental sustainability. To address this limitation, researchers have conducted thorough investigations into the adoption of inorganic materials and lead-free compositions for the core absorber layer in perovskite solar cells (PSCs). In this context, the inorganic cation cesium (Cs^+) has emerged as a highly preferred alternative to organic cations such as MA+ and FA+. This preference is primarily attributed to the superior thermal stability exhibited by cesium, which has the potential to greatly extend the operational lifetime of devices [116].

The remarkable optoelectronic capabilities of lead-free double halide perovskites, specifically those with the chemical formula A_2BCX_6, have gained significant recognition in the field of photovoltaics. Due to their exceptional steadiness in the environment, appealing electronics and optics characteristics, and minimal poisonousness, it might be regarded as a feasible substitute for lead-based perovskites. Synthesizing halide double perovskites (HDPs) results in problems due to the presence of undesired phases during their production. Recently, sev-

eral compounds including Cs_2NaBiI_6, $Cs_2AgInCl_6$, $Cs_2AgSbCl_6$, and Cs_2AgBiX_6 (X = Br, Cl) have been successfully synthesised. Due to its lack of toxicity and exceptional properties that make it well-suited for usage in perovskite solar cells (PSCs) [4].

Cs_2BiAgI_6 exhibits promising characteristics as a potential substitute for lead-based perovskites. Substituting the inorganic cesium Cs^+ cation for the organic 'A' cation may raise the breakdown energy by as much as $-0.069eV$, hence improving the stability to its optimal level. The main goal was to solve the toxicity problem by replacing the cation at the Pb^+B site, while making sure that the device's performance and safety were not affected. The adoption of double substitution, in particular the substitution of lead with the monovalent cations of silver (Ag^+) and bismuth ($Bi_6{}^{+3}$) in perovskite solar cells (PSCs) based on cesium have gained a lot of attention as a potential replacement. The contributing variables include an appropriate bandgap, strong optical absorbance, and higher coulomb interaction energy, which greatly improve stability and result in a high decomposition energy of $0.38eV$. Double perovskite materials based on monovalent Ag^+ and Bi^{3+} have recently shown great promise as efficient solar cell materials, according to recent investigations. This is because of their enhanced stability, longer carrier recombination lifespan, better photoluminescence lifetime, ideal band gap, and favorable charge carrier effective mass [116].

This chapter delves into numerical simulations of various structures for perovskite-based photovoltaic solar cells, specifically focusing on $MAPbI_3$ and Cs_2BiAgI_6 materials. Our goal is to enhance the electrical performance of these devices using the Atlas 2018 software. The study begins by introducing a solar cell configuration based on a p-i-n double perovskite structure. This configuration includes layers of SiO_2/ITO/NiO/Cs_2AgBiI_6/ZnO/Ag To optimize performance,several Electron Transport Materials (ETMs) and Hole Transport Materials (HTMs) are employed. Here are the key aspects we investigate:

oping Densities Optimization: Numerical simulations is performed to determine the optimal doping densities for the hole transport layer (HTL) and electron transport layer (ETL). Careful selection of these densities significantly impacts device performance.

The Indium Tin Oxide (ITO) Work Function: ITO is a critical layer in solar cells. Its work function affects charge transport and overall efficiency.

Back contact: The choice of back contact material plays a role in electron extraction and overall device behavior.

In the second part of the study, the application of beta-gallium oxide (β-Ga_2O_3) as a flexible and multifunctional element within perovskite solar cells (PSCs) is investigated. β-Ga_2O_3 plays several crucial roles, each contributing to the overall performance of these photovoltaic devices:

Electron Transport Layer (ETL): β-Ga_2O_3 serves as an efficient ETL, facilitating the movement of electrons within the solar cell structure. Its unique properties enhance charge transport, leading to improved efficiency.

Window Material with Reduced Reflection: As a window layer, β-Ga_2O_3 minimizes the reflection of visible light. This property ensures optimal light absorption by the perovskite

layer, enhancing overall energy conversion.

UV Absorption for Perovskite Stability: The presence of β-Ga_2O_3 absorbs harmful ultraviolet (UV) radiation, contributing to the stability of the perovskite layer. UV-induced degradation is a common challenge in solar cells, and β-Ga_2O_3 helps mitigate this issue.

Hole-Blocking Layer (HBL): Due to its significant valence band-offset, β-Ga_2O_3 acts as an effective HBL. It prevents unwanted charge recombination by blocking holes from migrating to the electron transport layer

Besides, a bilayer structure will be incorporated; Cuprous Oxide/Silicon (Cu_2O/p-Si) as HTL and EBL: The Cu_2O/p-Si bilayer serves as both the hole transport layer (HTL) and the electron blocking layer (EBL). It complements β-Ga_2O_3's functions, ensuring efficient charge separation and preventing carrier losses.

In addition, a specific focus lies in analyzing the impact of various factors on solar cell performance:

The influence of the variation of the perovskite absorber layer on efficiency. Methylammonium lead iodide ($CH_3NH_3PbI_3$) is used as the perovskite absorber.

Traps effect within the perovskite, β-Ga_2O_3, and Cu_2O layers. Minimizing traps is crucial for maintaining charge carriers and overall device stability.

By optimizing all these parameters, we aim to create more efficient and cost-effective solar cells, contributing to sustainable energy solutions.

IV.2 Part 1: Study of Cs_2BiAgI_6 double perovskite solar cell

IV.2.1 Solar cell structure

In this case, the double perovskite solar cell is formed by associating the Cs_2BiAgI_6 absorber layer with ETL, HTL, and back contact. The absorber's solar cell structure is a p-i-n configuration made of Cs_2BiAgI_6. A p-i-n structure has better long-wavelength responsiveness than a regular semiconductor p-n junction. Deep inside the device, encompassing the intrinsic area is also where the p-i-n structure depletion zone is located. Photons with extended wavelengths can deeply penetrate cells. However, it should be mentioned that the generation of current is limited to electron-hole pairs that are produced either within or near the depletion region. With a larger depletion width, electron-hole pairs can be created and separated, leading to an increase in the quantum efficiency of the cell. The ability to capture photons is a result of the double heterostructure in Cs_2BiAgI_6, which acts as an ohmic contact on both sides and confines both charge and photons [80].

The proposed architecture of the perovskite solar cell is depicted in Figure IV.1b, which is an p-i-n heterojunction with an active layer of Cs_2AgBiI_6sandwiched between an ETL of zinc oxide (ZnO) and an HTL of nickel oxide (NiO). Silver and transparent indium tin oxide (ITO) compose the rear and front contacts, correspondingly. After the light absorber layer

creates electrons and holes, the holes move to the NiO layer and finally to the ITO contact. As an opposite, the electrons complete the circuit by travelling through the ZnO layer and arriving at the Ag contact. The proposed device configuration consists of the following layers: SiO_2/ITO/NiO/Cs_2AgBiI_6/ZnO/Ag.

All of the required input parameters have unique properties for each layer of the device and must be set before the simulation can run. The parameters, which are derived from published works, are listed in Table IV.1. The illumination was configured to$AM1.5G$ with an intensity of $1000W/m^2$, and the temperature was set to 300 K. Indium tin oxide (ITO) has a work function of $5.2eV$, while silver (Ag) has a work function of$4.2eV$. Table IV.2 shows the density of traps inside the device's active layer.

Figure IV.1a shows the energy band diagram of the p-i-n perovskite solar cell. The figure is crucial for understanding how solar cells convert light into electricity. The diagram shows the included materials into the solar cell that are SiO_2, ITO, NiO, Perovskite, ZnO and Ag, each with unique electronic properties essential for the cell's function. The conduction band (blue line), valence band (red line), and equilibrium Fermi level (black line) are fundamental in determining how, across the layers, electrons and holes are excited and move to generate an electric current.

Plotting this diagram helps in optimizing the solar cell's efficiency by tailoring the materials and their energy levels even that it is a simplified representation, and actual solar cells may have more complexities involved in their operation. The figure shows mainly that the perovskite and ZnO layers have highly different conduction band energy levels, which allows for effective electron transport. In a similar manner, the perovskite and NiO layers have almost identical valence band energy levels, which makes hole extraction and transport much easier. The diagram indicates that the perovskite layer exhibits a high absorption coefficient and a low recombination rate due to its comparatively narrow band gap and the positioning of the Fermi level toward the middle of the gap. The diagram suggests that the solar cell can get superior efficiency and stability through the optimization of layer thickness and quality, as well as interface engineering and device architecture.

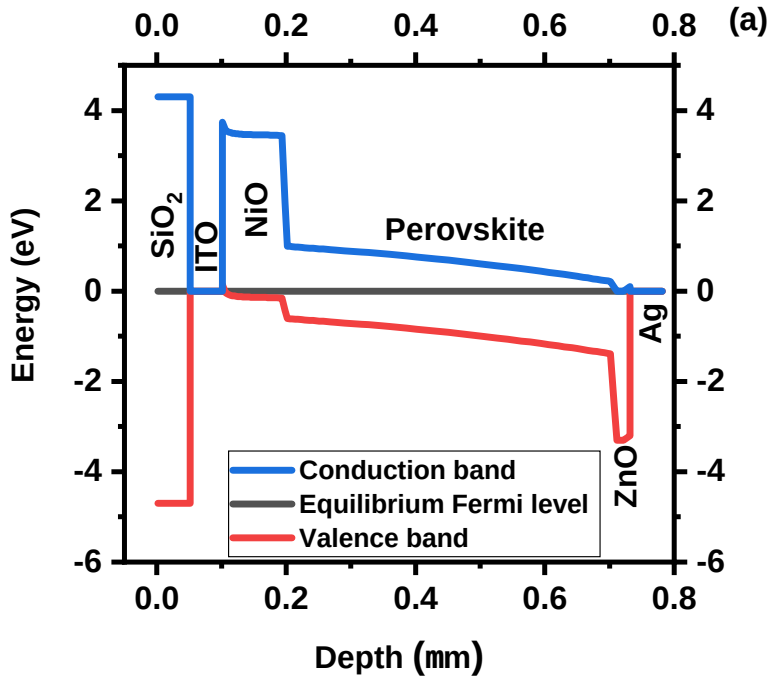

(a) Energy diagram.

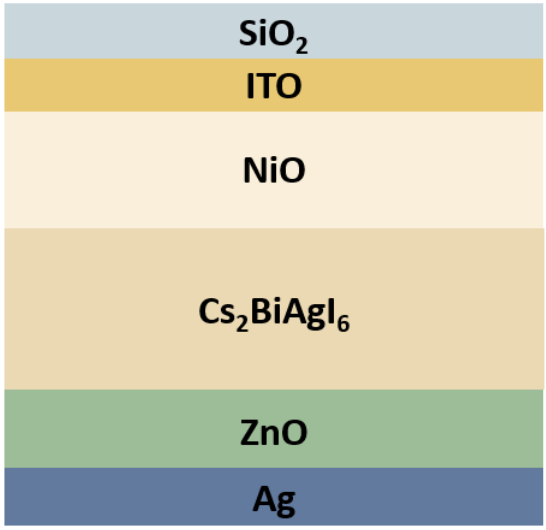

(b) Solar cell structure

Figure IV.1: Energy Band Diagram and Layer Structure of a Perovskite (Cs_2BiAgI_6) Solar Cell

Table IV.1: Materials parameters of different layers used in the simulation of PSC [80].

Parameter	CS_2BiAgI_6	ZnO	NiO
Bandgap (eV)	1.6	3.3	3.6
Affinity (eV)	3.9	4.1	1.46
Hole mobility $\left(cm^2V^{-1}s^{-1}\right)$	2	10	5
Electron mobility $\left(cm^2V^{-1}s^{-1}\right)$	2	30	12
Relative permittivity	6.5	9	11
$N_c\left(cm^{-3}\right)$	$1\cdot10^{19}$	$4\cdot10^{18}$	$1.6\cdot10^{19}$
$N_v\left(cm^{-3}\right)$	$1\cdot10^{19}$	$1\cdot10^{19}$	$1\cdot10^{19}$
$N_A\left(cm^{-3}\right)$	$1\cdot10^{15}$	-	$1\cdot10^{17}$
$N_D\left(cm^{-3}\right)$	-	$5\cdot10^{18}$	-
$\tau_n/\tau_p(ns)$	1/1	1 /1	1/1
Thickness (μm)	0.5	0.03	0.1

Table IV.2: Cs_2BiAgI_6 related traps.

	Trap level (eV)	Density $(cm-^3)$	Hole capture section (cm^2)	Electron capture section (cm^2)
Cs_2BiAgI_6 [4]	0.6	$9.1\cdot10^{16}$	$1\cdot10^{-15}$	$1\cdot10^{-14}$

IV.2.2 Results and discussion

IV.2.2.1 Primary optimized devices

Prior to delving into the examination of the Hole Transport Layer (HTL)'s impact, our approach commenced with the plotting of the J-V characteristic curve for the initial device configuration. This step was essential for setting a benchmark for our study. The device, comprising a structure of NiO/Cs_2BiAgI_6/ZnO, was meticulously analyzed and its performance metrics were directly compared against existing data within the scientific literature. Illustrated in Figure IV.2, the preliminary findings revealed a power conversion efficiency (PCE) of 14.05%, alongside an Open Circuit Voltage $(V_{oc})$of $0.92V$. Additionally, the device demonstrated a Fill Factor (FF) of 72.81% and a Short Circuit Current (J_{sc}) of $19.97mA/cm^2$. These initial metrics not only served as a foundation for further investigation but also provided a comprehensive overview of the device's baseline performance within the context of contemporary research findings.

When comparing the results obtained with previous research on the same absorber layer Cs_2BiAgI_6, it is evident that M. Khalid Hossain et al. showcased that CBTS serves as the most optimal HTL for Cs_2BiAgI_6among the eight ETLs considered in their study [117]. This optimization resulted in an impressive power conversion efficiency (PCE) ranging from 14.44% to 21.59% with a variety of materials such as PCBM, TiO_2, ZnO, C60, IGZO, SnO_2, CeO_2, and WS_2. Notably, our initial findings align well with recent research outcomes.

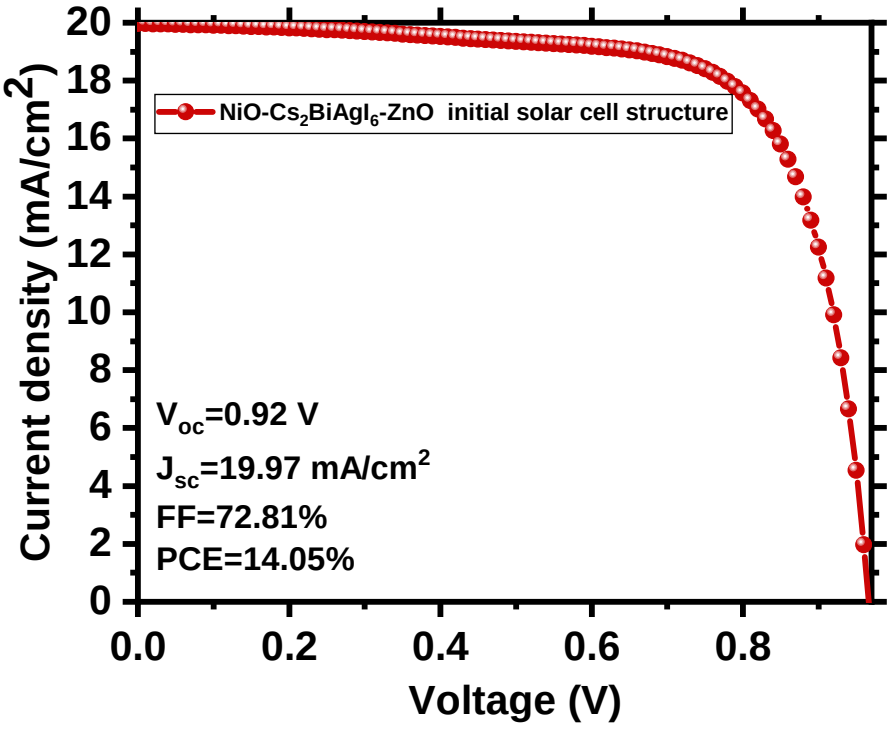

Figure IV.2: J-V characteristic of the initial simulated device structure.

IV.2.2.2 Effect of Changing HTL

The hole transport layer (HTL) is the functional component of the PSCs device that collects holes from the Cs_2BiAgI_6 perovskite material and transfers them to the ITO front transparent contact. In this simulation, we have employed different forms of HTL to maximize the performance of the device, as shown in Table IV.3. This section of the study evaluates the effect of different HTLs, including NiO, CuI, CuO, Cu_2O, $CuSbS_2$, $CuAlO_2$, P_3HT, CuSCN, MoO_3, V_2O_5, Spiro-MeOTAD, and PEDOT:PSS.

FigureIV.3 depicts the current density-voltage characteristics of Cs_2BiAgI_6 perovskite solar cells when using different (HTL) materials. The curve demonstrates that CuI is the most suitable HTL material, with CuSCN and NiO closely behind, as they exhibit the greatest values for J_{sc}, V_{oc},FF, and PCE. The curve also indicates that certain HTL materials, like $CuAlO_2$, P_3HT, and V_2O_5, are not suitable for Cs_2BiAgI_6 perovskite solar cells. This is due to their significantly lower J_{sc} values, which signify inadequate hole extraction and transport capabilities. According to the curve, selecting the right HTL material is crucial for Cs_2BiAgI_6 perovskite solar cells to perform at their best.

Table IV.3 illustrates the critical performance metrics for various materials serving as HTLs in Cs_2BiAgI_6 perovskite solar cells. Calculated parameters include Power Conversion Efficiency (PCE), Fill Factor (FF), Short-Circuit Current Density (J_{sc}), and Open-Circuit Voltage (V_{oc}). The findings reveal that CuI achieves the highestPCE value of 22.23%, closely trailed by CuSCN at 17.99%. Furthermore, P_3HT demonstrates the highest FF value at 81.53%, marginally surpassing Cu_2O with a FF of 79.38%. Notably, CuI displays the highest J_{sc} value at $30.35 mA/cm^2$, with CuSCN following closely at $24.93 mA/cm^2$. The superior performance of CuI based devices can be attributed to their enhanced carrier mobility and favorable valence band offset (VBO),resulting in a heightened FF. Remarkably, all organic HTL materials exhibit comparable J_{sc} values. These insights underscore the significance of material selection in optimizing perovskite solar cell performance, with CuI emerging as a promising candidate due to its favorable characteristics.

Table IV.3: Material parameters of different HTL layers [80].

HTL	$d\,(\mu m)$	$E_g\,(eV)$	$\chi\,(eV)$	$\varepsilon\,(ev)$	$\mu_n\left(\frac{cm^2}{V.s}\right)$	$\mu_p\left(\frac{cm^2}{V.s}\right)$	$N_c\left(cm^{-3}\right)$	$N_v\left(cm^{-3}\right)$	$N_A\left(cm^{-3}\right)$	$N_D\left(cm^{-3}\right)$	$\frac{\tau_n}{\tau_p}$
CuI	0.1	3.1	2.1	6.5	100	43.9	$2.8\cdot10^{19}$	$1\cdot10^{19}$	$1\cdot10^{18}$	/	1/1
CuSCN	0.1	3.6	1.7	10	100	25	$2.2\cdot10^{19}$	$1.8\cdot10^{18}$	$1\cdot10^{18}$	/	1/1
$CuAlO_2$	0.1	3.46	2.5	60	2	8.6	$2.2\cdot10^{18}$	$1.8\cdot10^{18}$	$3.6\cdot10^{18}$	/	1/1
CuO	0.1	1.51	4.07	18.1	100	0.1	$2.2\cdot10^{19}$	$5.5\cdot10^{20}$	$1\cdot10^{18}$	/	1/1
Cu_2O	0.1	2.2	3.4	7.5	200	8600	$2\cdot10^{19}$	$1\cdot10^{19}$	$1\cdot10^{18}$	/	1/1
$CuSbS_2$	0.1	1.58	4.2	14.6	49	49	$2\cdot10^{18}$	$1\cdot10^{19}$	$1\cdot10^{18}$	/	1/1
P3HT	0.1	1.7	3.5	3	$1.8\cdot10^{-3}$	$1.86\cdot10^{-3}$	$2\cdot10^{21}$	$2\cdot10^{21}$	$1\cdot10^{18}$	/	1/1
Spiro-MeOTAD	0.1	3	2.2	3	$2.1\cdot10^{-3}$	$2.16\cdot10^{-3}$	$2.2\cdot10^{18}$	$1.8\cdot10^{19}$	$1\cdot10^{18}$	/	1/1
PEDOT:PSS	0.1	1.6	3.4	3	$4.5\cdot10^{-2}$	$4.5\cdot10^{-2}$	$2.2\cdot10^{18}$	$2.2\cdot10^{19}$	$1\cdot10^{18}$	/	1/1
V_2O_5	0.1	2.2	4	10	320	40	$9.2\cdot10^{17}$	$5\cdot10^{18}$	$1\cdot10^{18}$	/	1/1
MoO_3	0.1	3	2.5	12.5	25	100	$2.2\cdot10^{18}$	$1.8\cdot10^{18}$	$1\cdot10^{18}$	/	1/1

The CuSCN, CuI,NiO, MoO_3, and Cu_2O HTLs exhibited significantly higher power con-

version efficiencies (PCEs) ranging from approximately 12% to 22% compared to the other HTLs.However, unlike the other HTLs, the V_2O_5, P_3HT, and $CuAlO_2$ HTLs exhibited lower power conversion efficiencies $(PCEs)$ of 8.29%, 8.08%, and 6.31%, respectively, as shown in Table IV.4. We noticed that, with a few notable exceptions, inorganic HTLs outperformed their organic counterparts. This is because inorganic HTLs possess qualities like enhanced stability, excellent band alignment as shown in Figure IV.4, and great transparency.

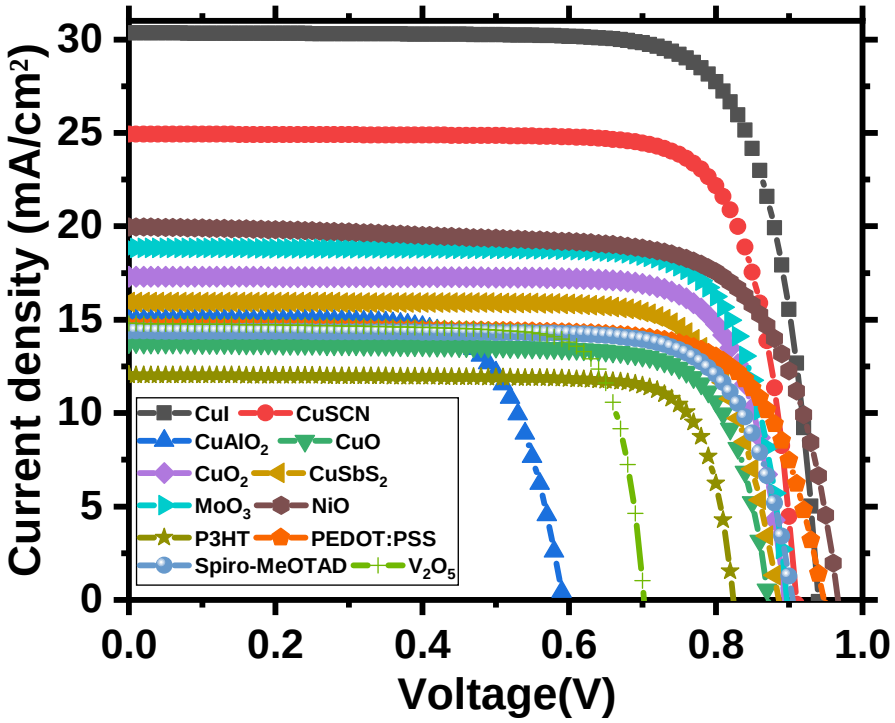

Figure IV.3: J-V characteristic curves for various Hole Transport Layers (HTLs).

Table IV.4: output values for different HTL materials.

HTL material	$PCE\,(\%)$	$FF\,(\%)$	$J_{sc}\left(\frac{mA}{cm^2}\right)$	$V_{oc}\,(V)$
NiO	14.05	72.82	19.97	0.97
CuI	22.23	77.92	30.35	0.94
CuO	9.34	77.67	13.79	0.87
Cu_2O	12.27	79.38	17.30	0.89
$CuSbS_2$	10.69	77.69	15.94	0.89
$CuAlO_2$	6.31	71.13	14.99	0.59
P3HT	8.08	81.53	12.03	0.82
CuSCN	17.99	79.34	24.93	0.91
MoO_3	13.42	79.38	18.83	0.90
V_2O_5	8.29	79.79	14.80	0.70
Sipro-MeOTAD	10.04	77.14	14.39	0.90
PEDOT:PSS	10.45	75.59	14.59	0.95

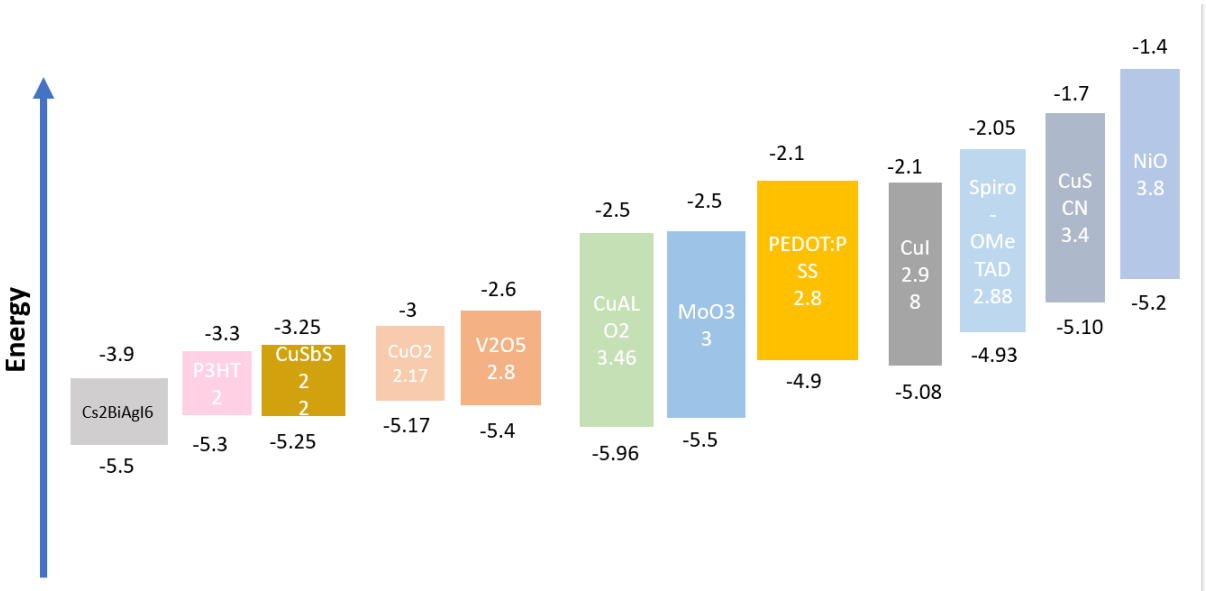

Figure IV.4: Energy level diagram of several Hole Transport Materials (HTMs).

Effect of the HTL thickness

The highest efficiency HTL retained in this section is CuI. Various CuI thicknesses, ranging from 30 to 100*nm*, were experienced to investigate the impact of the optimal HTL thickness on solar cell efficiency. Figure IV.5 illustrates the relationship between device characteristics and the thickness of CuI. From Figure IV.5b, it is observed that the *PCE*,*Voc*, and *Jsc* increase as the thickness of CuI increases from 30 nm to 60 nm. However, beyond the 60 nm threshold, these parameters start to decrease. This behavior can be explained by the fact that when the CuI

thickness exceeds a certain limit, it impedes the movement of photo-generated holes toward the contact electrode. On the other hand, the FF increases when the CuI thickness ranges from 30*nm* to 100*nm*. This improvement may be attributed to reduced shunt resistance and the occurrence of current leakage due to the thinness of the material [4].

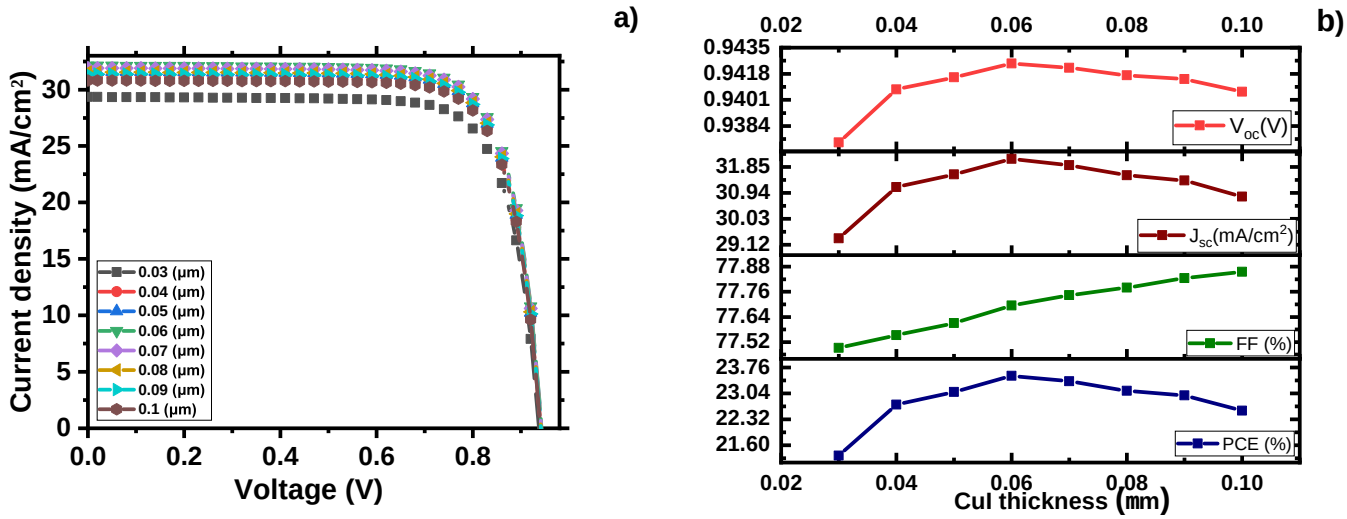

(a) effect of CuI thickness on the J-V characteristics of the solar cell

(b) The relationship between CuI thickness and the characteristics of solar cells

Figure IV.5: a) effect of CuI thickness on the J-V characteristics of the solar cell. b) The relationship between CuI thickness and the characteristics of solar cells.

IV.2.2.3 Effect of Cs_2BiAgI_6 thickness for different ETL materials:

FigureIV.6 illustrates the impact of various ETL materials on the output characteristics of solar cells as the thickness of Cs_2BiAgI_6 varies. The thickness of the perovskite layer ranges from 0.6 to 1.2 µm. Suggested ETL materials include β-Ga_2O_3, WO_3, WS_2, SnO_2, TiO_2, IGZO, and ZnS. Detailed material parameters for each ETL are provided in Tables IV.1 and IV.5

Table IV.5: Material parameters of different ETL layers [4, 80, 118, 119].

ETL	ZnSe	CdS	ZnS	WO_3	WS_2	IGZO	β-Ga_2O_3	TiO_2	SnO_2
Thickness (μm)	0.3	0.3	0.3	0.3	0.3	0.3	0.3	0.3	0.3
Band gap, $E_g\,(eV)$	2.81	2.4	3.6	2.6	1.8	3.05	4.8	3.2	3.6
Electron affinity,$\chi\,(eV)$	4.09	4.18	4.45	3.8	3.95	4.16	4	4	4
Relative permittivity,$\varepsilon\,(eV)$	8.6	10	9	4.8	13.6	10	11	9	9
Electron mobility,$\mu_n\left(\frac{cm^2}{V.s}\right)$	400	100	100	30	100	15	300	20	100
Electron mobility,$\mu_p\left(\frac{cm^2}{V.s}\right)$	110	25	25	30	100	0.1	10	10	25
$N_c\,(cm^{-3})$	$2.2.10^{19}$	$2.2.10^{18}$	$2.2.10^{18}$	$2.2.10^{21}$	$2.2.10^{17}$	5.10^{18}	2.10^{21}	$1.8.10^{19}$	$1.8.10^{19}$
$N_v\,(cm^{-3})$	$1.8.10^{18}$	$1.9.10^{19}$	$1.9.10^{19}$	$2.2.10^{21}$	$2.2.10^{16}$	5.10^{18}	2.10^{21}	$1.8.10^{19}$	$1.8.10^{19}$
$N_A\,(cm^{-3})$	/	/	/	/	/	/	/	/	/
$N_D\,(cm^{-3})$	1.10^{18}	1.10^{18}	1.10^{18}	$6.35.10^{17}$	1.10^{18}	1.10^{17}	1.10^{16}	1.10^{21}	9.10^{16}
$\frac{\tau_n}{\tau_p}\,(10^{-7}s)$	/	/	/	/	/	/	/	/	/

The graph in Figure IV.6a clearly shows that the*PCE* and the thickness of the Cs_2BiAgI_6 layer are related. Initially, as the thickness grows, the *PCE* also increases. This indicates that there is an optimal thickness of the perovskite layer required to accomplish maximum light absorption and creation of charge carriers. Nevertheless, after it reaches its highest point, the *PCE* tends to stabilize or slightly decline as the thickness increases further. This phenomenon may be attributed to the increased prominence of recombination losses in larger perovskite layers, or to constraints in charge carrier extraction.

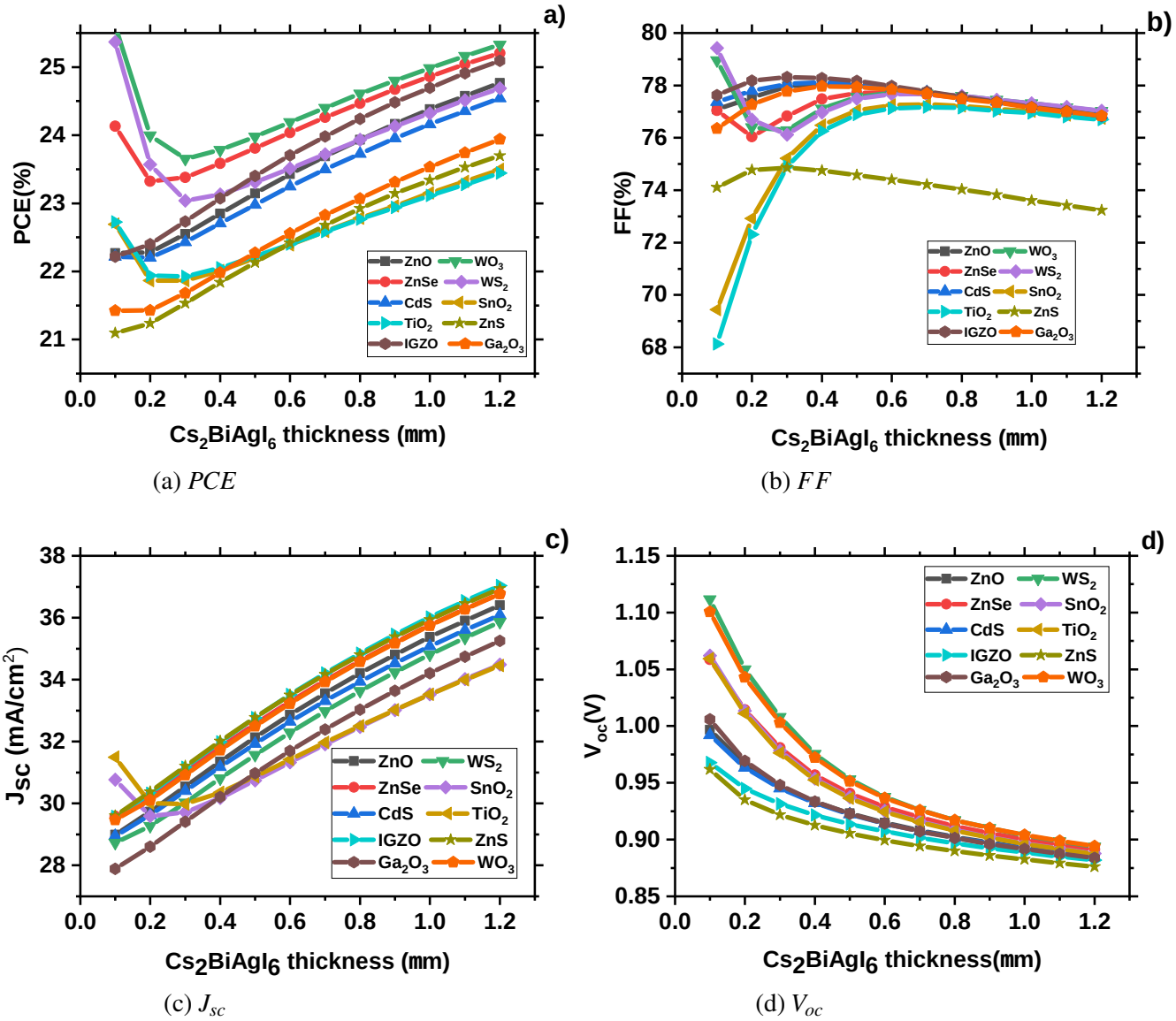

(a) *PCE* (b) *FF*

(c) J_{sc} (d) V_{oc}

Figure IV.6: Curves depicting the relationship between the thickness variation of Cs_2AgBiI_6 and output parameters for many ETMs.

The ETL materials also show different patterns and*PCE* values, which suggests that the choice of ETL can have a big effect on how well the solar cell works. For example, certain materials like as TiO_2 and SnO_2 exhibit a consistent rise in power conversion efficiency (PCE) as the perovskite layer thickness increases, but materials like ZnO and ZnSe demonstrate a more

prominent peak followed by a stabilization. The differences in energy band alignments, charge carrier mobilities, and recombination rates at the interfaces between Cs_2BiAgI_6 and the various ETLs could explain this phenomenon.

Figure IV.6b presents the variations in FF percentages as the thickness of Cs_2BiAgI_6 varies across different ETL materials. Initially, all ETL materials demonstrate uniformFF values at lower Cs_2BiAgI_6 thickness levels. However, differences arise around 0.2 µm thickness. With increasing thickness, materials such as ZnS,β-Ga_2O_3, and $IGZO$ maintain consistently higher FF levels, hovering around 78%. Similarly, theFF corresponding to other materials like ZnO, ZnSe, CdS,WO_3, WS_2,SnO_2, and TiO_2 remain stable, although at slightly lower values. This observation underscores the influence of Cs_2BiAgI_6 thickness on the corresponding FF of the materials.

The Figure IV.6c depicts a line graph showcasing the correlation between $J_{sc}(mA/cm^2)$and | thickness for several materials, The graph illustrates a consistent increasing trajectory for all materials, suggesting that when the thickness of Cs_2BiAgI_6 grows from 0.6 to $1.2\mu m$, there is a discernible augmentation in J_{sc}. The lines depicting each material have almost parallel orientation, indicating a uniform rise in J_{sc} as the thickness of the materials increases. This suggests that the thickness of Cs_2BiAgI_6 has a direct influence on the J_{sc} of these materials.

The Figure IV.6d depicts a line graph showing the correlation between the thickness of Cs_2BiAgI_6 and $V_{oc}$for different ETL materials. The graph illustrates a consistent decline in all materials, suggesting that when the thickness of Cs_2BiAgI_6 increases, there is a significant reduction in V_{oc}. Increasing the thickness of Cs_2BiAgI_6 is likely to result in a reduction in the open circuit voltage of these materials. However, each material exhibits this trend at varying rates and magnitudes, indicating that the particular features of the material also influence this correlation.

The solar device utilizing WO3 as the electron transport layer (ETL) achieves the highest (PCE),specifically reaching a optimum PCE of 25.32% (with aV_{oc} of $0.89V$, J_{sc} of $36.77mA/cm2$, and FF of 77.02%). This PCE is obtained with a Cs_2AgBiI_6 thickness of$1.2\mu m$, which is believed to be the optimal thickness. WO_3 is a material with a higher performance as an electron transport layer (ETL) compared to other materials. Its low conduction band offset (CBO) as shown in Figure IV.7 results in a low barrier, facilitating electron passage to the electrode. This improved performance is attributed to the presence of a spike at the interface between the ETL and absorber [4].

Effect of the ETL thickness

The primary function of the ETL layer is to move electrons from the absorber layer to the Ag while keeping them from combing with holes in the absorber layer. The thickness of the ETL is critical in order to get optimal performance. When the ETL gets thicker, the series resistance also gets higher, which causes recombination. In this section, the best ETL which is WO_3 is chosen and its thickness has been varied, from 0.03 to $0.1\mu m$. Figure IV.8b depicts the result on

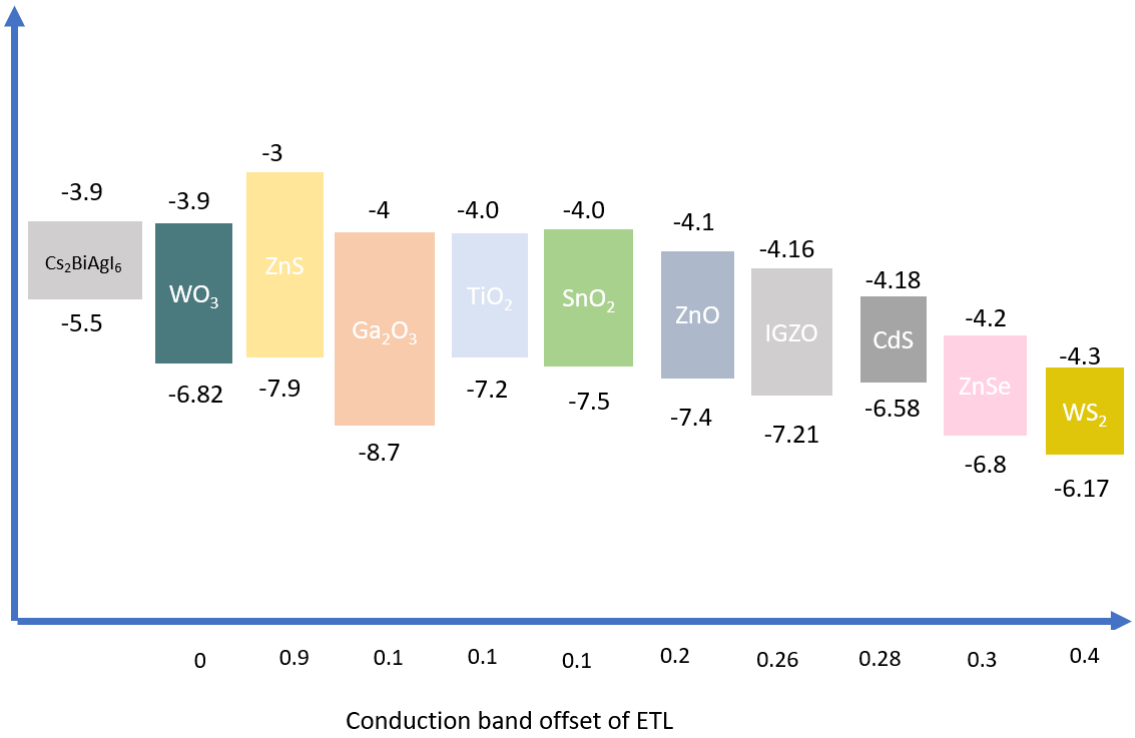

Figure IV.7: Energy level diagram and conduction band offset of several Electron Transport Materials (ETMs).

V_{oc}, J_{sc}, FF and PCE. The outputs of the PSC are unaffected by the thickness of the WO_3 layer as long as it surpasses a specific minimum value. The reason for this is that Cs_2BiAgI_6 has a relatively high electron mobility, facilitating the efficient transportation of electrons even over thin ETL layers. Due to its small band gap, the ETL layer has a lower resistance. Therefore, the optimal ETL thickness is chosen to be $0.1\mu m$ [120].

IV.2.2.4 Effect of doping concentration of HTL

The acceptor density has been increased from 10^{16} to $10^{19} cm^{-3}$ in order to predict its effect on solar cell performance. The impact of different levels of CuI doping concentration on the solar cell outputs is illustrated in Figure IV.9b. As the concentration of CuI doping increases, the open circuit voltage V_{oc} remains relatively constant, exhibiting negligible variation. The current generation at greater doping levels is significantly reduced, leading to a substantial decline in J_{sc}. FF has an early rise followed by stabilization, indicating an enhancement in performance within a particular range of doping densities. PCE and V_{oc} exhibit a comparable pattern to the J_{sc}. Consequently, augmenting the CuI doping concentration can improve specific performance a solar cell like as FF. However, it can also result in a decline in other (J_{sc}, V_{oc} and PCE). For a solar cell the most important performance is PCE.

Nevertheless, the highest attainable PCE is determined to be 32.62% when the optimal N_A value is selected as 110^{16}, as greater NA values can generate coulomb traps, leading to reduced hole mobility [120]. The cell's optimum suggested (PCE), (FF), (V_{oc}), and (J_{sc}) values are

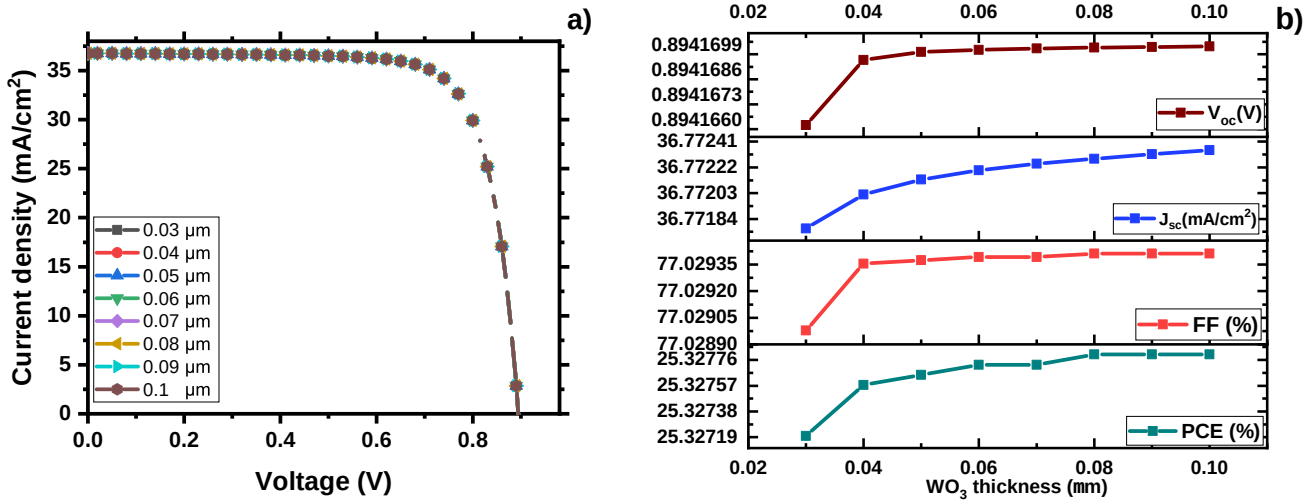

(a) effect of WO_3 thickness on the J-V characteristics.

(b) variation of the solar cell's output parameters with WO_3 thickness.

Figure IV.8: a) effect of WO_3 thickness on the J-V characteristics. b) variation of the solar cell'soutput parameters with WO_3 thickness.

32.62%,76.63%, 0.92 V, and 46.30 mA/cm2 respectively, with an HTL doping concentration (N_A) of $1 \cdot 10^{16} cm^{-3}$.

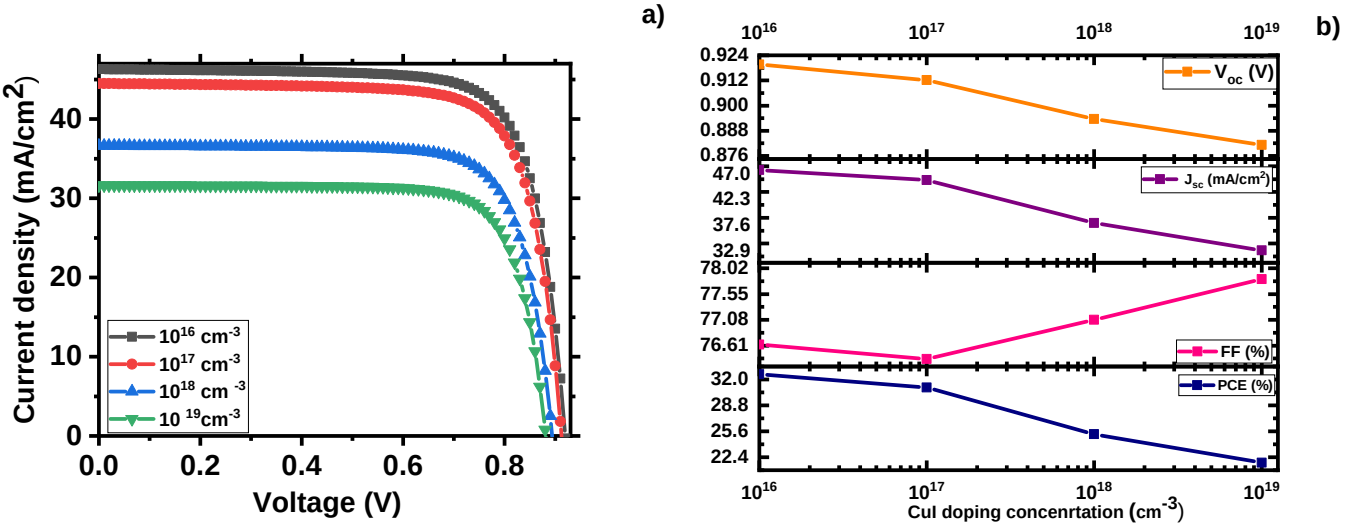

(a) Variation of photovoltaic parameters with respect to doping density (N_A) of CuI.

(b) effect of CuI doping concentration on the J-V characteristics of the solar cell.

Figure IV.9: a) Variation of photovoltaic parameters with respect to doping density (N_A) of CuI. b) effect of CuI doping concentration on the J-V characteristics of the solar cell.

IV.2.2.5 Effect of doping concentration of ETL

Figure IV.10a and IV.10b depicts the impact of different concentrations of WO_3 doping on the J-V characteristics and electrical outputs. The donor density is changed within the range of $10^{16}$to$10^{19} cm^{-3}$ in order to optimize performance. As the concentration of doping increases,

the opencircuit voltage (V_{oc}) remains practically steady with minor variations. The current density at higher doping levels is slightly increased. The fill factor (FF) demonstrates a little upward trend. The power conversion efficiency (PCE) likewise increases slightly. The obtained results indicates that higher levels of WO_3 doping has no considerable effect.

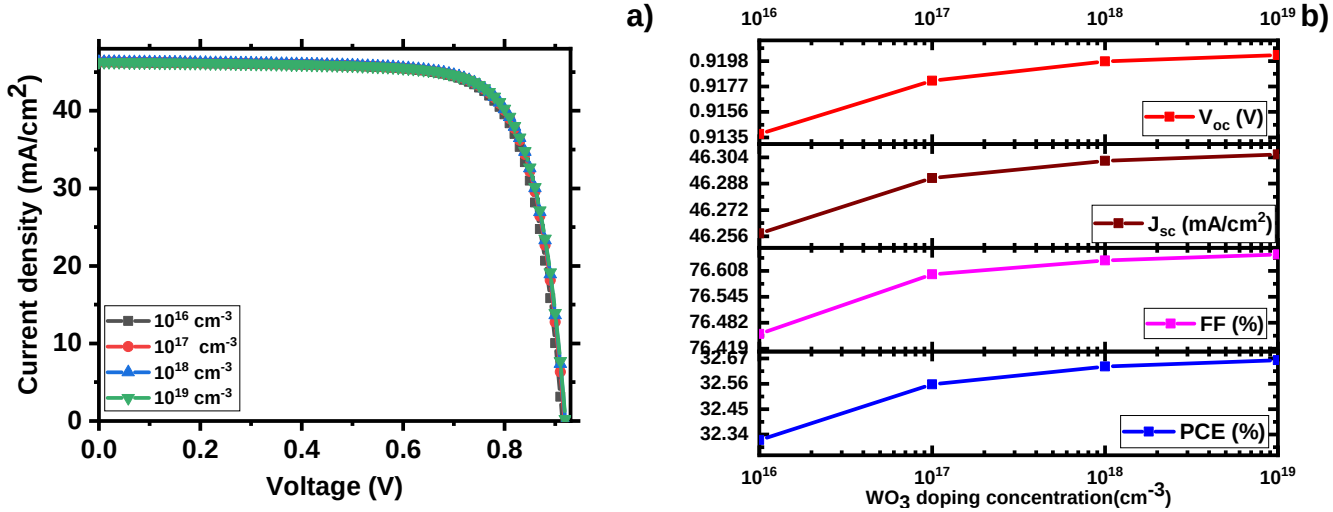

(a) Effect of WO_3 doping concentration on the J-V characteristics of the solar cell.

(b) Variation of photovoltaic parameters with respect to doping density (N_D) of WO_3.

Figure IV.10: a) effect of WO_3 doping concentration on the J-V characteristics of the solar cell. b) Variation of photovoltaic parameters with respect to doping density (N_D) of WO_3.

IV.2.2.6 Effect of ITO work-function

The front contact is established via Indium Tin Oxide (ITO). There have been reports indicating that the work function of the ITO can be artificially manipulated [4]. The simulation analysis used an initial work function of $5.2eV$ for the ITO electrode, which was used as the top electrode. In this step; the value of the ITO work function (φ) is changed from $4.6eV$ to $5.2eV$. The effect on electrical outputs is presented in Figure IV.11. V_{oc}demonstrates a variable pattern, reaching its highest points between 4.8 and $5.2(eV)$. Jsc demonstrates a steady rise, suggesting an improvement as the workfunction of (ITO) increases. FF likewise exhibits a consistent increase, indicating an enhancement in fill factor as the indium tin oxide (ITO) workfunction increases. PCE exhibits a parallel upward trajectory, suggesting that the increase in the indium tin oxide (ITO) workfunction leads also to an improvement in PCE.

IV.2.2.7 Effect of Back contact

The presented graph in Figure IV.12a illustrates the J-V characteristics of perovskite solar cells with different back contact materials, represented by distinct symbols and colors for each metal. The plot demonstrates that the selection of the back contact material greatly influences the performance of the solar cell. The materials subjected to testing comprise gold (Au), silver

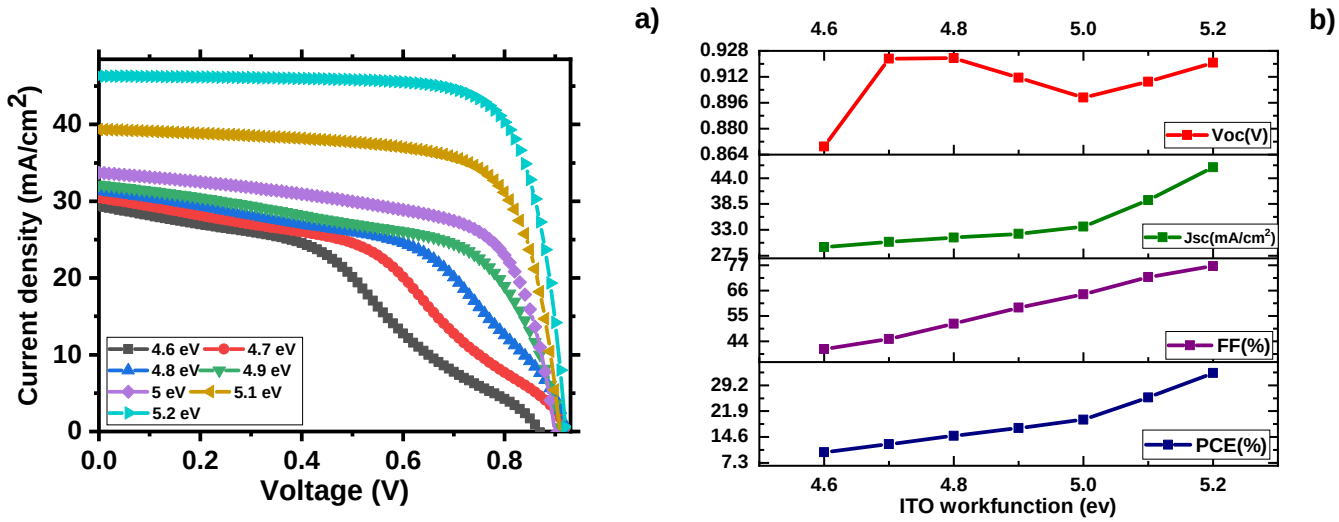

(a) J-V curve variation for different ITO work function.

(b) Electrical output parameters for different ITO work function.

Figure IV.11: a) J-V curve variation for different ITO work function. b) Electrical output parameters for different ITO work function.

(Ag), aluminum (Al), tungsten (W), iron (Fe), nickel (Ni), molybdenum (Mo), and copper (Cu).

Figure IV.12b illustrates the outputs obtained using back-contact work functions related to the suggested materials, ranged from 4.06 to $5.31eV$. As the workfunction of the back contact increases from 4.0 to$5.5eV$,V_{oc} shows a declining trend, suggesting a decrease in the voltage when no current is flowing. J_{sc} has a non-uniform distribution characterized by two distinct peaks around 4.25 and $4.75eV$, indicating fluctuations in the density of short-circuit current at these specific energy levels. FF drops consistently as the work function of the back contact increases. PCE exhibits a comparable decline as the V_{oc} and FF, suggesting that increased back contact work functions lead to decreased power conversion efficiency.

The solar cells designed with silver (Ag) back contacts exhibit, then, the maximum current density over the whole voltage spectrum, indicating exceptional efficacy in converting light into power.The explanation behind this could be because of the remarkable conductivity and chemical stability of silver. These properties are vital for efficient charge collection and the long-term stability of solar cells. In contrast, cells with gold (Au) and iron (Fe) back contacts exhibit significantly reduced current density values. This can be due adverse interactions with the perovskite material. Other metals, such as aluminium (Al) and molybdenum (Mo), exhibit comparatively high current densities, falling within the range of values between these extremes. The device achieves optimal performance by utilizing Ag (Silver) with a work function of $4.2eV$ as the back contact. The photovoltaic cell efficiency is 32.68%, the V_{oc} is $0.92V$, the J_{sc} is $46.31\frac{mA}{cm^2}$, and the FF is 76.66%.

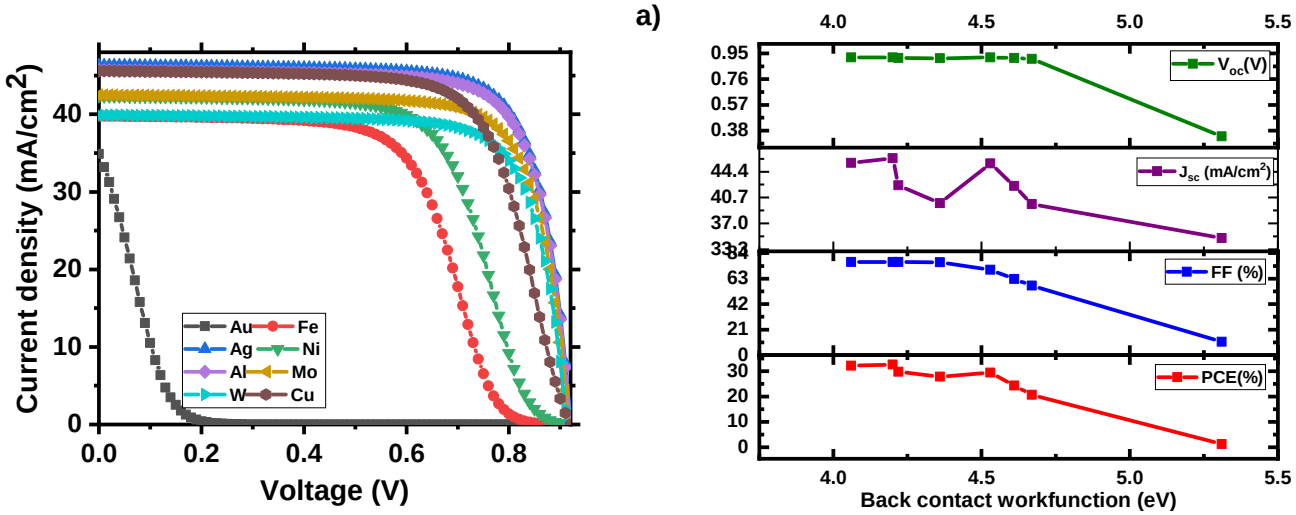

(a) Effect of Work function of back contact on the J-V curve.

(b) Effect of Work function of back contact on the output characteristics.

Figure IV.12: a) Effect of Work function of back contact on the J-V curve. b) Effect of Work function of back contact on the output characteristics.

IV.2.2.8 Effect of antireflective layer

It is known that to minimise the amount of reflected light, a common technique involves coating the surface of the solar cell with an anti-reflection material, either in one or several layers. The anti-reflection layer is very important for improving the efficiency of solar cell conversion because it makes it easier for light to focus on the device's active material. The anti-reflection layer typically consists of either one or several dielectric layers. This layer reduces light reflection, enhancing light penetration and improving visibility and legibility in different lighting circumstances [121].

Figured out in Figure IV.13 is the effect of several anti-reflective (AR) coatings on the solar cell's J-V characteristic. The AR layers are made up of four different types of materials: SiO_2,SiN, Si_3N_4, and Al_2O_3. Figure IV.13 and Table IV.6 indicate that SiO_2 yielded the most favourable outputs, while Al_2O_3 produced the least favourable results. This phenomenon arose due to the better transparent properties of the SiO2 materials compared to that of the Al_2O_3 substance. The overall efficiency of the perovskite solar cell is significantly affected by the presence or absence of this layer.

Table IV.6: Solar cell output values for different anireflective layer.

Anireflective layer	*PCE*	*FF*	J_{sc}	V_{oc}
SiO_2	32.68	76.66	546.31	0.92
SiN	29.89	76.6	41.61	0.92
Al_2O_3	22.65	76.39	32.87	0.90
Si_3N_4	29.89	76.6	42.61	0.92

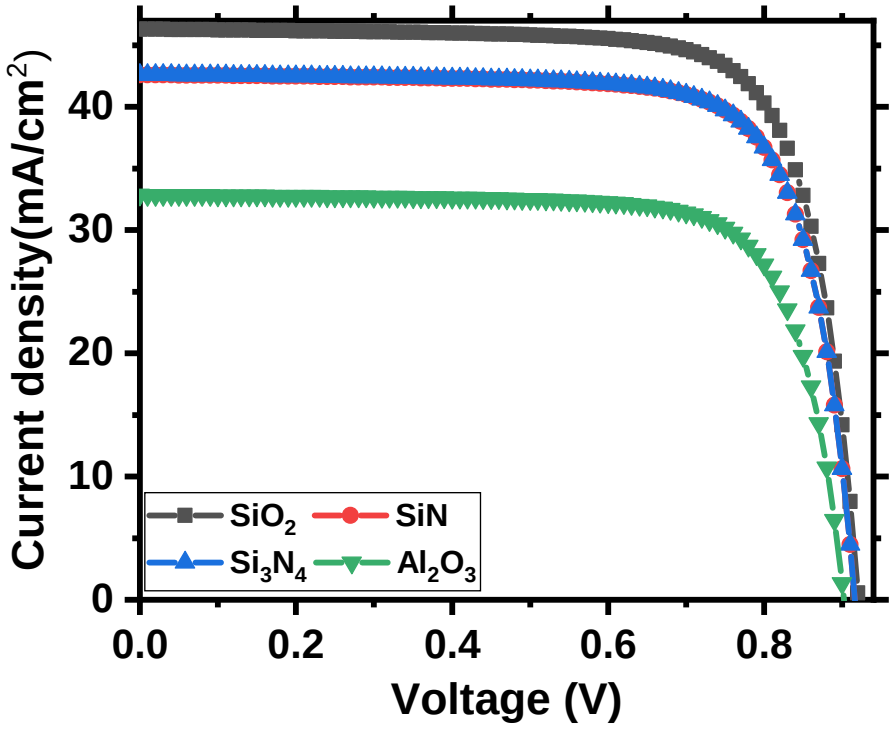

Figure IV.13: effect of the antireflective layer on the J-V characteristic of the solar cell.

Effect of the antireflective layer thickness (SiO_2)

The anti-reflection layer in Figure IV.14 is assumed to be SiO_2, with its thickness varying from 0.05 μm to 0.5 μm. The result on J-V characteristic and electrical outputs is shown Figure IV.14. According to these figures, the thickness of the SiO_2 layer in a solar cell has minimal impact on its performance. As the thickness of the SiO_2 layer increases, the four parameters remain unchanged, suggesting that the efficiency of the solar cell is not affected by the thickness of the SiO_2 layer. The same remark hold for the current density-voltage characteristics as the SiO_2 thickness increases. This is attributed to the characteristics of the SiO_2 layer, such as its ability to prevent undesired reactions, alter the electric field, and reduce the loss of charge carriers, play a key role in maintaining solar cells' consistent performance, independent of the SiO_2 layer's thickness.

IV.2.2.9 Comparison between the inverted and conventional structure

Double perovskite solar cells with normal and inverted designs are shown in Figure IV.15. The conventional configuration has a PCE of 30.86%, a FF of 77.03%, a J_{sc} of 43.47 $\frac{mA}{cm^2}$, and V_{oc} of 0.92 V. The inverted structure demonstrates enhanced performance, achieving a PCE of 32.86%, a slightly reduced fill factor FF of 76.66%, an increased J_{sc} of 46.30 $\frac{mA}{cm^2}$, and the same V_{oc} of 0.92 V. The comparison suggests that the inverted configuration of perovskite solar cells has the potential to achieve higher energy conversion efficiency compared to the

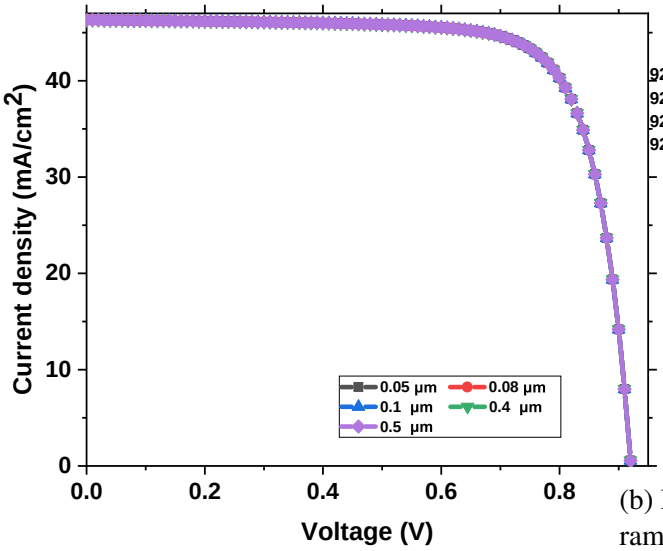

(a) Effect of SiO_2 thickness on the J-V curve.

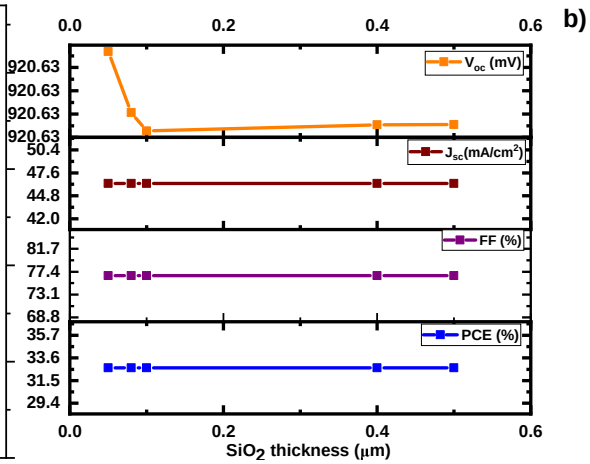

(b) Effect of SiO_2 thickness on the output parameters.

Figure IV.14: a) Effect of SiO_2 thickness on the J-V curve. b) Effect of SiO_2 thickness on the output parameters.

normal configuration. Nevertheless, it is crucial to acknowledge that these outcomes represent only a single set of data, and the real performance may differ due to several factors such as fabrication techniques, material integrity, and operational circumstances. The selection between a normal or inverted configuration can have a significant impact on the efficiency of the solar cell. Based on the presented figure, the inverted structure demonstrates enhanced performance characterized by a better PCE and J_{sc}, despite a slightly lower FF. However, it's important to note that the performance can vary based on a variety of factors, including the specific materials used for the ETL and HTL, the quality of the perovskite layer, the fabrication methods, and the operating conditions. Research showed that the normal structure can be improved to attain a PCE score close to that of the inverted p-i-n structure. This suggests that both structures have their advantages and can be optimized for high performance.

IV.3 Part 2: Exploring Gallium Oxide's functions in advancing the efficiency of $CH_3NH_3PbI_3$ perovskite solar cells: electron transport, transparency Enhancement, UV and hole Blocking.

This section delves into the study of perovskite solar cells that incorporate a Cu_2O/Si bilayer hole transporting layer (bi-HTL) with beta-gallium oxide (β-Ga_2O_3) ETL as an UV blocking layer and window. Several advantages can be gained from using (β-Ga_2O_3) as ETL instead of

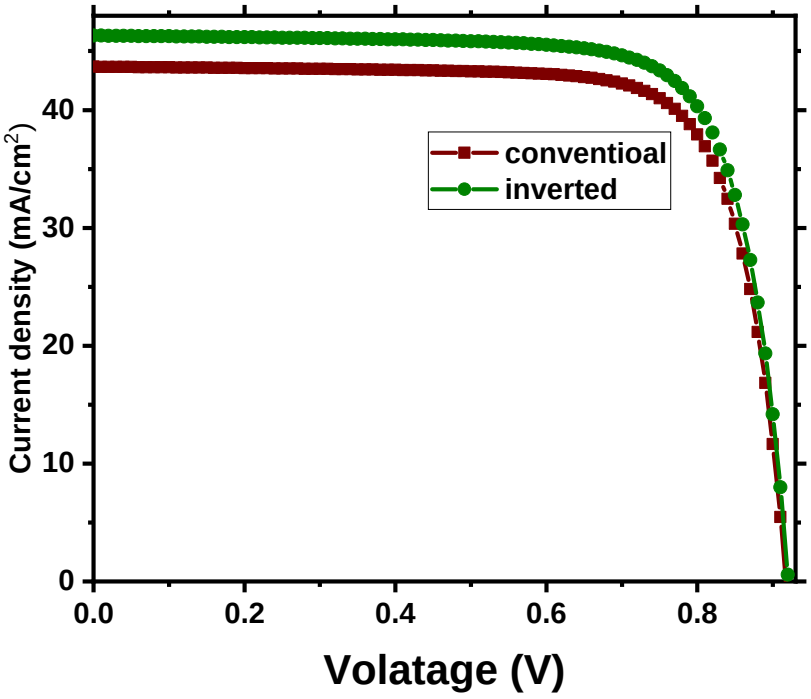

Figure IV.15: J-V curve comparison between conventional structure and inverted structure.

zinc oxide (ZnO), according to the study.(β-Ga_2O_3) serves as a more effective ETL, enhancing electron mobility in the solar cell and resulting in a higher (PCE). Numerical calculations conducted with SILVACO-TCAD software forecast a substantial increase in (PCE), with the refined device setup achieving an impressive 23.02%, surpassing traditional ZnO-based cells. The enhancement stems from the improved electrical characteristics of (β-Ga_2O_3), such as its broader bandgap and increased electron mobility.

Additionally, (β-Ga_2O_3) functions as a transparent material, enabling increased sunlight absorption for energy generation in the cell. This is accomplished by its great transparency in the visible light spectrum, which reduces reflection losses. Crucially, (β-Ga_2O_3) also has the distinct capability to absorb detrimental ultraviolet (UV) light. UV radiation can significantly deteriorate perovskite solar cells' efficiency and reliability. The study tackles a significant difficulty in perovskite technology by integrating (β-Ga_2O_3), which could result in solar cells that are more durable and dependable.

Furthermore, the work investigates the utilization of a bilayer consisting of cuprous oxide (Cu_2O) and p-type silicon (p-Si) as the hole transport and electron blocking layer (HTL), respectively. This combination efficiently removes holes created in the perovskite layer and prevents undesired electron flow back into the absorber. Adding Cu2O/p-Si enhances the overall efficiency and brings the device closer to the theoretical limit of 26.6% PCE known as the Shockley-Queisser limit.

IV.3.1 Solar cell structure

The lead-based perovskite solar cell shown in Figure IV.16 consists of the following elements: the bilayer hole transport layer Cu_2O/Si, the perovskite absorbing material $CH_3NH_3PbI_3$, and the electron transport layers (ETL) (β-Ga_2O_3). The values that were used for the numerical evaluation can be found in tables IV.7 and IV.8.

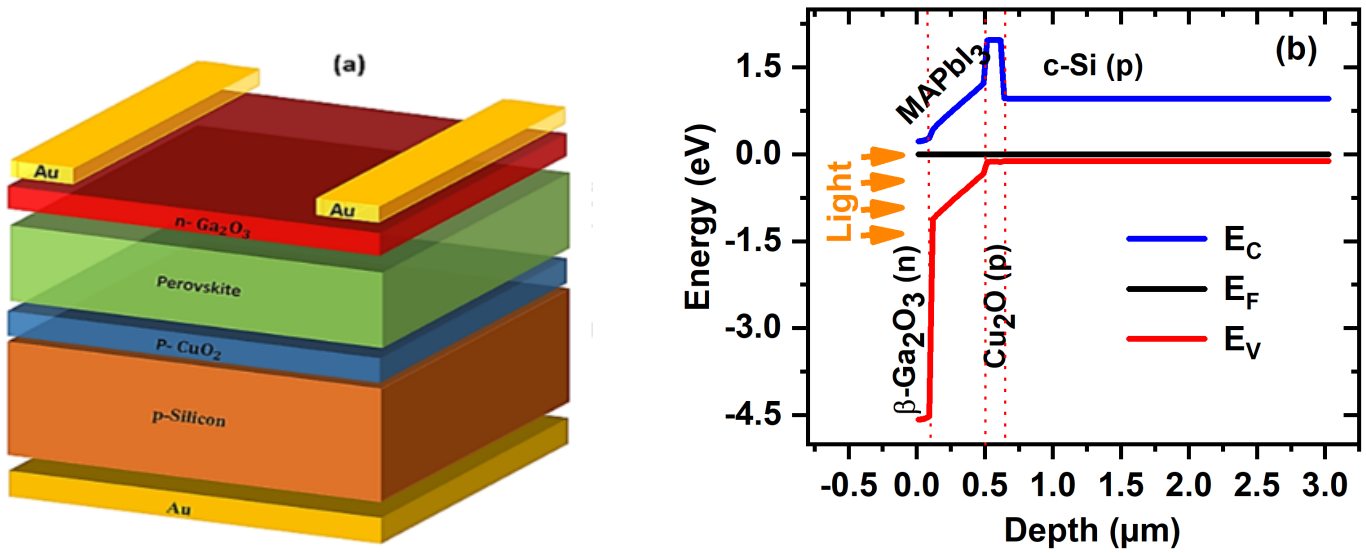

(a) Bi-HTL perovskite solar cell's structure.

(b) thermal equilibrium energy band diagram.

Figure IV.16: a) Bi-HTL perovskite solar cell's structure. b) thermal equilibrium energy band diagram.

Table IV.7: solar cell output values for different anireflective layer [122–125].

Parameters	CH_3NHPbI_3	β-Ga_2O_3	Cu_2O	Si
Band gap (eV)	1.55	4.8	2.17	1.12
Affinity (eV)	3.9	4	3.20	4.17
Hole mobility $\left(cm^2 \cdot V^{-1} \cdot s^{-1}\right)$	2	10	80	480
Electron mobility $\left(cm^2 \cdot V^{-1} \cdot s^{-1}\right)$	2	300	200	1500
Relative permittivity	6.5	11	7.11	11.8
$N_c(cm^{-3})$	$2.2 \cdot 10^{18}$	$3.7 \cdot 10^{18}$	$2.02 \cdot 10^{17}$	$2 \cdot 10^{19}$
$N_v(cm^{-3})$	$1.8 \cdot 10^{19}$	$5 \cdot 10^{18}$	$1.10 \cdot 10^{19}$	$1.04 \cdot 10^{19}$
Free electrons concentration (cm^{-3})	-	$3 \cdot 10^{16}$	-	-
Free holes concentration (cm^{-3})	-	-	$1 \cdot 10^{16}$	-
τ_n/τ_p (ns)	8/8	1/1	5/5	$1 \cdot 10^{-4}/1 \cdot 10^{-4}$
AUGN $\left(cm^{-6} \cdot s^{-1}\right)$	$1 \cdot 10^{-22}$	$1 \cdot 10^{-22}$	$1 \cdot 10^{-22}$	-
AUGP $\left(cm^{-6} \cdot s^{-1}\right)$	$1 \cdot 10^{-22}$	$1 \cdot 10^{-22}$	$1 \cdot 10^{-22}$	$1 \cdot 10^{-22}$
A.langevin	1	-	-	-
Thickness	0.35	0.1	0.05	10

Table IV.8: Traps Associated with Perovskite, Cu_2O and β-Ga_2O_3 [126–129].

Material	Trap level	Density	Electron capture cross section	Hole capture cross section
Perovskite	0.62	$5 \cdot 10^{14}$	$5.2 \cdot 10^{-14}$	$5.2 \cdot 10^{-14}$
	0.76	$9.5 \cdot 10^{14}$	$2.5 \cdot 10^{-14}$	$2.5 \cdot 10^{-14}$
Cu_2O	0.45	$5 \cdot 10^{14}$	$1 \cdot 10^{-15}$	$1 \cdot 10^{-14}$
β-Ga_2O_3	0.6	$3.6 \cdot 10^{1}3$	$4.5 \cdot 10^{-}11$	$5.4 \cdot 10^{-}13$
	0.75	$4.6 \cdot 10^{1}3$	$0.5 \cdot 10^{-12}$	$0.5 \cdot 10^{-14}$
	1.05	$1.1 \cdot 10^{14}$	$1.5 \cdot 10^{-12}$	$1.5 \cdot 10^{-14}$

IV.3.2 Choice of β-Ga_2O_3 as electron transport layer

Although ZnO is a promising ETL due to its low processing temperature, scientists are continuously seeking new ways to enhance the reliability and efficiency of perovskite solar cells. At this point, ZnO and β-Ga_2O_3 3were compared. Figure IV.17a displayed the current density voltage (J-V) characteristic of the simulated perovskite ($MAPbI_3$) solar cell, whereas Figure IV.17b displayed the external quantum efficiency (EQE). The figures compare β-Ga_2O_3 and ZnO as ETLs. The results show that β-Ga_2O_3 material is more effective than ZnO. For β-Ga_2O_3, (PCE), (FF),(J_{sc}), (V_{oc}), are, in that order, 66.44%, 19.21%, and 30.90 $\frac{mA}{cm^2}$ and 935.79 mV, respectively. On the other hand, for ZnO, the values for J_{sc}, V_{oc}, FF, and PCE are 29.93 $mA \setminus cm^2$, 911.80 mV, 59.80%, and 16.32% correspondingly.

The reason why β-Ga_2O_3 is superior to ZnO is because it increases solar cell absorption, as confirmed by EQE (Figure IV.17b). The likely reason for this enhancement is the ultra-wide bandgap semiconductor capabilities of β-Ga_2O_3, which lead to the perovskite absorption wavelength domain expanding and the outstanding optical window layer features. The adequate band alignment of the β-Ga_2O_3 and the perovskite is another element that improves the perovskite solar cell's capability. It should be mentioned that β-Ga_2O_3 has the ability to absorb photons with energies more than or equal to $4.8eV$, which means it might be used as a UV absorption layer to safeguard the perovskite.

IV.3.3 Selecting Cu_2O/Si Bilayer for hole extraction and electron barrier

We are presently conducting an examination to confirm the effect of Cu_2O in improving the ability to extract holes and block electrons. Remarkably, the solar cell's output characteristics are superior when a dual layer of Cu_2O/Si is used compared to a single Si layer. This setup results in an enhanced (J_{SC}) of 30.90 $mA \setminus cm^2$, an increased (V_{OC}) of 935.79mV, a higher (FF) of 66.44%, and a greater (PCE) of 19.21%. The Si HTL with a single layer demonstrates somewhat lower values, as depicted in Figure IV.18. The dual layer's improved hole extraction and electron blocking features are the source of these noticeable benefits.

While it is difficult to produce pure Cu_2O without any CuO, recent progress in materials

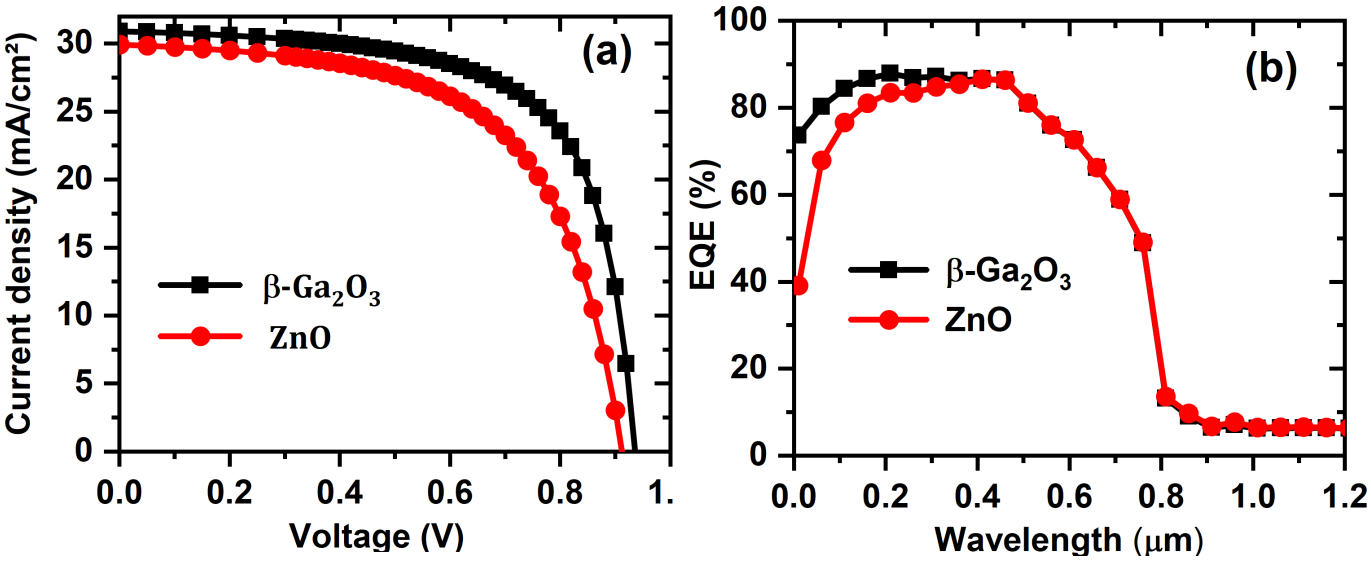

(a) Current-Voltage (J-V) characteristics.

(b) External Quantum Efficiency (EQE).

Figure IV.17: a) Current-Voltage (J-V) characteristics and b) External Quantum Efficiency (EQE) of perovskite-based solar cells using β-Ga_2O_3 and ZnO as electron transport layers (ETL).

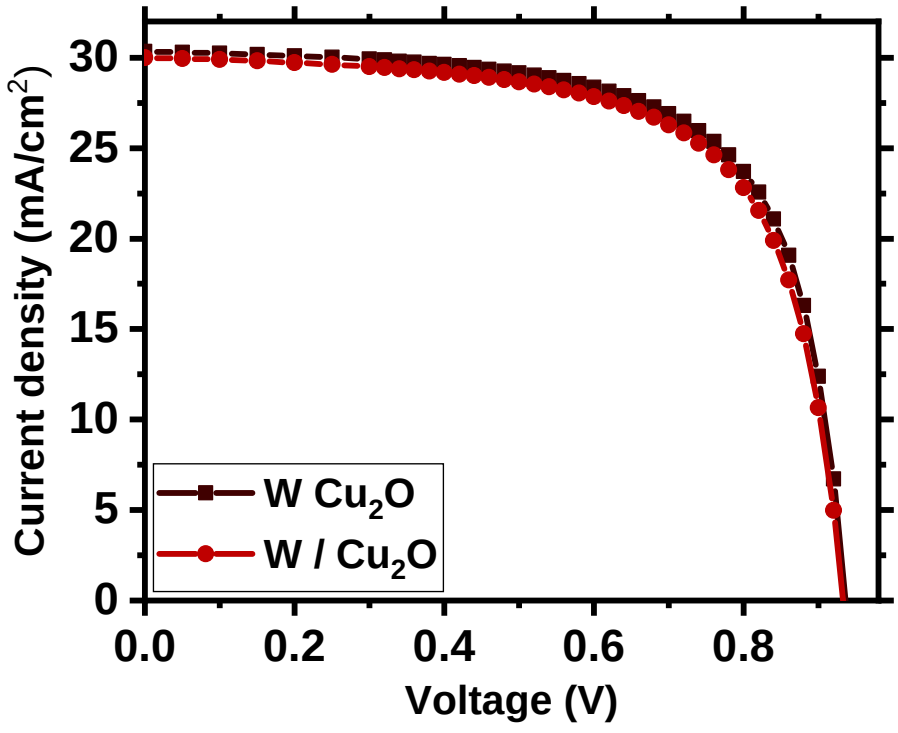

Figure IV.18: J-V characteristics with and without Cu_2O layer.

synthesis has shown encouraging outcomes in achieving pure Cu_2O without including any other phases. Even in an outside environment, Nguyen et al. were able to build a layer of pure Cu_2O onto silicon using a low-temperature deposition process., by utilizing the Atmospheric Pressure-

Spatial Atomic Layer Deposition approach [130].

IV.3.4 Perovskite and β-Ga_2O_3 thickness effect

In the field of solar cell technology, the thickness of various layers particularly the absorber layer has a substantial impact on the functionality of solar cells. In light of this, we conducted a study to analyse the consequences of varying the β-Ga_2O_3 ETL layer thickness from 0.05 μm to 0.5 μm, as well as the perovskite layer thickness from 0.25 μm to 0.5 μm. Figure IV.20 displays the (J-V) characteristics and the EQE as they vary with the thickness of β-Ga_2O_3, presenting our research findings. Moreover, Figure IV.21 displays the electrical outputs that were recovered from these tests. In order to provide a thorough examination, we have included Figure IV.21 and IV.22, which illustrate the identical electrical characteristics when graphed against the perovskite thicknesses.

Upon thorough analysis, we have concluded that the most favorable thickness for the β-Ga_2O_3 electron transport layer (ETL) is 0.1 μm, but for the perovskite absorber layer (AL) it is 0.35 μm. Noteworthy, the solar cell's performance declined with increasing β-Ga_2O_3 layer thickness. The increase in device series resistance and the decrease in light absorption by the perovskite layer, as seen in Figure IV.19b, can be related to this phenomenon. As a result, our investigations revealed that by using an ideal thickness of 0.1 μm for the β-Ga_2O_3 ETL, we can get an efficiency of 19.26%.

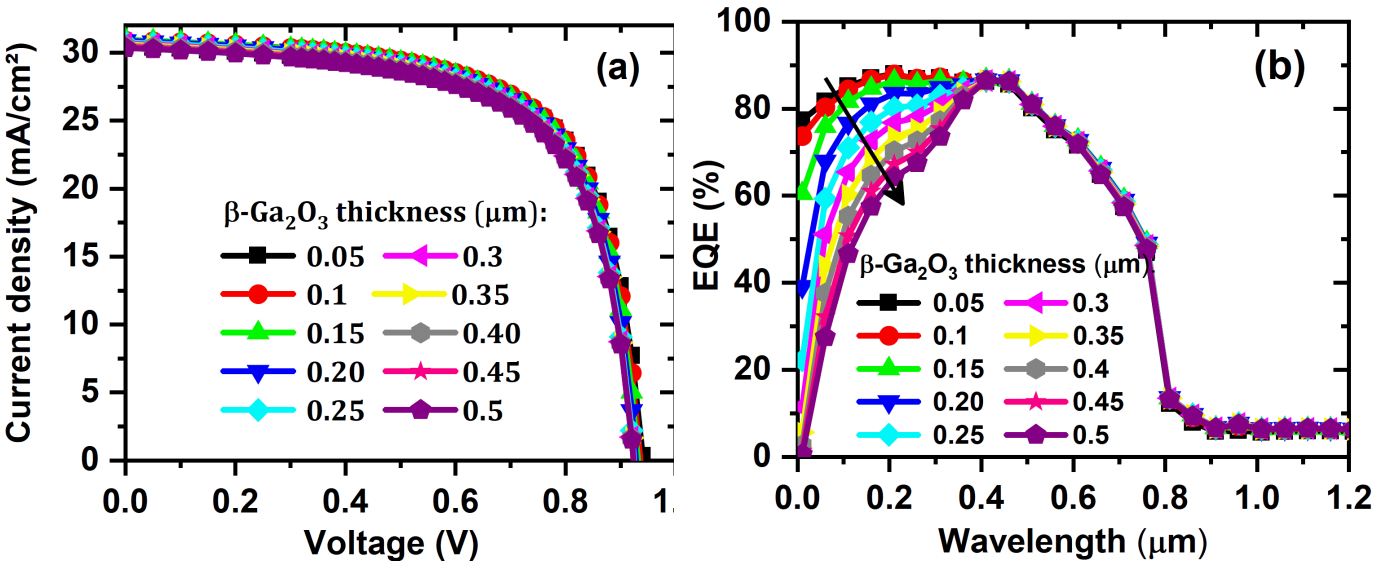

(a) Current-Voltage Behavior.

(b) External Quantum Efficiency.

Figure IV.19: a) Current-Voltage Behavior and b) External Quantum Efficiency of perovskite solar cells across varying thicknesses of the β-Ga_2O_3 Layer.

By increasing the perovskite layer thickness, the output properties have been improved. As an illustration, the following parameters are displayed by the solar cell when the thickness of the perovskite layer is 0.35 μm: $V_{OC} = 0.94V$, $J_{SC} = 30.33mA \setminus cm^2$, $FF = 67.86\%$, and

$PCE = 19.27\%$. The improved efficiency can be due to the increased current density generated by the photons, that is associated with the thicker layer of the absorber. A greater thickness of the layer enables a higher number of carriers to be produced by absorbing light [131].

In addition, the most effective thickness for the absorber perovskite layer is 0.35 μm, leading to a maximum external quantum efficiency (EQE) of 85% between the wavelengths of $200 - 450$ nm. In a further investigation conducted by Fakhri et al [132]. comparable findings were observed. Solar cells demonstrated the greatest capacity to absorb light throughout the identical range of wavelengths, resulting in the best achievable EQE within this range. It is important to mention that the maximum wavelength for this thickness is anticipated to be 750 nm. When the wavelength goes beyond 800 nm, the absorption of low-energy photons causes a steep drop in absorption, which eventually drops to zero.

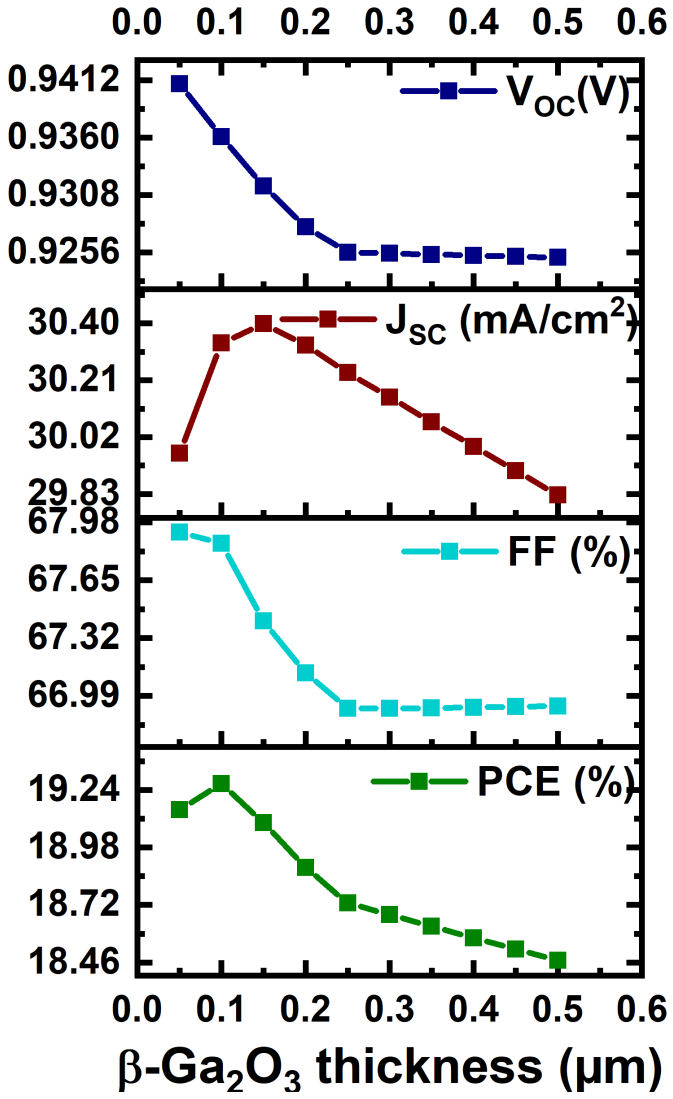

Figure IV.20: changes in solar cell parameters as the thickness ofβ-Ga_2O_3 is increased.

Regarding the electrical outputs, it has been noted that theV_{oc} drops substantially as the

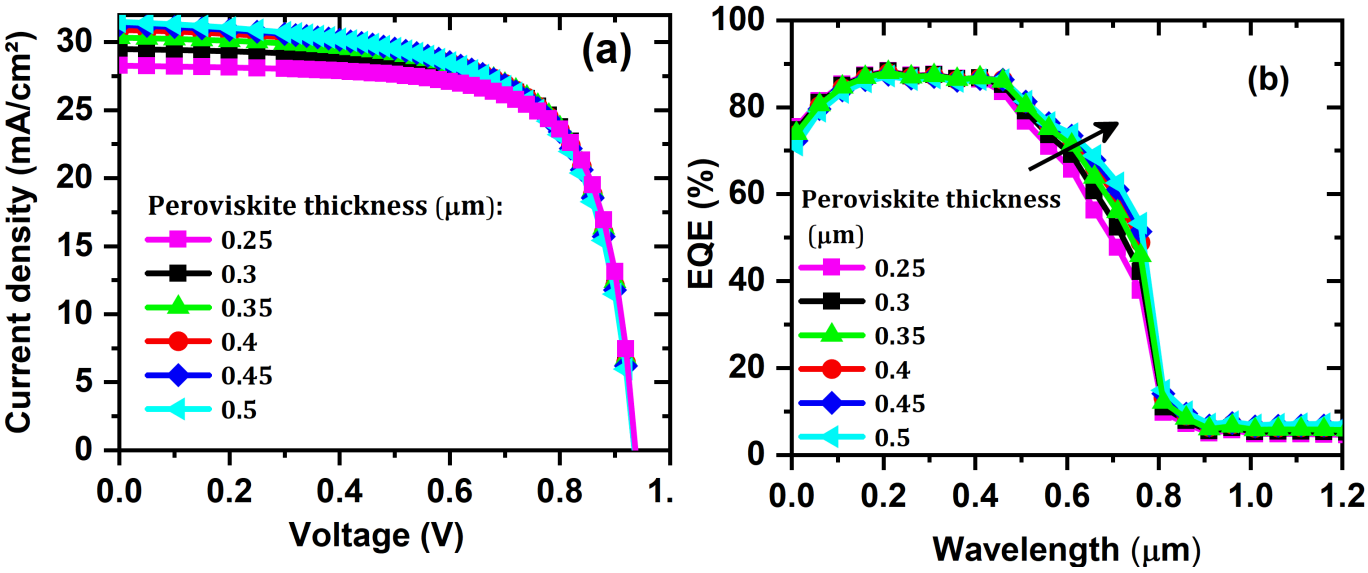

(a) Current-Voltage Behavior.

(b) External Quantum Efficiency.

Figure IV.21: Examination of a) Current-Voltage (J-V) behavior and b) External Quantum Efficiency (EQE) of perovskite solar Cell in correlation with perovskite layer thickness.

thickness of the β-Ga_2O_3 layer or the perovskite absorber is raised. Nevertheless, the decline in FF becomes more noticeable as the absorber layer increases. remarkably,J_{sc}acts in the exact opposite way in the second scenario as it did in the first.

IV.3.5 Influence of traps associated with perovskite material

Trap states in perovskite materials can significantly affect the efficiency and how long solar cells last. Perovskite films can have structural defects that cause trap states, which collect charge carriers generated by light, leading to energy losses and reduced efficiency. These imperfections are commonly located in close proximity to the surface or interfaces between grains in the film [133]. The deposition method and film production parameters can influence the nature and density of these flaws.

As stated by Mohd Yusoff et al [134], Two kinds of defects are typically seen in perovskite films: IPb, in which I atoms are placed at the MA position, and IMA, in which I atoms occupy a Pb site. The one-step spin-coating process produces perovskite films where the most common defects are IPb defects, which are found around $0.62eV$ below the conduction band (CB). In contrast, perovskite films produced by the sequential deposition technique exhibit a prominent deep defect known as IMA, that is situated about $0.76eV$ under the CB. The IMA defect state has a lower energy level within the bandgap than IPb, which results in a stronger influence on the film's electrical properties [126, 133].

Regarding the impact of IPb and theIMA trap density on the current-voltage (J-V) behaviour and output characteristics of perovskite solar cells are shown in Figures IV.23 and IV.24, respectively. The device's performance is obviously negatively impacted when there are defect states

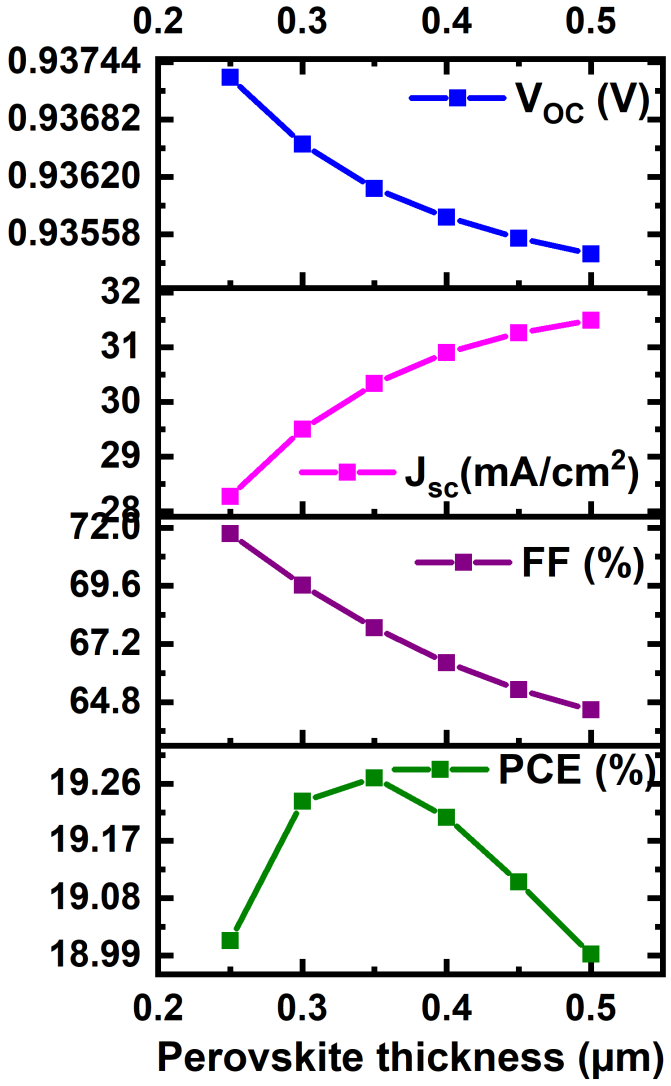

Figure IV.22: Solar cell parameters in relation to varying perovskite thickness.

in the absorber layer. The reason for this is that the absorber layer has a vital function in converting incoming light into electrical charge, and any flaws might capture and combine charge carriers, resulting in a decrease in efficiency. When the trap density of IPb grows from $10^{14} cm^{-3}$ to $10^{17} cm^{-3}$, the open-circuit voltage (V_{OC}) undergoes a significant lowering.

The second trap flaws reveal an IMA situated at an energy level of $0.75eV$. As a consequence, there is a reduction in the voltage open circuit (V_{OC}) from $0.95V$ to $0.78V$ and a decrease in the fill factor (FF) from 77.53% to 61.20%. Nevertheless, the value of J_{sc} remains almost unchanging at $30mA \setminus cm^2$ for trap densities lower than $10^{15} cm^{-3}$. However, the value of J_{sc} drops as trap densities increase. Remarkably, the *PCE* undergoes a substantial decline from 23.02% to 2.92% in these instances. In summary, the device's performance remains mostly unchanged as the perovskite layer's trap density is below $10^{15} cm^{-3}$.

Nevertheless, when the trap density exceeds $10^{15} cm^{-3}$, the device's performance experi-

ences a major deterioration, leading to a notable loss in efficiency. The findings indicate that decreasing the number of traps, particularly at energy levels of $0.62eV$ and $0.75eV$, greatly enhances PSCs accomplishment. Multiple techniques have been suggested to reduce trap density in the perovskite film. These include improving the processing conditions of the layers to improve the crystallinity of the film, as demonstrated by Ganesh et al [85] , Liu et al [135], Pegu et al [136], and Schütz et al [137]. Enhancing the quality of the crystal structure can significantly reduce the number of traps and lower the occurrence of charge recombination, triggering the device's functionality to improve generally.

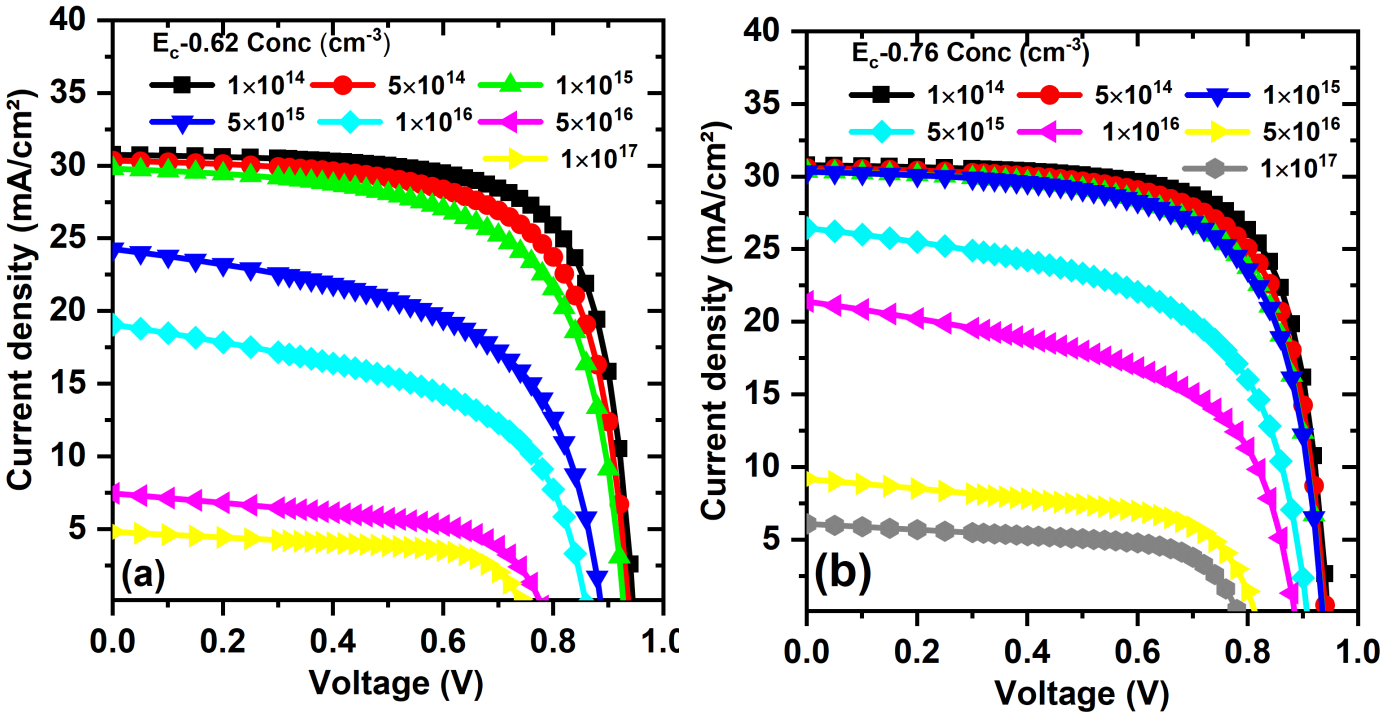

(a) $E_C - 0.62eV$.

(b) $E_C - 0.76eV$.

Figure IV.23: Influence of perovskite-associated trap state density on J-V characteristic of perovskite solar cell performance characteristics. specifically investigating energy levels at $E_C - 0.62eV$ and $E_C - 0.76eaV$.

IV.3.6 β-Ga_2O_3 related traps effect

The existence of β-Ga_2O_3associated defects in PSCs might potentially have a substantial impact on the efficiency of solar cells, and their abundance can be controlled by the processing conditions during fabrication. Grain boundaries, dislocations, and flaws at the perovskite-charge transport layer interface are the most probable sources of traps. Consequently, by regulating the processing parameters and enhancing the quality of both β-Ga_2O_3 and the perovskite layers, it is possible to decrease the trap density [136]. Galazka's research identified three separate traps in β-Ga_2O_3, positioned at $E_c - 0.6$, $E_c - 0.75$, and $E_c - 1.05eV$, respectively [129]. These traps

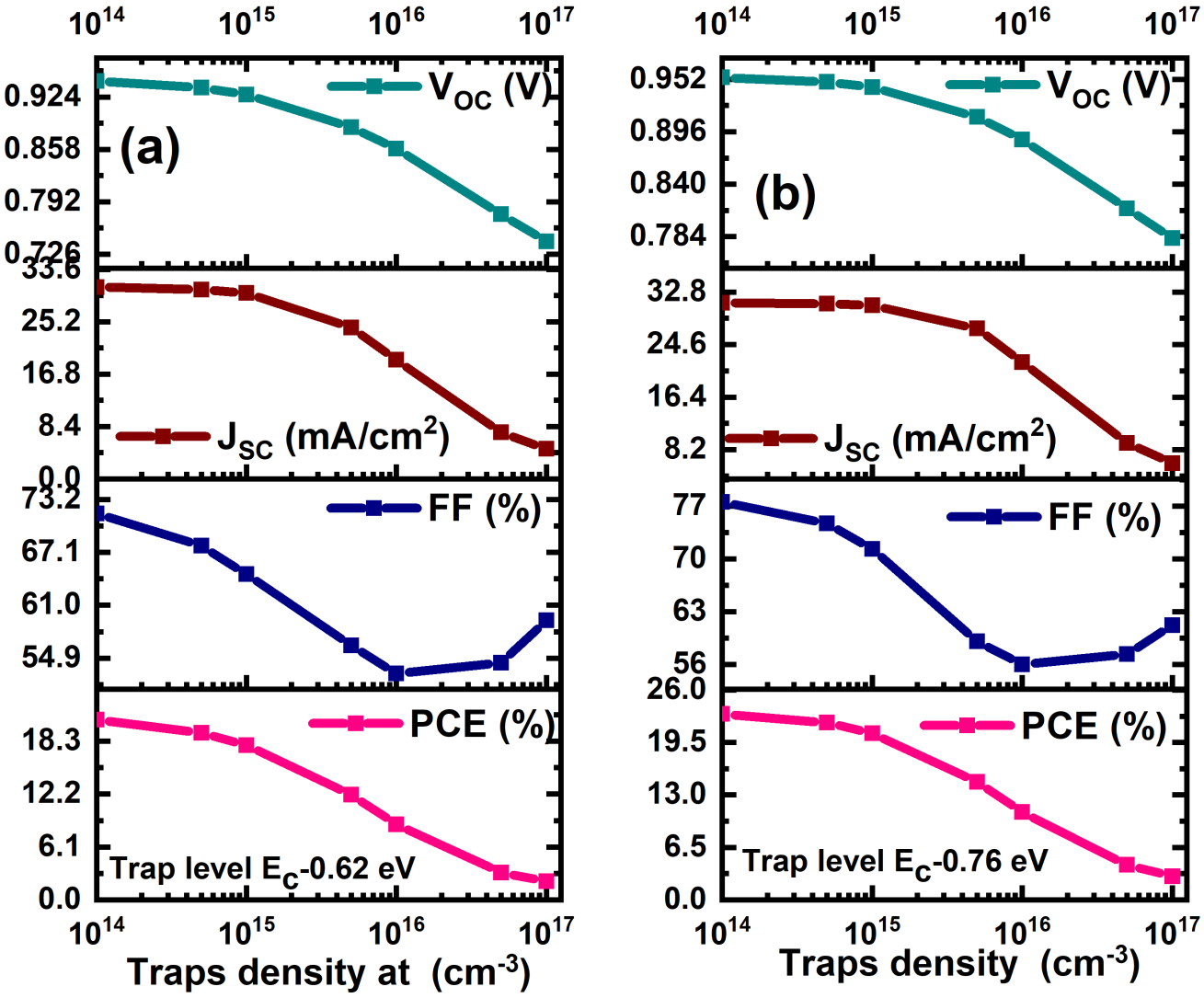

(a) $E_C - 0.62eV$.

(b) $E_C - 0.76eV$.

Figure IV.24: Effects of Perovskite-Associated Trap State Density on Performance Metrics of Perovskite Solar Cells. Focus on Energy Levels at $E_C - 0.62eV$ and $E_C - 0.76eV$.

are characterized by energy levels situated below E_c.

Regarding β-Ga_2O_3, Figures IV.25 and IV.26 show the J-V characteristic and the output parameters of the PSC when subjected to varying trap densities, ranging from 10^{14} to $10^{17} cm^{-3}$. The data clearly shows that higher β-Ga_2O_3 trap concentrations limit the efficiency of the solar cell. All output parameters demonstrate two different zones of change. The initial section displays a steady decrease, whereas the subsequent zone showcases a sudden decline. The threshold for the transition between these two behaviors occurs at roughly $5 \cdot 10^{15} cm^{-3}$ for all sorts of defects.

As the number of trap density located $0.6eV$ below Ec increases from $10^{14} cm^{-3}$ to $10^{17} cm^{-3}$, the open-circuit voltage (V_{OC}) decreases from $0.95V$ to $0.76V$ (at$10^{16} cm^{-3}$), and then slightly improves to $0.78V$ at $10^{17} cm^{-3}$. The short-circuit current density (J_{sc}) remains stable at around

$30mA/cm^2$ for trap densities below $5 \cdot 10^{15} cm^{-3}$, but it decreases significantly for larger trap densities. The FF undergoes a decline from 77.53% to 65% when the trap density reaches $5 \cdot 10^{15} cm^{-3}$, and thereafter decreases to 6.81% at a trap density of $10^{17} cm^{-3}$. Similarly, the PCE experiences a decrease from 23.02% to 0.09%, with an intermediate value of 16.84% at a concentration of $5 \cdot 10^{15} cm^{-3}$.

Concerning the second trap defect, which is positioned $0.75eV$ below E_c, it seems that V_{OC} exhibits a lower level of sensitivity compared to the prior trap. More precisely, the open-circuit voltage (V_{OC}) decreases from $0.95V$ volts to $0.88V$ at a concentration of $10^{17} cm^{-3}$. Regarding J_{sc}, it maintains a relatively stable value of approximately $30mA/cm^2$, except when dealing with trap densities below $10^{16} cm^{-3}$, in which case it experiences a notable decrease. FF and PCE exhibit comparable traits to the prior defect, with the threshold of $5 \cdot 10^{15} cm^{-3}$ still delineating the distinction between areas of progressive and rapid changes. The percentages decrease from 77.53% and 23.02% to 10.52% and 0.29%, respectively.

Now let's discuss the third trap defect, which is located at a depth of $1.05eV$ below E_c. This trap has a similar effect to the second trap. The current density (J_{sc}) remains reasonably constant at approximately $30mA/cm^2$ when the trap densities are below $10^{16} cm^{-3}$. However, it significantly decreases for trap densities that are higher than this threshold. The values of FF and PCE decrease from 77.53% and 23.02% to 9.96% and 0.22%, respectively, when the threshold of $5 \cdot 10^{15} cm^{-3}$ is reached. This threshold marks the point at which the changes shift from being gradual to being more significant. Nevertheless, the open-circuit voltage (V_{OC}) exhibits a small improvement, increasing from $0.86V$ at a concentration of $10^{16} cm^{-3}$ to $0.87V$ at a concentration of $10^{17} cm^{-3}$. Therefore, it is essential to minimize trap density in order to achieve optimal performance results. To do this, one can optimize the doping of the electron transport material (ETM) to create a uniform and level surface, which will improve the interaction between the ETM and the active layer [136].

IV.3.7 Impact of traps associated with Cu_2O

Since HTL (Cu_2O) quality evaluations can include undesired defect traps, they substantially impact hole extraction efficiency. The HTL contains a principal trap located $0.45eV$ above the valence band, as mentioned by Hossain et al [127]. In order to undertake a more in-depth investigation, simulations were carried out using different densities of this trap.

Figure IV.27 displays the J-V properties of the perovskite solar cell. Significantly, this specific trap has a somewhat smaller impact compared to the traps in the β-Ga_2O_3 layer. This disparity can be ascribed to two sources. Initially, there is a greater quantity of photo-generated carriers at the interface between β-Ga_2O_3 and perovskite, as opposed to the interface between perovskite and Cu_2O. Furthermore, the traps present in β-Ga_2O_3 exhibit a higher level of effectiveness in collecting free carriers, as evidenced by their notably larger capture cross sections.

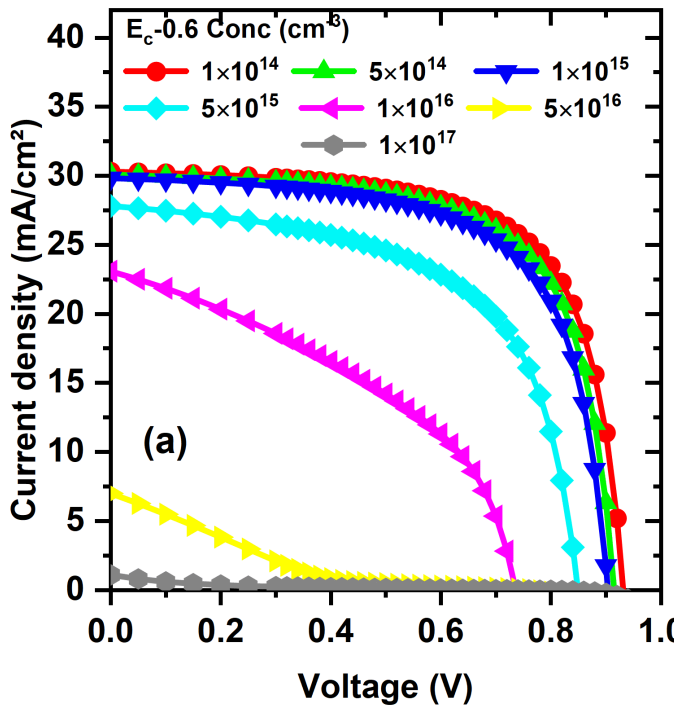

(a) $E_c - 0.6eV$.

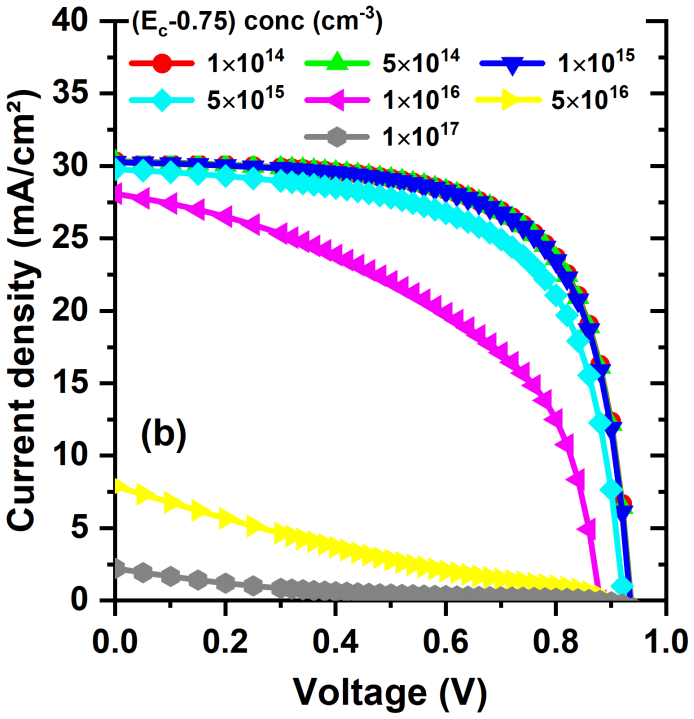

(b) $E_c - o.75eV$.

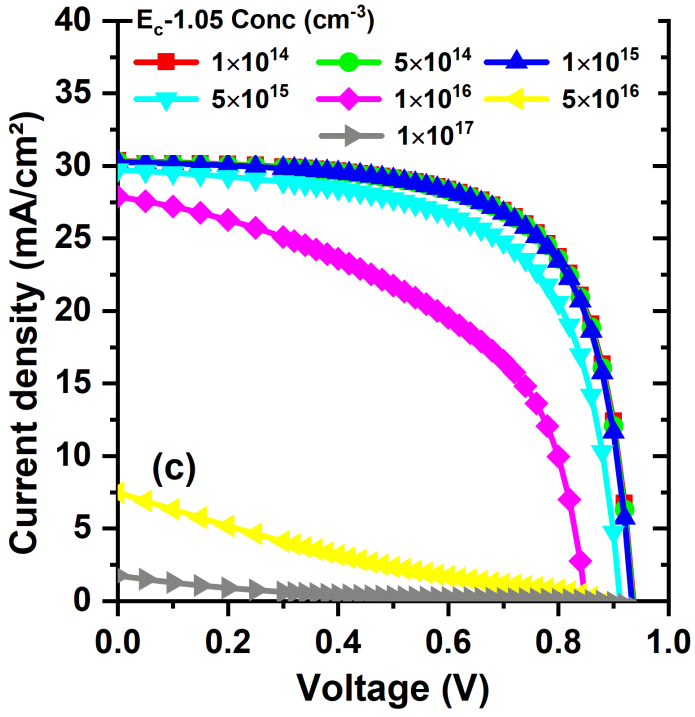

(c) $E_c - 1.05eV$.

Figure IV.25: Effect of Trap Densities Associated with β-Ga_2O_3 on the Current-Voltage (J-V) Behavior of Perovskite Solar Cells at Energy Levels of (a) $E_c - 0.6eV$, (b) $E_c - o.75eV$, and (c) $E_c - 1.05eV$.

IV.3.8 Temperature effect

Temperature variations can have a large impact on how well the perovskite solar cell works. In order to evaluate the influence, the temperature was manipulated within the range of $300 - 400K$

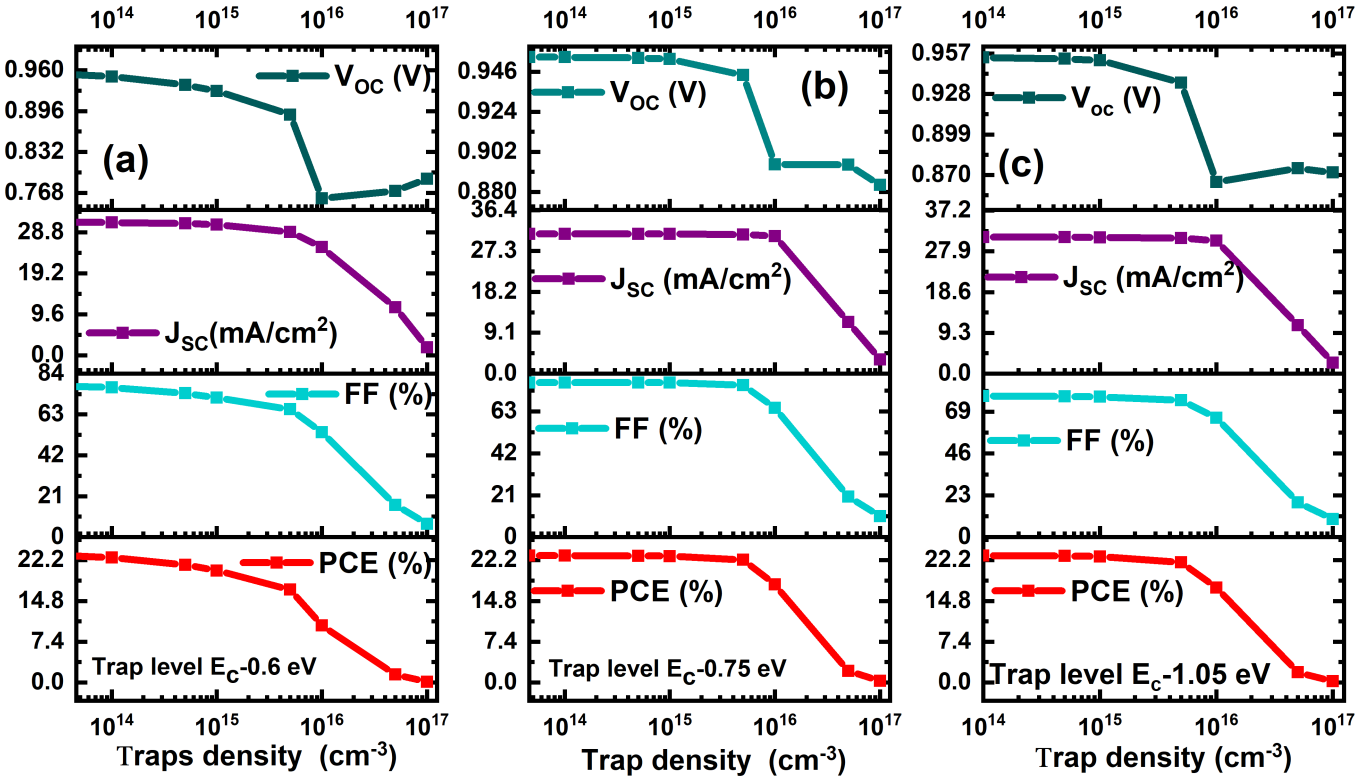

(a) $E_c - 0.6eV$. (b) $E_c - o.75eV$. (c) $E_c - 1.05eV$.

Figure IV.26: Impact of the density of β-Ga_2O_3 related traps on the output parameters of the perovskite solar cell at three different electrode potentials: $E_c - 0.6eV$, $E_c - o.75eV$, and $E_c - 1.05eV$.

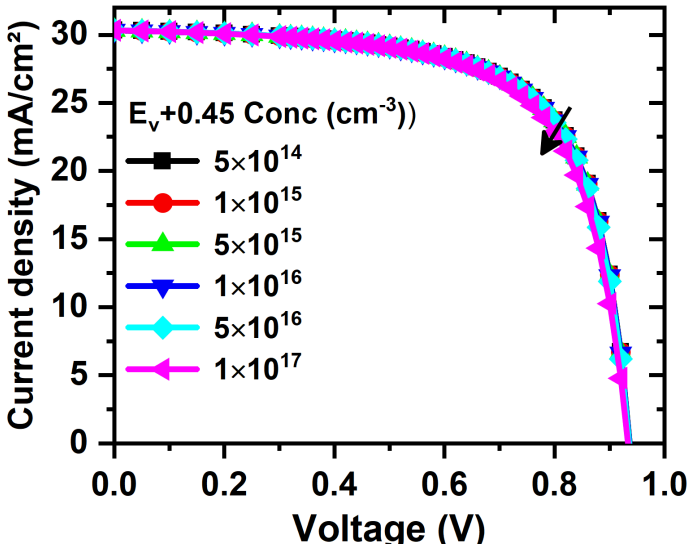

Figure IV.27: Current-Voltage (J-V) characteristics of the perovskite solar Cell with varied Cu_2O-related trap densities at $(E_V + 0.45eV)$.

for the purpose of investigating how it influences the solar cell's output parameters. Figures IV.28a and IV.28b depict the J-V characteristic and the recombination rate, respectively, demon-

strating the impact of operation temperature on the perovskite solar cell.

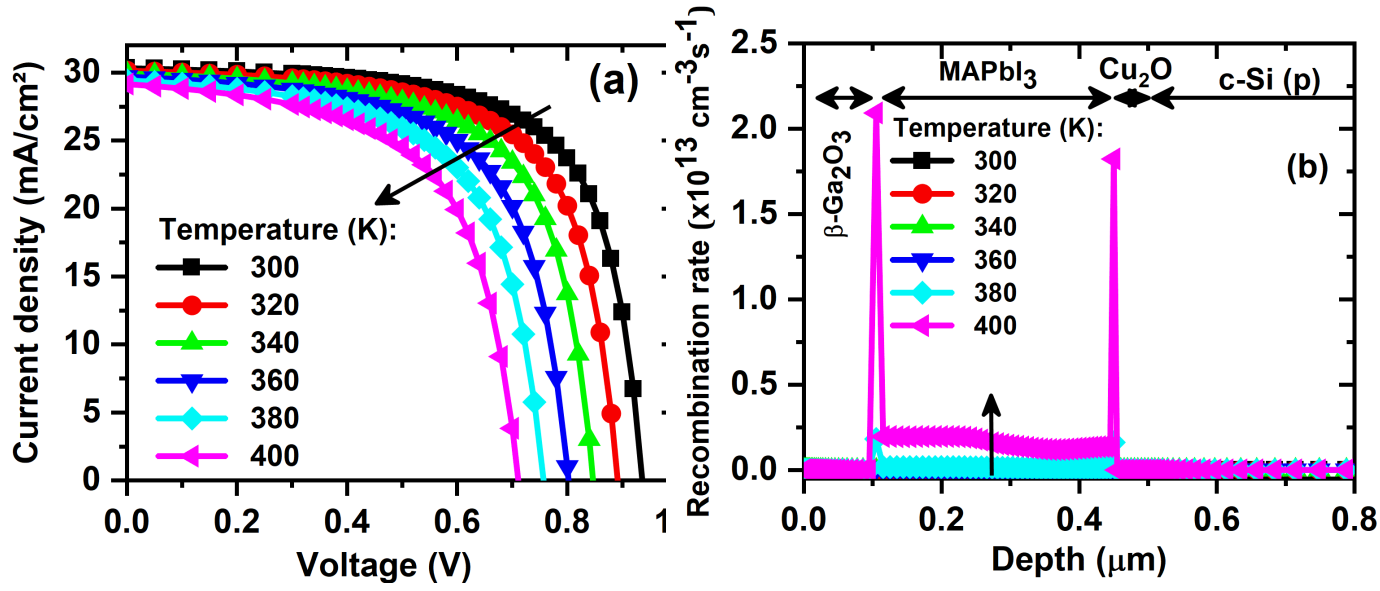

(a) Current-Voltage (J-V) Characteristics .

(b) recombination rate.

Figure IV.28: (a) Current-Voltage (J-V) Characteristics and (b) recombination rate in the perovskite solar cell, investigating the effect of operating temperature.

Figure IV.29 shows how the perovskite solar cell's output characteristics are affected by the operating temperature. A number of properties, such as carrier concentration, carrier mobility, resistivity, and bandgap, are altered when materials are subjected to rising temperatures. As a result, the output parameters are affected by this modification. The characteristics encompass (J_{SC}), (PCE), (V_{OC}), and (FF). The temperature increase causes additional strain and distortion in the material, resulting in a higher occurrence of interfacial defects and an accelerated rate of Shockley-Read-Hall (SRH) recombination. Because of this, the series resistance increases and the diffusion length decreases, ultimately causing a loss in the power conversion efficiency (PCE) and fill factor (FF). Furthermore, electron instability at higher solar cell temperatures causes more recombination and a decline power conversion efficiency (PCE) [138]. Optimal performance is generally achieved by selecting a working temperature of 300 K, taking into account these considerations [139]. It must be emphasised that the impacts mentioned might vary depending on the specific solar cell materials and configuration. Hence, meticulous evaluation of temperature impacts is crucial for the development of beneficial and dependable solar cells.

IV.3.9 Effect of Biomolecular recombination rate (A. Langevin):

Electrons and holes recombining in the conduction band and valence band is a major semiconductor physics phenomenon. Langevin's hypothesis has provided a clear explanation for this process, which is widely acknowledged as a crucial mechanism for recombination. Recent empirical study shows that charge carrier bimolecular recombination dominates the perovskite active layer [140]. The Langevin recombination rate can be defined as follows:

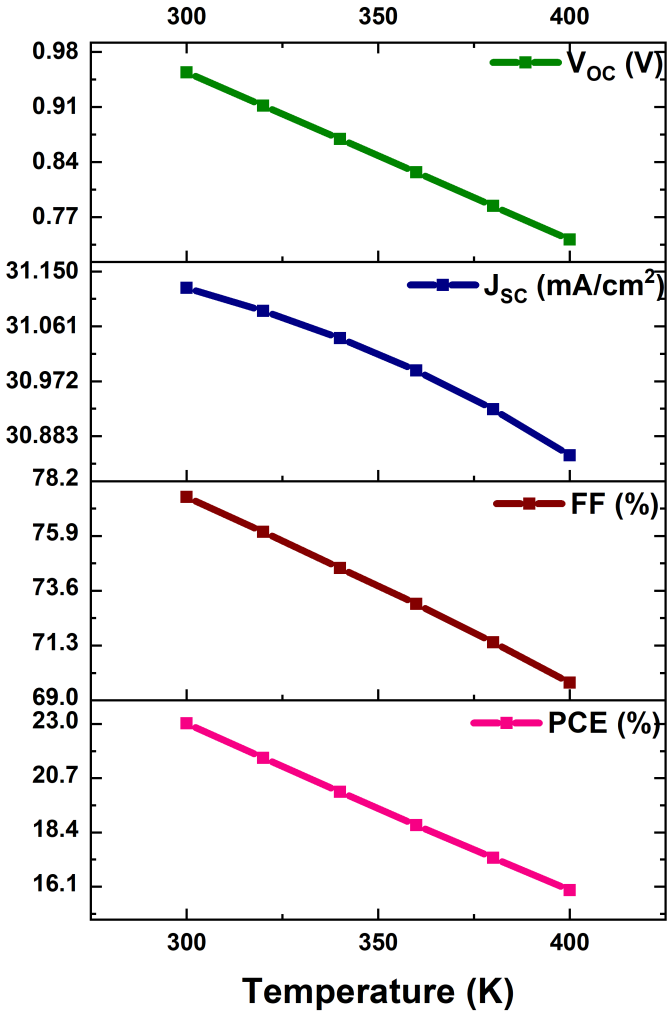

Figure IV.29: the effect of the operational temperature on the output parameters associated with perovskite solar cells.

$$R_{In,p} = r_L(x,y,t)\left(np - n_i^2\right) \tag{IV.1}$$

Where

$$r_L(x,y,t) = A_L \frac{q\left(\mu_n(E) + \mu_p(E)\right)}{\varepsilon_r \varepsilon_0} \tag{IV.2}$$

The electron (hole) density, denoted as $n(p)$, and the intrinsic charge carrier density, referred to as ni, play a crucial role in this context. Additionally, we consider $r_L(x,y,t)$ as the Langevin's recombination coefficient, ε_r as the relative permittivity, and ε_0 as the absolute permittivity. It should be mentioned that the bimolecular Langevin recombination model incorporates a prefactor, which is defined asA_L. This variable is essential in determining the effectiveness of charge carrier recombination. Setting A_L to 1 indicates that the model expects a conventional recombination rate. Through expanding the value of A_L to 10, the model anticipates a higher recom-

bination rate, notably a higher rate of bimolecular recombination. This rise in AL indicates an increased probability of bimolecular recombination occurring.

By varying the value of A_L from 1 to 10 in the model, we can examine how bimolecular recombination affects perovskite solar cells' efficiency. If an increase A_L leads to a drop in efficiency, then suggests that bimolecular recombination is truly a constraining factor. Nevertheless, if increasing A_L has little or no effect on efficiency, it indicates that other parameters, such as trap-assisted recombination or charge extraction, have a more substantial influence on restricting the cell's performance [140].

Figure IV.30 depicts the outcomes parameters of a perovskite solar cell, such as (PCE), (FF), (J_{SC}), and $(V\mathrm{OC})$, as they vary with changes in theA_L parameter. The observed trend demonstrates a decline in all metrics as the value of A_L increases. This indicates that bimolecular recombination is a fundamental attribute of the absorber. The variation in A_L has a substantial influence on short-circuit current (J_{SC}), indicating that the process of bimolecular recombination plays a role in the creation and movement of electron-hole pairs in the solar cell. Moreover, the impact on V_{OC} is likewise substantial, indicating that the speed of bimolecular recombination affects V_{OC}. The decline in FF can be ascribed to the diminished efficacy of electron-hole pair transportation across the cell, leading to amplified recombination losses. Furthermore, there is a decrease of 1.41% in PCE when the AL goes from 1 to 10.

To summarize, Figure IV.30 unequivocally indicates the substantial influence of bimolecular recombination on the performance characteristics of a perovskite solar cell. These findings emphasize the crucial need of improving material characteristics and device design to reduce recombination losses and increase the overall efficiency of the solar cell. In addition, we have compared our results to current experimental and simulation references, clearly demonstrating the significant importance of our simulation as indicate.

Table IV.9: a comprehensive comparison between our meticulously designed solar cell and the experimental and simulated $CH_3NH_3PbI_3$ based solar cells that utilized various hole transport layers (HTLs) and electron transport layers (ETLs).

References	HTL	ETL	Efficiency
Xie et al [141]	NiO	ZPCBM	19.21% Experimental
Kari and Saghafi [142]	$CuInSe_2$	SnO_2	20.36% Simulation
This work	Cu_2O/Si	β-Ga_2O_3	23.02%

IV.4 Comparison of Cs_2BiAgI_6 results with $CH_3NH_3PbI_3$

Table IV.10 displays a comparison between our latest research on $CH_3NH_3PbI_3$-based perovskite solar cells and Cs_2BiAgI_6-based solar cells. The Cs_2BiAgI_6-based solar cell has a higher (PCE) of 32.86% in comparison to the $CH_3NH_3PbI_3$ solar cell with a PCE of 23.02% as shown in the table. The Cs_2BiAgI_6-based solar cell exhibits greater fill factor (FF) at 76.66%

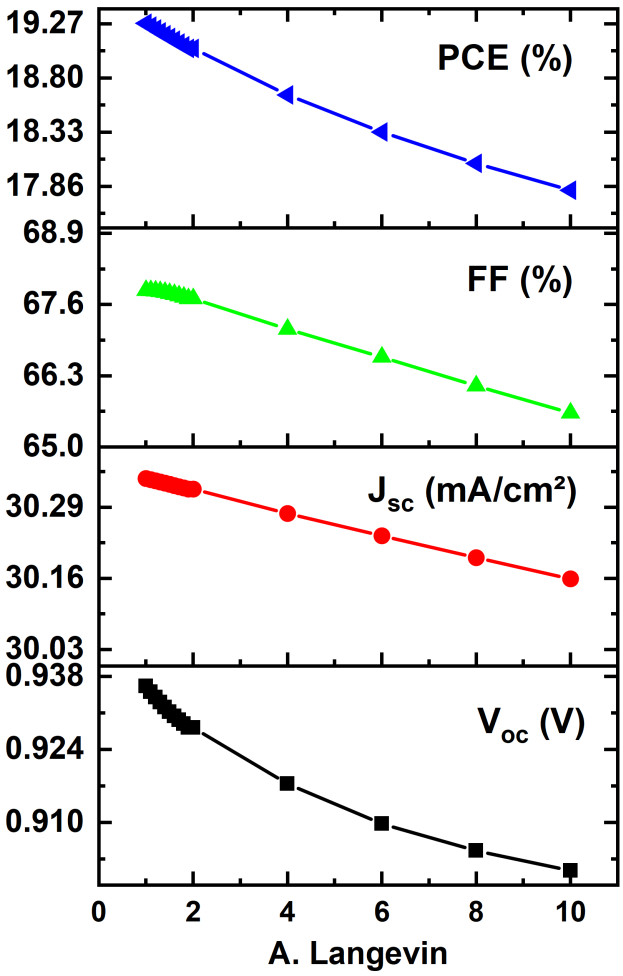

Figure IV.30: the performance parameters of the perovskite solar cell in relation to the variation of the A. Langevin parameter.

and short-circuit current density (J_{sc}) at 46.50 mA/cm^2 as compared to the $CH_3NH_3PbI_3$ solar cell with FF at 77.53%and J_{sc} at 31.12 mA/cm^2. The $CH_3NH_3PbI_3$ solar cell has a V_{oc} of $0.95V$, which is somewhat higher than the Cs_2BiAgI_6-based solar cell with a V_{oc} of $0.92V$. The Cs_2BiAgI_6-based solar cell has improved performance based on the PV characteristics presented in the table.

Table IV.10: The comparison of PV parameters of $CH_3NH_3PbI_3$ and Cs_2BiAgI_6-based solar cells.

Device structure	$PCE(\%)$	$FF(\%)$	$J_{sc}(mA/cm^2)$	$V_{oc}(V)$
Au/β-Ga_2O_3/$CH_3NH_3PbI_3$/Cu_2O/Si/Au	23.02	77.53	31.12	0.95
ITO/CuI/Cs_2BiAgI_6/WO_3/Ag	32.32	76.66	46.30	0.92

IV.5 Results of SILVACO-ATLAS Compared to Earlier Research

Table IV.11 contrasts The configurations of the devices' performance metrics shown with the most recent optimal configurations published. This table compares various photovoltaic cell structures, evaluating their performance metrics like Power Conversion Efficiency (PCE), Fill Factor (FF), Short-Circuit Current Density (J_{sc}), and Open-Circuit Voltage (Voc). Key observations highlight the structure SiO_2/ITO/CuI/Cs_2BiAgI_6/WO_3/Ag achieving the highest PCE of 32.86% with a J_{sc} of $46.30 mA/cm^2$ and V_{oc} of $0.92V$. Notably, most values are theoretical, with some experimental results providing real-world validations. The type of electron transport layer (ETL) significantly impacts performance, as evidenced by varied efficiencies achieved with different materials like TiO_2, SnO_2, and ZnO. This table underscores the importance of material choices and structural configurations in optimizing perovskite solar cells, pointing towards their potential for significant efficiency improvements.

Table IV.11: Comparison of PV Parameters of Cs_2BiAgI_6- and similar absorbers-based solar cells.

Device structure	$PCE(\%)$	$FF(\%)$	$J_{sc}(mA\setminus cm^2)$	$V_{oc}(V)$	Type
FTO/cTiO_2/mTiO_2/$Cs_2AgBiBr_6$/N719/SpiroOMeTAD/Ag [143]	2.84	-	5.13	1.06	E
FTO/TiO_2/$Cs_2AgBiBr_6$/Spiro−OMeTAD/Au [144]	2.43	62.40	3.96	0.98	E
FTO/SnO_2/$CS_2BiAgBr_6$/Cu_2O/Au [145]	16.63	69.84	15.76	1.511	T
FTO/TiO_2/$CS_2BiAgBr_6$/Cu_2O/Au [145]	16.85	71.1	15.71	1.508	T
FTO/ZnO/$CS_2BiAgBr_6$/Cu_2O/Au [145]	16.79	70.52	15.75	1.510	T
ITO/CdS/$Cs_2AgBiBr_6$/$CuAlO_2$/Pt [4]	7.16	88.74	4.913925	1.6425	T
FTO/PCBM/$Cs_2AgBiBr_6$/NiOx/Au [146]	21.92	77.03	11.49	2.49	T
ITO/PCBM/Cs_2BiAgI_6/CBTS/Au [80]	19.99	82.56	22.39	1.08	T
ITO/TiO_2/Cs_2BiAgI_6/CBTS/Au [80]	21.55	83.61	23.8	1.08	T
ITO/ZnO/Cs_2BiAgI_6/CBTS/Au [80]	21.59	83.78	23.76	1.08	T
TO/C_{60}/Cs_2BiAgI_6/CBTS/Au [80]	17.47	82.65	19.62	1.07	T
ITO/IGZO/Cs_2BiAgI_6/CBTS/Au [80]	20.42	79.04	23.65	1.09	T
ITO/SnO_2/Cs_2BiAgI_6/CBTS/Au [80]	21.52	83.54	23.76	1.08	T
ITO/CeO_2/Cs_2BiAgI_6/CBTS/Au [80]	14.44	66.21	23.59	0.92	T
ITO/WS_2/Cs_2BiAgI_6/CBTS/Au [80]	21.43	83.91	23.53	1.08	T
SiO_2/ITO/CuI/CS_2BiAgI_6/WO_3/Ag	32.86	76.66	46.30	0.92	*

Note: E = Experimental, T = Theoretical, *This work.

IV.6 Conclusion

To summarize, this study has showcased the modeling and optimization of perovskite solar cells using Cs_2BiAgI_6 and $CH_3NH_3PbI_3$, with the p-i-n and n-i-p structures being utilized, respectively. The first part of the chapter provides a detailed description of a quantitative analysis conducted using SILVACO-ATLAS on a perovskite solar cell based on Pb-free Cs_2AgBiI_6. The

work utilizes ZnO as the electron transport layer (ETL) and NiO as the hole transport layer (HTL). We made adjustments to several factors in order to enhance the efficiency of our solar device, which utilizes Cs_2AgBiI_6 with a fully inorganic architecture. Firstly, we examine the influence of altering the hole transport layer (HTL) on the efficiency of the double perovskite solar cell. The finding indicate that CuI exhibits the highest photovoltaic conversion efficiency (PCE)value, specifically 22.23%. After a thorough process of determining the most suitable Hole Transport Layer (HTL), we have carefully optimized its thickness. The CuI layer thickness has been precisely adjusted to a measurement of 0.06 µm.

Furthermore, we conducted a study on the impact of Cs_2BiAgI_6 thickness on various ETLs. We carefully controlled the thickness of the Cs_2AgBiI_6 absorber material to be exactly $1.2\mu m$ and determined that WO_3 is the optimal choice for the ETL layer. After meticulously choosing the most appropriate electron transport layer (ETL), we then proceeded to optimize their thicknesses. Our findings indicate that a WO_3 thickness of $0.1\mu m$ produced the most optimal outcomes. Additionally, we optimized the doping densities for the ntype $(N_D = 10^{19} cm^{-3})$ and p-type $(N_A = 10^{16} cm^{-3})$areas. Other crucial elements that were enhanced include the impact of ITO workfunction, back contact, temperature,antireflective layer,comparison between inverted and conventional structure. By executing these enhancements, we have successfully developed a solar device with a highly efficient configuration of SiO_2/ITO/CuI/Cs_2AgBiI_6/WO_3/Ag with efficiency of 32.86%.

The second section of the chapter demonstrates the successful optimization of lead halide perovskite solar cells (PSCs) using the SILVACO TCAD simulator. β-Ga_2O_3 stands out for its outstanding performance as both an electron transport and a window layer, surpassing ZnO because of its remarkable band alignment. Moreover, β-Ga_2O_3 functions as a very efficient layer for blocking ultraviolet light and preventing the flow of holes, thanks to its extremely broad energy bandgap. The solar cells have been significantly improved by implementing Cu_2O/Si as a double hole transport layer (Bi-HTL). For the best functionality and performance, it has been found that the absorber layer should be $0.35\mu m$ thick and the ETL layer should be 0.1 µm thick. In addition, we have looked at the effect of temperature and trap density on the device's accuracy. Temperature has a negative effect on PSC stability, according to the findings, and traps in the Perovskite or β-Ga_2O_3layers have adverse impacts as well. It is worth noting that traps located within the Cu_2O layer did not yield any effect. The study also shows that the solar cell's output parameters are negatively affected by increasing bimolecular recombination. At last, we can state that Cs_2AgBiI_6 perovskites have better electrical capabilities than $CH_3NH_3PbI_3$perovskites.

Conclusion

Conclusion

This thesis provides a comprehensive investigation of perovskite photovoltaics (PV) in a professional manner. Extensive research has been conducted on these principles, proving their ability to improve power conversion efficiency (PCE) greatly. The objective of this thesis was to examine two separate types of perovskite solar cells. We will compare these two types of solar cells.The first chapter offers an in-depth guide to perovskite solar cells, including a detailed overview of their historical progress in power conversion efficiency. In the subsequent sections, we presented an overview of the perovskite compound family and delved into the topic of solar cells. In the following sections, Chapter 3 provided an extensive analysis of the SILVACO-ATLAS software, which was utilised in our simulation investigation.

In Chapter 4, we investigated Cs_2BiAgI_6 and $CH_3NH_3PbI_3$ perovskite solar cells. For this reason,we have divided the last chapter into two parts. The first part focuses on studying Cs_2BiAgI_6 solar cell. The second part studies $CH_3NH_3PbI_3$ solar cell. In the first part, we focused on studying the effect of different parameters on Cs_2BiAgI_6 p-i-n solar cell which is composed of NiO as the HTL layer and ZnO as the ETL layer with ITO and Ag as front and back contact. Of the top of ITO, we have used SiO_2 as an antireflective layer. The several parameters that we examined in the initial section were as follows: Initially, we performed a thorough study to examine the influence of altering the hole transport layer (HTL) on the efficiency of the double perovskite solar cell. The results suggest that CuI exhibits the best photovoltaic conversion efficiency (PCE), with an astounding value of 22.23%. Based on these data, we conducted a thorough selection process to determine the most appropriate HTL. Afterwards, we conducted a comprehensive optimisation approach to ascertain the ideal thickness of the CuI layer, precisely fine-tuning it to a measurement of $0.06\mu m$.

Furthermore, we performed a thorough examination of the impact of Cs_2BiAgI_6 thickness on different electron transport layers (ETLs). By precisely controlling the thickness of the Cs_2AgBiI_6 absorber material at $1.2\mu m$, our analysis determined that WO_3 is the best choice for the ETL layer. In addition, we made a concerted effort to optimise the thicknesses of each component. Our thorough analysis concluded that a WO_3 thickness of $0.1\mu m$ yielded the most favourable results. Furthermore, we have fine-tuned the doping densities for the n-type $(N_D = 10^{19} cm^{-3})$ and p-type $(N_A = 10^{16} cm^{-3})$ areas. Additionally, we have made it a priority to optimise a number of crucial variables, including temperature, back contact, and the impact of the ITO work function, antireflective layer, and comparison between inverted and conventional

structures. Through the implementation of these optimisations, we have successfully created a solar device with a highly efficient arrangement of SiO_2/ITO/CuI/Cs_2AgBiI_6/WO_3/Ag, resulting in an outstanding efficiency of 32.86%.

The implementation of the SILVACO TCAD simulator to effectively increase lead halide PSCs is demonstrated in the next section of the chapter. β-Ga_2O_3 is notable for its exceptional performance as a window layer as well as an electron transport, surpassing ZnO because of its extraordinary band alignment. Furthermore,β-Ga_2O_3 serves as a highly effective barrier against ultraviolet radiation and inhibits the movement of holes due to its exceptionally wide energy bandgap. The efficiency of solar cells has been greatly enhanced through the utilisation of CuO_2/Si as a dual-hole transport layer (BiHTL). Optimal functioning and performance require the absorber layer to have a thickness of $0.35\mu m$ and the ETL layer to have a thickness of$0.1\mu m$. Additionally, we have examined the impact of temperature and trap density on the device's precision. The research findings indicate that temperature has a detrimental impact in terms of PSC resilience. Additionally, the presence of traps in the Perovskite or β-Ga_2O_3 layers also has unfavourable effects. It is important to mention that traps situated within the CuO_2 layer did not produce any impact. Moreover, the study demonstrates that the solar cell's output parameters are adversely impacted by the escalation of bimolecular recombination.

CS_2BiAgI_6 and $CH_3NH_3PbI_3$ are two types of perovskite solar cells that have been studied for their potential in solar energy conversion. CS_2BiAgI_6 is a double perovskite solar cell. Its optimized designs have been investigated using. Various charge transport layers such as are β-Ga_2O_3, WO_3, WS_2, SnO_2, TiO_2, IGZO, ZnSe, CdS and ZnS are used as Electron Transport Layer (ETL), and NiO, CuI, CuO, Cu_2O, $CuSbS_2$, $CuAlO_2$, P3HT, CuSCN, MoO_3, V_2O_5, Spiro-MeOTAD, and PEDOT:PSS are used as Hole Transport Layer (HTL). The approach might open the door to additional lead-free double perovskite solar cell design optimisation.Contrarily, $CH_3NH_3PbI_3$ is an organic-inorganic-halide molecule employed in solar cells. The device structure typically consists of layers of Au,β-Ga_2O_3, $CH_3NH_3PbI_3$, and Cu_2O/Si. The perovskite material has a bandgap energy of $1.51eV$, indicating a high potential for efficient power conversion. When evaluating materials for energy harvesting, the crucial elements to examine are the light absorption capacity and the diffusion length. The perovskite $CH_3NH_3PbI_3$ material has a direct bandgap of $1.55eV$, which improves the efficiency of solar cells in converting power. The perovskite material demonstrates a substantial absorption coefficient, as well as a notable electron mobility of $7.5cm^2V^{-1}s^{-1}$ and hole mobility ranging from 12.5 to $65cm^2V^{-1}s^{-1}$. It also possesses a long carrier diffusion length, which varies from $100nm$ to $1\mu m$, and exhibits a big grain size.

CS_2BiAgI_6 and $CH_3NH_3PbI_3$ perovskites are two different forms of perovskite materials that are commonly used in solar cell technology due to their exceptional ability to absorb light and carry charges. However, it is crucial to recognise that these materials have unique electrical characteristics that can greatly impact the overall efficiency of the solar cells in which they are employed. Finally, we may conclude that CS_2BiAgI_6 perovskites have superior electrical

properties compared to $CH_3NH_3PbI_3$ perovskites. The study shows that CS_2BiAgI_6-based perovskite solar cells can reach a remarkable power conversion efficiency (PCE) of up to 32.86%. The exceptional efficiency of the CS_2BiAgI_6 material can be ascribed to its semiconducting qualities. The findings emphasise the potential of CS_2BiAgI_6 as a highly promising material for the advancement of highperformance solar cells.

$CH_3NH_3PbI_3$ perovskites have become increasingly popular In the realm of solar cells that use perovskites due to their advantageous band gap and impressive charge transport abilities. Nevertheless, it is important to mention that as compared to CS_2BiAgI_6 perovskites, they demonstrate a relatively lower electrical conductivity. The notable disparity in electrical characteristics could potentially explain the exceptional performance exhibited by CS_2BiAgI_6 perovskites.To summaries, it can be inferred that both varieties of perovskites have their distinct advantages.CS_2BiAgI_6 perovskites exhibit exceptional electrical characteristics, which could lead to improved efficiency in solar cell usage. It is important to remember that the overall efficiency of a solar cell depends on various factors, including the cell's design and the materials used in other layers. Therefore, it is crucial to do further study and optimization to fully use the possibilities of these materials.

It is noteworthy to mention that the performance of these solar cells could differ greatly based on the particular production method and the operational environment. Our intricate numerical simulation of perovskite-based solar cells functions as a reliable guidance tool, providing predictive analytics skills that are crucial for the advancement of other solar cell-based devices known for their low toxicity and high efficiency. However, there is still a lot of room for future research efforts that might potentially improve the performance metrics of these creative energy solutions. A promising area to investigate is the theoretical and empirical analysis of innovative solar cell designs. An example of a unique strategy worth exploring is the implementation of a tandem structure, which can be accomplished by integrating all inorganic perovskite solar cell into the current cell framework. This synthetic alteration has the potential to improve operational efficiency and greatly reduce toxicity by eliminating the need for lead. In conclusion, although our numerical models offer useful insights into the potential performance of perovskite-based solar cells, it is clear that additional research is necessary to explore potential design and structural adjustments. These research efforts will undoubtedly have a major impact on improving the effectiveness, cost, and environmentally friendly characteristics of perovskite-based solar cells.

Bibliography

Bibliography

[1] S. Chu and A. Majumdar, "Opportunities and challenges for a sustainable energy future," *nature*, vol. 488, no. 7411, pp. 294–303, 2012.

[2] F. Liu, Q. Dong, M. K. Wong, A. B. Djurišić, A. Ng, Z. Ren, Q. Shen, C. Surya, W. K. Chan, J. Wang *et al.*, "Is excess PbI_2 beneficial for perovskite solar cell performance?" *Advanced Energy Materials*, vol. 6, no. 7, p. 1502206, 2016.

[3] M. Zhai, C. Chen, and M. Cheng, "Advancing lead-free $Cs_2AgBiBr_6$ perovskite solar cells: challenges and strategies," *Solar Energy*, vol. 253, pp. 563–583, 2023.

[4] I. Chabri, Y. Benhouria, A. Oubelkacem, A. Kaiba, I. Essaoudi, and A. Ainane, " $Cs_2AgBiBr_6$-based perovskite solar cell: A novel combination of ITO/CdS/$Cs_2AgBiBr_{6/}$$CuAlO_{2/}$Pt, with inorganic charge transport layers," *Optik*, vol. 274, p. 170560, 2023.

[5] J.-H. Kim, Y. R. Kim, J. Kim, C.-M. Oh, I.-W. Hwang, J. Kim, S. Zeiske, T. Ki, S. Kwon, H. Kim *et al.*, "Efficient and stable perovskite solar cells with a high open-circuit voltage over 1.2 v achieved by a dual-side passivation layer," *Advanced Materials*, vol. 34, no. 41, p. 2205268, 2022.

[6] J. Jeong, M. Kim, J. Seo, H. Lu, P. Ahlawat, A. Mishra, Y. Yang, M. A. Hope, F. T. Eickemeyer, M. Kim *et al.*, "Pseudo-halide anion engineering for α-$FAPbI_3$ perovskite solar cells," *Nature*, vol. 592, no. 7854, pp. 381–385, 2021.

[7] M. Gratzel, "The rise of highly efficient and stable perovskite solar cells," *Accounts of chemical research*, vol. 50, no. 3, pp. 487–491, 2017.

[8] R. Azmi, E. Ugur, A. Seitkhan, F. Aljamaan, A. S. Subbiah, J. Liu, G. T. Harrison, M. I. Nugraha, M. K. Eswaran, M. Babics *et al.*, "Damp heat–stable perovskite solar cells with tailored-dimensionality 2d/3d heterojunctions," *Science*, vol. 376, no. 6588, pp. 73–77, 2022.

[9] A. Kojima, K. Teshima, Y. Shirai, and T. Miyasaka, "Organometal halide perovskites as visible-light sensitizers for photovoltaic cells," *Journal of the american chemical society*, vol. 131, no. 17, pp. 6050–6051, 2009.

[10] A. Miyata, A. Mitioglu, P. Plochocka, O. Portugall, J. T.-W. Wang, S. D. Stranks, H. J. Snaith, and R. J. Nicholas, "Direct measurement of the exciton binding energy and effective masses for charge carriers in organic–inorganic tri-halide perovskites," *Nature Physics*, vol. 11, no. 7, pp. 582–587, 2015.

[11] G. Giorgi, J.-I. Fujisawa, H. Segawa, and K. Yamashita, "Small photocarrier effective masses featuring ambipolar transport in methylammonium lead iodide perovskite: a density functional analysis," *The journal of physical chemistry letters*, vol. 4, no. 24, pp. 4213–4216, 2013.

[12] A. Baumann, S. Vath, P. Rieder, M. C. Heiber, K. Tvingstedt, and V. Dyakonov, "Identification of trap states in perovskite solar cells," *The journal of physical chemistry letters*, vol. 6, no. 12, pp. 2350–2354, 2015.

[13] G. Xing, N. Mathews, S. Sun, S. S. Lim, Y. M. Lam, M. Grätzel, S. Mhaisalkar, and T. C. Sum, "Long-range balanced electron-and hole-transport lengths in organic-inorganic $CH_3NH_3PbI_3$," *Science*, vol. 342, no. 6156, pp. 344–347, 2013.

[14] C. Wehrenfennig, G. E. Eperon, M. B. Johnston, H. J. Snaith, and L. M. Herz, "High charge carrier mobilities and lifetimes in organolead trihalide perovskites," *Advanced Materials (Deerfield Beach, Fla.)*, vol. 26, no. 10, p. 1584, 2014.

[15] M. V. Kovalenko, L. Protesescu, and M. I. Bodnarchuk, "Properties and potential optoelectronic applications of lead halide perovskite nanocrystals," *Science*, vol. 358, no. 6364, pp. 745–750, 2017.

[16] E. A. Katz, "Perovskite: name puzzle and german-russian odyssey of discovery," *Helvetica Chimica Acta*, vol. 103, no. 6, p. e2000061, 2020.

[17] R. Sharma, A. Sharma, S. Agarwal, and M. Dhaka, "Stability and efficiency issues, solutions and advancements in perovskite solar cells: A review," *Solar Energy*, vol. 244, pp. 516–535, 2022.

[18] D. B. Mitzi, K. Chondroudis, and C. R. Kagan, "Organic-inorganic electronics," *IBM journal of research and development*, vol. 45, no. 1, pp. 29–45, 2001.

[19] J.-H. Im, C.-R. Lee, J.-W. Lee, S.-W. Park, and N.-G. Park, "6.5% efficient perovskite quantum-dot-sensitized solar cell," *Nanoscale*, vol. 3, no. 10, pp. 4088–4093, 2011.

[20] H.-S. Kim, C.-R. Lee, J.-H. Im, K.-B. Lee, T. Moehl, A. Marchioro, S.-J. Moon, R. Humphry-Baker, J.-H. Yum, J. E. Moser *et al.*, "Lead iodide perovskite sensitized all-solid-state submicron thin film mesoscopic solar cell with efficiency exceeding 9%," *Scientific reports*, vol. 2, no. 1, p. 591, 2012.

[21] J. Burschka, N. Pellet, S.-J. Moon, R. Humphry-Baker, P. Gao, M. K. Nazeeruddin, and M. Grätzel, "Sequential deposition as a route to high-performance perovskite-sensitized solar cells," *Nature*, vol. 499, no. 7458, pp. 316–319, 2013.

[22] J.-H. Im, I.-H. Jang, N. Pellet, M. Grätzel, and N.-G. Park, "Growth of $CH_3NH_3PbI_3$ cuboids with controlled size for high-efficiency perovskite solar cells," *Nature nanotechnology*, vol. 9, no. 11, pp. 927–932, 2014.

[23] F. Giordano, A. Abate, J. P. Correa Baena, M. Saliba, T. Matsui, S. H. Im, S. M. Zakeeruddin, M. K. Nazeeruddin, A. Hagfeldt, and M. Graetzel, "Enhanced electronic properties in mesoporous tio2 via lithium doping for high-efficiency perovskite solar cells," *Nature communications*, vol. 7, no. 1, p. 10379, 2016.

[24] W. S. Yang, J. H. Noh, N. J. Jeon, Y. C. Kim, S. Ryu, J. Seo, and S. I. Seok, "High-performance photovoltaic perovskite layers fabricated through intramolecular exchange," *Science*, vol. 348, no. 6240, pp. 1234–1237, 2015.

[25] X. Li, D. Bi, C. Yi, J.-D. Décoppet, J. Luo, S. M. Zakeeruddin, A. Hagfeldt, and M. Grätzel, "A vacuum flash–assisted solution process for high-efficiency large-area perovskite solar cells," *Science*, vol. 353, no. 6294, pp. 58–62, 2016.

[26] D. Bi, C. Yi, J. Luo, J.-D. Décoppet, F. Zhang, S. M. Zakeeruddin, X. Li, A. Hagfeldt, and M. Grätzel, "Polymer-templated nucleation and crystal growth of perovskite films for solar cells with efficiency greater than 21%," *Nature Energy*, vol. 1, no. 10, pp. 1–5, 2016.

[27] W. S. Yang, B.-W. Park, E. H. Jung, N. J. Jeon, Y. C. Kim, D. U. Lee, S. S. Shin, J. Seo, E. K. Kim, J. H. Noh *et al.*, "Iodide management in formamidinium-lead-halide–based perovskite layers for efficient solar cells," *Science*, vol. 356, no. 6345, pp. 1376–1379, 2017.

[28] Q. Jiang, Y. Zhao, X. Zhang, X. Yang, Y. Chen, Z. Chu, Q. Ye, X. Li, Z. Yin, and J. You, "Surface passivation of perovskite film for efficient solar cells," *Nature Photonics*, vol. 13, no. 7, pp. 460–466, 2019.

[29] M. Green, E. Dunlop, J. Hohl-Ebinger, M. Yoshita, N. Kopidakis, and X. Hao, "Solar cell efficiency tables (version 57)," *Progress in photovoltaics: research and applications*, vol. 29, no. 1, pp. 3–15, 2021.

[30] L. Kazmerski, D. Gwinner, and A. Hicks, "Best research cell efficiencies," *National Renewable Energy Laboratory*, vol. 2, pp. 0–0, 2010.

[31] N. NREL, "Best research-cell efficiencies," *National Renewable Energy Laboratory: Golden, Colorado*, 2019.

[32] M. Green, E. Dunlop, G. Siefer, M. Yoshita, N. Kopidakis, K. Bothe, and X. Hao, "Solar cell efficiency tables (version 61)," *Progress in Photovoltaics: Research and Applications*, vol. 31, pp. 3–16, 2023.

[33] J. Park, J. Kim, H.-S. Yun, M. J. Paik, E. Noh, H. J. Mun, M. G. Kim, T. J. Shin, and S. I. Seok, "Controlled growth of perovskite layers with volatile alkylammonium chlorides," *Nature*, vol. 616, no. 7958, pp. 724–730, 2023.

[34] W. Shen, Y. Zhao, and F. Liu, "Highlights of mainstream solar cell efficiencies in 2023," *Frontiers in Energy*, vol. 18, no. 1, pp. 8–15, 2024.

[35] M. Green, E. Dunlop, M. Yoshita, N. Kopidakis, K. Bothe, G. Siefer, and X. Hao, "Solar cell efficiency tables (version 62)," *Progress in Photovoltaics: Research and Applications*, vol. 31, pp. 651–663, 2023.

[36] Y. Zhao, F. Ma, Z. Qu, S. Yu, T. Shen, H.-X. Deng, X. Chu, X. Peng, Y. Yuan, X. Zhang *et al.*, "Inactive (pbi2) 2rbcl stabilizes perovskite films for efficient solar cells," *Science*, vol. 377, no. 6605, pp. 531–534, 2022.

[37] M. Green, E. Dunlop, M. Yoshita, N. Kopidakis, K. Bothe, G. Siefer, and X. Hao, "Solar cell efficiency tables (version 63)," *Progress in Photovoltaics: Research and Applications*, vol. 32, pp. 3–13, 2024.

[38] W. Peng, K. Mao, F. Cai, H. Meng, Z. Zhu, T. Li, S. Yuan, Z. Xu, X. Feng, J. Xu *et al.*, "Reducing nonradiative recombination in perovskite solar cells with a porous insulator contact," *Science*, vol. 379, no. 6633, pp. 683–690, 2023.

[39] C. Liu, Y. Yang, H. Chen, J. Xu, A. Liu, A. S. Bati, H. Zhu, L. Grater, S. S. Hadke, C. Huang *et al.*, "Bimolecularly passivated interface enables efficient and stable inverted perovskite solar cells," *Science*, vol. 382, no. 6672, pp. 810–815, 2023.

[40] J. Li, H. Liang, C. Xiao, X. Jia, R. Guo, J. Chen, X. Guo, R. Luo, X. Wang, M. Li *et al.*, "Enhancing the efficiency and longevity of inverted perovskite solar cells with antimony-doped tin oxides," *Nature Energy*, vol. 9, no. 3, pp. 308–315, 2024.

[41] Y. Ding, B. Ding, H. Kanda, O. J. Usiobo, T. Gallet, Z. Yang, Y. Liu, H. Huang, J. Sheng, C. Liu *et al.*, "Single-crystalline TiO_2 nanoparticles for stable and efficient perovskite modules," *Nature Nanotechnology*, vol. 17, no. 6, pp. 598–605, 2022.

[42] X. Qin, Z. Zhao, Y. Wang, J. Wu, Q. Jiang, and J. You, "Recent progress in stability of perovskite solar cells," *Journal of Semiconductors*, vol. 38, no. 1, p. 011002, 2017.

[43] C. Kuang, Z. Hu, Z. Yuan, K. Wen, J. Qing, L. Kobera, S. Abbrent, J. Brus, C. Yin, H. Wang *et al.*, "Critical role of additive-induced molecular interaction on the operational stability of perovskite light-emitting diodes," *Joule*, vol. 5, no. 3, pp. 618–630, 2021.

[44] G. Ding, Y. Zheng, X. Xiao, H. Cheng, G. Zhang, Y. Shi, and Y. Shao, "Sustainable development of perovskite solar cells: keeping a balance between toxicity and efficiency," *Journal of Materials Chemistry A*, vol. 10, no. 15, pp. 8159–8171, 2022.

[45] M. Boskabady, N. Marefati, T. Farkhondeh, F. Shakeri, A. Farshbaf, and M. H. Boskabady, "The effect of environmental lead exposure on human health and the contribution of inflammatory mechanisms, a review," *Environment international*, vol. 120, pp. 404–420, 2018.

[46] F. Elfatouaki, O. Farkad, R. Takassa, S. Hassine, O. Choukri, A. Ouahdani, E. Ibnouelghazi, D. Abouelaoualim, and A. Outzourhit, "Optoelectronic and thermoelectric properties of double halide perovskite cs2agbii6 for renewable energy devices," *Solar Energy*, vol. 260, pp. 1–10, 2023.

[47] A. H. Slavney, T. Hu, A. M. Lindenberg, and H. I. Karunadasa, "A bismuth-halide double perovskite with long carrier recombination lifetime for photovoltaic applications," *Journal of the American chemical society*, vol. 138, no. 7, pp. 2138–2141, 2016.

[48] Y. Cai, W. Xie, Y. T. Teng, P. C. Harikesh, B. Ghosh, P. Huck, K. A. Persson, N. Mathews, S. G. Mhaisalkar, M. Sherburne *et al.*, "High-throughput computational study of halide double perovskite inorganic compounds," *Chemistry of Materials*, vol. 31, no. 15, pp. 5392–5401, 2019.

[49] T. Zhang, Z. Cai, and S. Chen, "Chemical trends in the thermodynamic stability and band gaps of 980 halide double perovskites: A high-throughput first-principles study," *ACS applied materials & interfaces*, vol. 12, no. 18, pp. 20 680–20 690, 2020.

[50] X.-G. Zhao, J.-H. Yang, Y. Fu, D. Yang, Q. Xu, L. Yu, S.-H. Wei, and L. Zhang, "Design of lead-free inorganic halide perovskites for solar cells via cation-transmutation," *Journal of the American Chemical Society*, vol. 139, no. 7, pp. 2630–2638, 2017.

[51] A. U. Manual, "Device simulation software," *Silvaco Int., Santa Clara, CA*, 2004.

[52] B. Mohamed El Amine, Y. Zhou, H. Li, Q. Wang, J. Xi, and C. Zhao, "Latest updates of single-junction organic solar cells up to 20% efficiency," *Energies*, vol. 16, no. 9, p. 3895, 2023.

[53] Y. Li, W. Huang, D. Zhao, L. Wang, Z. Jiao, Q. Huang, P. Wang, M. Sun, and G. Yuan, "Recent progress in organic solar cells: a review on materials from acceptor to donor," *Molecules*, vol. 27, no. 6, p. 1800, 2022.

[54] R. Wang, M. Han, Y. Wang, J. Zhao, J. Zhang, Y. Ding, Y. Zhao, X. Zhang, and G. Hou, "Recent progress on efficient perovskite/organic tandem solar cells," *Journal of Energy Chemistry*, vol. 83, pp. 158–172, 2023.

[55] G. Li, W.-H. Chang, and Y. Yang, "Low-bandgap conjugated polymers enabling solution-processable tandem solar cells," *Nature Reviews Materials*, vol. 2, no. 8, pp. 1–13, 2017.

[56] G. Yu, J. Gao, J. Hummelen, F. Wudl, and A. Heeger, "Polymer photovoltaic cells: Enhanced efficiencies via a the device structure consisted of a metal (ca or al) contact on the surface of a blend network of internal donor-acceptor heterojunctions," *Science*, vol. 270, p. 1995, 1789.

[57] A. L. Ayzner, C. J. Tassone, S. H. Tolbert, and B. J. Schwartz, "Reappraising the need for bulk heterojunctions in polymer- fullerene photovoltaics: the role of carrier transport in all-solution-processed P_3HT/PCBM bilayer solar cells," *The Journal of Physical Chemistry C*, vol. 113, no. 46, pp. 20 050–20 060, 2009.

[58] Y. Wang, Q. Zhu, H. B. Naveed, H. Zhao, K. Zhou, and W. Ma, "Sequential blade-coated acceptor and donor enables simultaneous enhancement of efficiency, stability, and mechanical properties for organic solar cells," *Advanced Energy Materials*, vol. 10, no. 7, p. 1903609, 2020.

[59] M. Zhou, C. Liao, Y. Duan, X. Xu, L. Yu, R. Li, and Q. Peng, "19.10% efficiency and 80.5% fill factor layer-by-layer organic solar cells realized by 4-bis (2-thienyl) pyrrole-2, 5-dione based polymer additives for inducing vertical segregation morphology," *Advanced Materials*, vol. 35, no. 6, p. 2208279, 2023.

[60] L. Zhan, S. Li, X. Xia, Y. Li, X. Lu, L. Zuo, M. Shi, and H. Chen, "Layer-by-layer processed ternary organic photovoltaics with efficiency over 18%," *Advanced Materials*, vol. 33, no. 12, p. 2007231, 2021.

[61] S. Hong and J. Lee, "Recent advances and challenges toward efficient perovskite/organic integrated solar cells," *Energies*, vol. 16, no. 1, p. 266, 2022.

[62] O. Inganas, "Organic photovoltaics over three decades," *Advanced materials*, vol. 30, no. 35, p. 1800388, 2018.

[63] H. Dong, S. Pang, Y. Xu, Z. Li, Z. Zhang, W. Zhu, D. Chen, H. Xi, Z. Lin, J. Zhang *et al.*, "Ultrawide band gap oxide semiconductor-triggered performance improvement of perovskite solar cells via the novel ga2o3/sno2 composite electron-transporting bilayer," *ACS Applied Materials & Interfaces*, vol. 12, no. 49, pp. 54 703–54 710, 2020.

[64] J. Kim, J. Choi, and Y. Kang, "First-principles study of srte and bate: Promising wide-band-gap semiconductors with ambipolar doping," *Current Applied Physics*, vol. 48, pp. 90–96, 2023.

[65] D. S. Ginley and C. Bright, "Transparent conducting oxides," *MRS bulletin*, vol. 25, no. 8, pp. 15–18, 2000.

[66] Y. Kang, S. H. Jeon, Y.-W. Son, Y.-S. Lee, M. Ryu, S. Lee, and S. Han, "Microscopic origin of universal quasilinear band structures of transparent conducting oxides," *Physical Review Letters*, vol. 108, no. 19, p. 196404, 2012.

[67] K. Nomura, H. Ohta, A. Takagi, T. Kamiya, M. Hirano, and H. Hosono, "Room-temperature fabrication of transparent flexible thin-film transistors using amorphous oxide semiconductors," *nature*, vol. 432, no. 7016, pp. 488–492, 2004.

[68] K. Nomura, H. Ohta, K. Ueda, T. Kamiya, M. Hirano, and H. Hosono, "Thin-film transistor fabricated in single-crystalline transparent oxide semiconductor," *Science*, vol. 300, no. 5623, pp. 1269–1272, 2003.

[69] A. K. Chandiran, N. Tetreault, R. Humphry-Baker, F. Kessler, E. Baranoff, C. Yi, M. K. Nazeeruddin, and M. Gratzel, "Subnanometer Ga_2O_3 tunnelling layer by atomic layer deposition to achieve 1.1 V open-circuit potential in dye-sensitized solar cells," *Nano letters*, vol. 12, no. 8, pp. 3941–3947, 2012.

[70] F. Shan, G. Liu, W. Lee, G. Lee, I. Kim, and B. Shin, "Structural, electrical, and optical properties of transparent gallium oxide thin films grown by plasma-enhanced atomic layer deposition," *Journal of applied physics*, vol. 98, no. 2, 2005.

[71] S. Ohira, N. Suzuki, N. Arai, M. Tanaka, T. Sugawara, K. Nakajima, and T. Shishido, "Characterization of transparent and conducting Sn-doped β-Ga_2O_3 single crystal after annealing," *Thin solid films*, vol. 516, no. 17, pp. 5763–5767, 2008.

[72] J. Robertson, "Disorder, band offsets and dopability of transparent conducting oxides," *Thin solid films*, vol. 516, no. 7, pp. 1419–1425, 2008.

[73] T. Allen and A. Cuevas, "Electronic passivation of silicon surfaces by thin films of atomic layer deposited gallium oxide," *Applied Physics Letters*, vol. 105, no. 3, 2014.

[74] J. Ma, M. Zheng, C. Chen, Z. Zhu, X. Zheng, Z. Chen, Y. Guo, C. Liu, Y. Yan, and G. Fang, "Efficient and stable nonfullerene-graded heterojunction inverted perovskite solar cells with inorganic Ga_2O_3 tunneling protective nanolayer," *Advanced Functional Materials*, vol. 28, no. 41, p. 1804128, 2018.

[75] M. K. Shahzad, M. U. Farooq, R. A. Laghari, M. A. Khan, M. B. Tahir, W. Azeem, M. M. Ali, and V. Tirth, "Investigation of structural, electronic, mechanical, & optical characteristics of Ra based-cubic hydrides $RbRaX_3$ (X= F and cl) perovskite materials for solar cell applications: First principle study," *Heliyon*, vol. 9, no. 7, 2023.

[76] K. Saranya and B. Janarthanan, "Progress and challenges of lead free halide perovskite materials for perovskite solar cell applications," *Journal of Molecular Structure*, vol. 1287, p. 135663, 2023.

[77] L. Gao, P. Hu, and S. F. Liu, "Low-dimensional perovskite modified 3d structures for higher-performance solar cells," *Journal of Energy Chemistry*, vol. 81, pp. 389–403, 2023.

[78] A. Bojar, "Heterojunctions and silicon/perovskite tandem solar cells," Ph.D. dissertation, Université Paris-Saclay, 2021.

[79] A. HIMA, "Study and optimization of perovskite-based solar cells," Ph.D. dissertation, Echahid Hamma Lakhdar University of El-Oued, 2020.

[80] M. K. Hossain, A. Arnab, R. C. Das, K. Hossain, M. Rubel, M. F. Rahman, H. Bencherif, M. Emetere, M. K. Mohammed, and R. Pandey, "Combined DFT, SCAPS-1D, and wx-AMPS frameworks for design optimization of efficient Cs_2BiAgI_6-based perovskite solar cells with different charge transport layers," *RSC advances*, vol. 12, no. 54, pp. 35 002–35 025, 2022.

[81] B. Yang, J. Chen, S. Yang, F. Hong, L. Sun, P. Han, T. Pullerits, W. Deng, and K. Han, "Lead-free silver-bismuth halide double perovskite nanocrystals," *Angewandte Chemie*, vol. 130, no. 19, pp. 5457–5461, 2018.

[82] T. L. Amu, "Performance optimization of tin halide perovskite solar cells via numerical simulation," Ph.D. dissertation, 2014.

[83] Z. Hu, "Investigations towards more performing and more stable solution-processed hybrid perovskite solar cells," Ph.D. dissertation, Sorbonne Université, 2020.

[84] E. Raoult, "Semi-transparent perovskite solar cells for large area 4-terminal silicon-based tandem devices," Ph.D. dissertation, Université Paris-Saclay, 2022.

[85] G. Ganesh, A. Yasin, I. I. Misnon, A. Fakharuddin, L. Schmidt-Mende, M. H. Ab Rahim, S. Thomas, and R. Jose, "Augmenting stability and performance in perovskite solar cells: A critical review on perovskite-polymer synergy," *Solar Energy*, vol. 257, pp. 266–306, 2023.

[86] K. Anoop and T. Ahipa, "Recent advancements in the hole transporting layers of perovskite solar cells," *Solar Energy*, vol. 263, p. 111937, 2023.

[87] K. Sekar, "Formamidinium-Cesium (FA – Cs) based hybrid perovskite solar cells: A comprehensive simulation and experimental analysis," Ph.D. dissertation, Limoges, 2021.

[88] F. Ali, "Investigation of metal oxides thin films developed by PVD system for perovskite solar cells," Ph.D. dissertation, Queensland University of Technology, 2019.

[89] H. Zhou, Q. Chen, G. Li, S. Luo, T.-b. Song, H.-S. Duan, Z. Hong, J. You, Y. Liu, and Y. Yang, "Interface engineering of highly efficient perovskite solar cells," *Science*, vol. 345, no. 6196, pp. 542–546, 2014.

[90] A. Kumar, D. Kumar, N. Jain, M. Kumar, G. Ghodake, S. Kumar, R. K. Sharma, J. Holovsky, V. S. Saji, and S. K. Sharma, "Enhanced efficiency and stability of electron transport layer in perovskite tandem solar cells: Challenges and future perspectives," *Solar Energy*, vol. 266, p. 112185, 2023.

[91] K. Ahmad and W. Raza, *Perovskite Materials for Energy and Environmental Applications*. John Wiley & Sons, 2022.

[92] W. L. Tan, "Synchrotron x-ray-based microstructural characterisation of perovskite solar cells," Ph.D. dissertation, Monash University.

[93] J. Stenberg, "Perovskite solar cells," 2017.

[94] D. Zhou, T. Zhou, Y. Tian, X. Zhu, and Y. Tu, "Perovskite-based solar cells: materials, methods, and future perspectives," *Journal of Nanomaterials*, vol. 2018, no. 1, p. 8148072, 2018.

[95] D. Sapori, "Hybrid perovskites: Fundamental properties and solar cell thin film technology," Ph.D. dissertation, INSA de Rennes, 2018.

[96] F. Baig, "Numerical analysis for efficiency enhancement of thin film solar cells," Ph.D. dissertation, Universitat Politècnica de València, 2019.

[97] W.-J. Yin, J.-H. Yang, J. Kang, Y. Yan, and S.-H. Wei, "Halide perovskite materials for solar cells: a theoretical review," *Journal of Materials Chemistry A*, vol. 3, no. 17, pp. 8926–8942, 2015.

[98] T. Nakada, "CIGS-based thin film solar cells and modules: unique material properties," *Electronic Materials Letters*, vol. 8, pp. 179–185, 2012.

[99] J. Ramanujam, D. M. Bishop, T. K. Todorov, O. Gunawan, J. Rath, R. Nekovei, E. Artegiani, and A. Romeo, "Flexible CIGS, CdTe and a-Si: H based thin film solar cells: A review," *Progress in Materials Science*, vol. 110, p. 100619, 2020.

[100] I. Dharmadasa and A. Alam, "How to achieve efficiencies beyond 22.1% for cdte-based thin-film solar cells," *Energies*, vol. 15, no. 24, p. 9510, 2022.

[101] J. Zhang, W. Zhang, H.-M. Cheng, and S. R. P. Silva, "Critical review of recent progress of flexible perovskite solar cells," *Materials Today*, vol. 39, pp. 66–88, 2020.

[102] Z. Song, C. L. McElvany, A. B. Phillips, I. Celik, P. W. Krantz, S. C. Watthage, G. K. Liyanage, D. Apul, and M. J. Heben, "A technoeconomic analysis of perovskite solar module manufacturing with low-cost materials and techniques," *Energy & Environmental Science*, vol. 10, no. 6, pp. 1297–1305, 2017.

[103] S. N. R. Nanduri, M. K. Siddiki, G. M. Chaudhry, and Y. Z. Alharthi, "Numerical simulation and performance optimization of perovskite solar cell," in *2017 IEEE 44th Photovoltaic Specialist Conference (PVSC)*. IEEE, 2017, pp. 1018–1021.

[104] B. Diouf, A. Muley, and R. Pode, "Issues, challenges, and future perspectives of perovskites for energy conversion applications," *Energies*, vol. 16, no. 18, p. 6498, 2023.

[105] Q.-Q. Chu, Z. Sun, J. Hah, K.-s. Moon, B. Cheng, D. Wang, P. Xiao, Y. Zhou, A. Petrozza, G.-J. Yang *et al.*, "Progress, challenges, and further trends of all perovskites tandem solar cells: A comprehensive review," *Materials Today*, 2023.

[106] A. Srivastava, J. A. K. Satrughna, M. K. Tiwari, A. Kanwade, S. C. Yadav, K. Bala, and P. M. Shirage, "Lead metal halide perovskite solar cells: Fabrication, advancement strategies, alternatives, and future perspectives," *Materials Today Communications*, vol. 35, p. 105686, 2023.

[107] H. Zhang and N.-G. Park, "Progress and issues in pin type perovskite solar cells," *DeCarbon*, p. 100025, 2023.

[108] F. Wu, R. Pathak, and Q. Qiao, "Origin and alleviation of jv hysteresis in perovskite solar cells: A short review," *Catalysis Today*, vol. 374, pp. 86–101, 2021.

[109] R. Singh and M. Parashar, "Origin of hysteresis in perovskite solar cells," *Soft-matter thin film solar cells*, vol. 12, p. 30, 2020.

[110] B. Chen, M. Yang, S. Priya, and K. Zhu, "Origin of j–v hysteresis in perovskite solar cells," *The journal of physical chemistry letters*, vol. 7, no. 5, pp. 905–917, 2016.

[111] Y. H. Khattak, "Modeling of high power conversion efficiency thin film solar cells," Ph.D. dissertation, Universitat Politècnica de València, 2019.

[112] M. Okil, A. Shaker, M. M. Salah, T. M. Abdolkader, and I. S. Ahmed, "Investigation of polymer/si thin film tandem solar cell using tcad numerical simulation," *Polymers*, vol. 15, no. 9, p. 2049, 2023.

[113] A. U. Manual, "Device simulation software," *Silvaco Int., Santa Clara, CA*, 2008.

[114] T. J. Mebelson and K. Elampari, "A study of electrical and optical characteristics of cztse solar cell using silvaco atlas," *Materials Today: Proceedings*, vol. 46, pp. 2540–2543, 2021.

[115] C. K. Maiti, *Computer aided design of micro-and nanoelectronic devices*. World Scientific, 2016.

[116] S. Baruah, J. Borah, S. Bhattarai, and S. Maity, "Optimization of all inorganic perovskite solar cell with dual active layers for beyond 29% efficiency," *Solar Energy*, vol. 263, p. 111939, 2023.

[117] M. K. Hossain, A. Arnab, R. C. Das, K. Hossain, M. Rubel, M. F. Rahman, H. Bencherif, M. Emetere, M. K. Mohammed, and R. Pandey, "Combined dft, scaps-1d, and wxamps frameworks for design optimization of efficient cs 2 biagi 6-based perovskite solar cells with different charge transport layers," *RSC advances*, vol. 12, no. 54, pp. 35 002–35 025, 2022.

[118] T. Bendib, H. Bencherif, M. Abdi, F. Meddour, L. Dehimi, and M. Chahdi, "Combined optical-electrical modeling of perovskite solar cell with an optimized design," *Optical Materials*, vol. 109, p. 110259, 2020.

[119] N. Rai, S. Rai, P. K. Singh, P. Lohia, and D. Dwivedi, "Analysis of various etl materials for an efficient perovskite solar cell by numerical simulation," *Journal of Materials Science: Materials in Electronics*, vol. 31, pp. 16 269–16 280, 2020.

[120] H. Karmaker, A. Siddique, and B. K. Das, "Numerical investigation of lead free Cs_2TiBr_6 based perovskite solar cell with optimal selection of electron and hole transport layer through SCAPS-1D simulation," *Results in Optics*, vol. 13, p. 100571, 2023.

[121] N. Shahverdi, M. Yaghoubi, M. Goodarzi, and A. Soleamani, "Optimization of anti-reflection layer and back contact of perovskite solar cell," *Solar Energy*, vol. 189, pp. 111–119, 2019.

[122] A. Slonopas, B. J. Foley, J. J. Choi, and M. C. Gupta, "Charge transport in bulk]ceCH3NH3PbI3 perovskite," *Journal of Applied Physics*, vol. 119, no. 7, 2016.

[123] M. Higashiwaki, " β-Ga_2O_3 material properties, growth technologies, and devices: a review," *AAPPS Bulletin*, vol. 32, no. 1, p. 3, 2022.

[124] D. S. Murali, S. Kumar, R. Choudhary, A. D. Wadikar, M. K. Jain, and A. Subrahmanyam, "Synthesis of Cu_2O from CuO thin films: Optical and electrical properties," *AIP advances*, vol. 5, no. 4, 2015.

[125] M. Tilli and A. Haapalinna, "Properties of silicon," in *Handbook of silicon based MEMS materials and technologies*. Elsevier, 2020, pp. 3–17.

[126] S. Heo, G. Seo, Y. Lee, D. Lee, M. Seol, J. Lee, J.-B. Park, K. Kim, D.-J. Yun, Y. S. Kim *et al.*, "Deep level trapped defect analysis in $CH_3NH_3PbI_3$ perovskite solar cells by

deep level transient spectroscopy," *Energy & Environmental Science*, vol. 10, no. 5, pp. 1128–1133, 2017.

[127] M. I. Hossain, F. H. Alharbi, and N. Tabet, "Copper oxide as inorganic hole transport material for lead halide perovskite based solar cells," *Solar energy*, vol. 120, pp. 370–380, 2015.

[128] M. Labed, N. Sengouga, M. Labed, A. Meftah, S. Kyoung, H. Kim, and Y. S. Rim, "Modeling aNi/β-Ga_2O_3 Schottky barrier diode deposited by confined magnetic-field-based sputtering," *Journal of Physics D: Applied Physics*, vol. 54, no. 11, p. 115102, 2021.

[129] Z. Galazka, " β-Ga_2O_3 for wide-bandgap electronics and optoelectronics," *Semiconductor Science and Technology*, vol. 33, no. 11, p. 113001, 2018.

[130] A. Sekkat, D. Bellet, G. Chichignoud, A. Kaminski-Cachopo, D. Muñoz-Rojas, W. Favre *et al.*, "Open-air, low-temperature deposition of phase pure Cu_2O thin films as efficient hole-transporting layers for silicon heterojunction solar cells," *Journal of Materials Chemistry A*, vol. 9, no. 29, pp. 15 968–15 974, 2021.

[131] T. Lenka, A. Soibam, K. Dey, T. Maung, and F. Lin, "Numerical analysis of high-efficiency lead-free perovskite solar cell with NiO as hole transport material and PCBM as electron transport material," *CSI Transactions on ICT*, vol. 8, pp. 111–116, 2020.

[132] N. Fakhri, M. Salay Naderi, S. Gholami Farkoush, S. SaeidNahaei, S.-N. Park, and S.-B. Rhee, "Simulation of perovskite solar cells optimized by the inverse planar method in silvaco: 3d electrical and optical models," *Energies*, vol. 14, no. 18, p. 5944, 2021.

[133] F. Wang, S. Bai, W. Tress, A. Hagfeldt, and F. Gao, "Defects engineering for high-performance perovskite solar cells," *npj Flexible Electronics*, vol. 2, no. 1, p. 22, 2018.

[134] A. R. bin Mohd Yusoff, M. Vasilopoulou, D. G. Georgiadou, L. C. Palilis, A. Abate, and M. K. Nazeeruddin, "Passivation and process engineering approaches of halide perovskite films for high efficiency and stability perovskite solar cells," *Energy & Environmental Science*, vol. 14, no. 5, pp. 2906–2953, 2021.

[135] H. Liu, P. Zhang, F. Wang, C. Jia, and Y. Chen, "Binary synergetic ions reduce defect density in ambient air processed perovskite solar cells," *Solar Energy*, vol. 198, pp. 335–342, 2020.

[136] M. Pegu, A. Ghaderian, S. Ahmad, and S. Kazim, "Reducing the trap density in $MAPbI_3$ based perovskite solar cells via bromide substitution," *ChemPlusChem*, vol. 87, no. 4, p. e202200021, 2022.

[137] E. R. Schütz, A. Fakharuddin, Y. Yalcinkaya, E. Ochoa-Martinez, S. Bijani, M. Yusoff, M. Vasilopoulou, T. Seewald, U. Steiner, S. A. Weber *et al.*, "Reduced defect density in crystalline halide perovskite films via methylamine treatment for the application in photodetectors," *APL Materials*, vol. 10, no. 8, 2022.

[138] U. Mandadapu, S. V. Vedanayakam, K. Thyagarajan, M. R. Reddy, and B. Babu, "Design and simulation of high efficiency tin halide perovskite solar cell," *Int. J. Renew. Energy Res*, vol. 7, no. 4, pp. 1603–1612, 2017.

[139] A. H. Alami, B. Rajab, J. Abed, M. Faraj, A. A. Hawili, and H. Alawadhi, "Investigating various copper oxides-based counter electrodes for dye sensitized solar cell applications," *Energy*, vol. 174, pp. 526–533, 2019.

[140] W. Yang, Y. Yao, and C.-Q. Wu, "Origin of the high open circuit voltage in planar heterojunction perovskite solar cells: Role of the reduced bimolecular recombination," *Journal of Applied Physics*, vol. 117, no. 9, 2015.

[141] Y. Xie, D. Chen, T. Chen, T. Zhang, Y. Yin, and X. Qiu, "Highly air-stable and efficient $CH_3NH_3PbI_3$ solar cells enhanced by ZnO-embedded PCBM electron transport layers," *Materials Science in Semiconductor Processing*, vol. 168, p. 107853, 2023.

[142] M. Kari and K. Saghafi, "Hysteresis reduction in planar perovskite solar cell with $CH_3NH_3PbI_3$ absorber by changing the precursor ratio and electron/hole transport layers," *Optik*, vol. 287, p. 170959, 2023.

[143] X. Yang, Y. Chen, P. Liu, H. Xiang, W. Wang, R. Ran, W. Zhou, and Z. Shao, "Multifunctional Dye Interlayers: Simultaneous Power Conversion Efficiency and Stability Enhancement of $Cs_2AgBiBr_6$ Lead-Free Inorganic Perovskite Solar Cell through Adopting a Multifunctional Dye Interlayer (Adv. Funct. Mater. 23/2020)," *Advanced Functional Materials*, vol. 30, no. 23, p. 2070147, 2020.

[144] M. S. Shadabroo, H. Abdizadeh, and M. R. Golobostanfard, "Dimethyl sulfoxide vapor-assisted $Cs_2AgBiBr_6$ homogenous film deposition for solar cell application," *ACS Applied Energy Materials*, vol. 4, no. 7, pp. 6797–6805, 2021.

[145] S. C. Yadav, J. A. K. Satrughna, and P. M. Shirage, "Investigation of the potential solar cell application of $Cs_2AgBiBr_6$ lead-free double perovskite," *Journal of Physics and Chemistry of Solids*, vol. 181, p. 111515, 2023.

[146] S. Beriha, A. Dikhit, and S. K. Tripathy, "Improving the efficiency of a FTO/PCBM/$Cs_2AgBiBr_6$/NiOx/Au lead-free double perovskite solar cell using numerical simulation through optimizing the absorption layer thickness and work function of electrodes," *Results in Optics*, vol. 12, p. 100467, 2023.

Scientific Productions

Scientific Productions

Publications in journals

- S. Barkat, A. Meftah, M. Labed, W. Laiadi, M. Abdallaoui, A. Meftah, N. Sengouga, Y.S. Rim, Gallium oxide as an electron transport, a window, an UV and a hole blocking layer for high performance perovskite solar cell: a simulation study, Opt Quantum Electron 56 (2024). https://doi.org/10.1007/s11082-023-05780-y.

International communication

- 7th International Students Science Congress 12-13 May, 2023, İzmir,Turkey.
  - **title:** Computer Simulation of an inverted Perovskite Solar Cell Using TiO_2 and WO_3 as Bi-Electron transport layer.
  - **Authors:** Barkat Sarra, Meftah Afak.
- 1st International Conference on Materials Sciences and Applications (ICMSA2023) 08-09 February 2023, Khenchela, Algeria..
  - **title:** Numerical simulation of p-i-n perovskite solar cells using different HTMs and ETMs by SILVACO-ATLAS.
  - **Authors:**Barkat Sarra, Meftah Afak, Abdallaoui Maroua.
- 1st International Seminar e on chemical process and Environment (1ST ISCPE2022) 14-15 March 2022, Biskra,Algeria.
  - **title:**Device simulation of inverted perovskite solar cell with NiO as hole transport layer and SnO_2/TiO_2 as electron transport layer
  - **Authors:**Barkat Sarra, Meftah Afak.
- 3RD INTERNATIONAL BLACK SEA COASTLINE COUNTRIES SCIENTIFIC RESEARCH SYMPOSIUM - VI March 23-24, 2023 Samsun, Turkiye

  - **title:** Perovskite solar cell structure modeling using a Bi-ETL of TiO_2 and SnO_2 thin films.

  - **Authors:** Barkat Sarra, Meftah Afak.

National communication

- Le 1er Séminaire National sur les Matériaux pour l'Environnement et le Développement Durable (MEDD) 09-10 Mai, 2023, Relizane,Algérie.

  - **title:** Inverted perovskite solar cell device simulation with NiO/PEDOT:PSS as Bi-hole transport layer and TiO_2 as electron transport layer.

  - **Authors:** Sarra Barkat, Afak Meftah,and Widad Laiadi.

- The 3rd National Conference on Applied Physics & Chemistry 12-13 march ,2023 ,Laghouat, Algeria.

  - **title:** Wo_3/TiO_2 as the Bi-electron transport material in organometal halide perovskite solar cell.

  - **Authors:** Sarra Barkat, Afak Meftah.